

THE USE OF CORE AND DRILLING DATA FOR  
SELECTIVE STIMULATION SELECTION IN THE  
CANNEY SHALE

By

HADEN P. KOLMER

Bachelor of Science in Mechanical Engineering

Oklahoma State University

Stillwater, OK

2019

Submitted to the Faculty of the  
Graduate College of the  
Oklahoma State University  
in partial fulfillment of  
the requirements for  
the Degree of  
MASTER OF SCIENCE  
May, 2021

THE USE OF CORE AND DRILLING DATA FOR  
SELECTIVE STIMULATION SELECTION IN THE  
CANNEY SHALE

Thesis Approved:

Dr. Geir Hareland

---

Thesis Adviser

Dr. Prem Bikkina

---

Dr. Mohammed Al-Dushaishi

---

## ACKNOWLEDGEMENTS

I would like to start by thanking my advisor, Dr. Geir Hareland, for giving me the opportunity to work on this project and providing guidance on the thesis, it became. I would also like to thank my distinguished professors, Dr. Mohammed Al-Dushaishi and Dr. Prem Bikkina, for their unwavering support and unlimited knowledge.

Next, I would like to thank Andy Rihn from Continental Resources; as well as the geology teams from the Oklahoma Geological Survey, OSU, and the University of Pittsburg for logging data and triaxial tests.

Lastly, I would like to thank Dr. Mileva Radonjic who served as Principal Investigator for this project and am very thankful for the funding provided by the Department of Energy and Continental Resources. Without their help, I would not have been able to match the quality of work presented in this thesis.

Name: HADEN PATRICK KOLMER

Date of Degree: MAY, 2021

Title of Study: THE USE OF CORE AND DRILLING DATA FOR SELECTIVE  
STIMULATION SELECTION IN THE CANEY SHALE

Major Field: PETROLEUM ENGINEERING

Abstract: Completion of shale plays are costly and require intelligent optimization techniques for an effective cost-saving means of production. An optimization technique is presented that utilizes raw drilling data from existing wells to enhance the completion performance. The objective of this work is to integrate the core and drilling data from existing wells to create petrophysical and geomechanical correlations between unconfined rock strength (UCS), porosity, permeability, Poisson's Ratio, and Young's Modulus to model in a complete geomechanical property log. The proposed method is based on an inverted ROP and torque and drag friction models that have been field-tested and proven with other published data. Raw drilling data that consist of ROP, RPM, mud weight, etc. were collected from two existing wells in the Caney Shale drilled in 2014. The D-Series software was applied with the drag and inverted ROP models to the raw drilling data to obtain the downhole weight on bit (DWOB) and formation UCS for every foot of the well. The ROP model's output data consist of the UCS which is correlated to Young's Modulus, porosity, permeability, and Poisson's Ratio which were developed in this study. These correlations can then be implemented to new wells in the same geographic area to provide the optimal selective perforation criteria that will yield the highest rate of return and hydrocarbon production.

## TABLE OF CONTENTS

Chapter	Page
I. INTRODUCTION.....	1
1.1 Goals.....	2
II. REVIEW OF LITERATURE.....	3
2.1 UCS Correlations.....	3
2.1.1 Onyia’s Correlation.....	4
2.1.2 Horsrud’s Correlation.....	9
2.1.3 Andrews et al. Correlation.....	11
2.1.4 Olea et al. Correlation.....	13
2.2 In-Situ Stress Bounds.....	15
2.3 Brittleness.....	17
2.4 Wellbore Friction.....	19
2.5 ROP model.....	22
2.6 Downhole WOB to Estimate UCS.....	24
2.7 Temperature Profile.....	24
2.8 D-Series Software.....	25
2.8.1 Inverted ROP Model and Other Correlations.....	27
2.8.2 D-WOB and D-ROCK Inputs.....	30
2.8.3 Geomechanical Strength Log.....	31
2.8.4 Stimulation Index.....	32
III. FIELD OF STUDY.....	34
3.1 Garrett and Wynnell Data.....	35
3.1.1 Location.....	35
3.1.2 Well Path.....	36
3.1.3 Target Reservoir.....	39
3.2 Tomaney.....	39
3.3 Galloway.....	41

Chapter	Page
IV. METHODOLOGY .....	42
4.1 Corrections .....	42
4.1.1 Temperature .....	42
4.1.2 Depth .....	45
4.2 D-Series Inputs and Quality Control .....	47
4.3 Correlations .....	48
V. FINDINGS .....	53
5.1 Correlations .....	53
5.1.1 Porosity and UCS .....	54
5.1.2 Permeability and Porosity .....	55
5.1.3 Compressive Strength and Confining Pressure .....	56
5.1.4 Young's Modulus and Confining Pressure .....	57
5.1.5 Overview of Constants .....	58
5.2 Outputs .....	59
5.2.1 Wellbore Friction .....	59
5.2.2 SWOB vs DWOB .....	60
5.2.3 Geomechanical Strength Log .....	61
5.3 Comparison to Other Plays .....	66
5.4 STIX Formulations .....	67
5.5 Recommendation .....	69
VI. CONCLUSION & FUTURE WORK .....	70
6.1 Conclusion .....	70
6.2 Future Work .....	71
REFERENCES .....	72
APPENDIX A .....	74

## LIST OF TABLES

Table	Page
Table 1 – Olea et al. Correlation Constants for Sand and Shale .....	14
Table 2 – Analysis and Recommendations for Stimulation Design .....	17
Table 3 – Reservoir 3 Triaxial Properties at 90°C .....	41
Table 4 – Reservoir 3 Uniaxial Properties at Room Temperature .....	41
Table 5 – Formation Constant Comparison of the Caney to Eagle Ford Shale .....	59
Table 6 – Comparison of the Caney Shale to Other Shale Plays and Published Data .....	66

## LIST OF FIGURES

Figure	Page
Figure 1 – Rock Strength vs Resistivity .....	5
Figure 2 – Rock Strength vs Depth.....	6
Figure 3 – Rock Strength vs Sonic Travel Time.....	7
Figure 4 – Rock Strength vs Sonic Travel Time Excluding Dolomite Clusters .....	8
Figure 5 – Rock Strength vs Sonic Porosity .....	9
Figure 6 – UCS Estimated from Sonic and Laboratory Tests.....	11
Figure 7 – Comparing Onyia’s Results for UCS to the Optimizer’s ARS.....	13
Figure 8 – Mohr Failure Envelope for Various Confining Pressures .....	16
Figure 9 – Effect of Young’s Modulus and Poisson’s Ratio on Brittleness .....	18
Figure 10 – Typical Illustration for BHA-Tight Hole Effect on Friction Coefficient .....	21
Figure 11 – D-Series Outline .....	26
Figure 12 – Force Balance on Drillstring Elements.....	27
Figure 13 – Porosity and Permeability Relationships for Eagle Ford Formation .....	29
Figure 14 – Selective Stimulation Locations from the Geomechanical Property Log.....	31
Figure 15 – Using UCS and STIX for Recommended Zones.....	33
Figure 16 – Location of Garrett and Wynell with Respect to the Tomaney .....	36
Figure 17 – Wynell Well Path .....	37
Figure 18 – Garrett Well Path.....	38
Figure 19 – Target Depths for the Wynell and Garrett Compared to the Tomaney .....	39
Figure 20 – Caney Core from CHK Labs .....	40

Figure	Page
Figure 21 – Mohmadi and Wan Temperature Profile Compared to UCS.....	43
Figure 22 – UCS vs Temperature for Reservoirs 1, 2, and 3 Comparing 37% Reduction .....	44
Figure 23 – Varying UCS Correlations Compared to Triaxial Results .....	46
Figure 24 – Permeability vs UCS for the Tomaney Core and Other Shale Plays.....	50
Figure 25 – Porosity vs UCS for the Tomaney Core and Other Correlations.....	51
Figure 26 – Permeability vs Porosity for the Tomaney Core and Other Shale Plays .....	52
Figure 27 – Porosity vs UCS for Reservoir 3 .....	54
Figure 28 – Permeability vs Porosity for Reservoir 3.....	55
Figure 29 – Correlation between Strength and Confining Pressure.....	56
Figure 30 – Correlation between Young’s Modulus Over CCS vs Confining Pressure .....	57
Figure 31 – Overview of Trends Generated from D-ROCK.....	58
Figure 32 – Depth vs Friction Coefficient for the Garrett Lateral .....	60
Figure 33 – Surface WOB vs Downhole WOB for the Garrett Lateral .....	61
Figure 34 – UCS and Young’s Modulus vs Depth .....	63
Figure 35 – Permeability and Porosity vs Depth .....	64
Figure 36 – Poisson’s Ratio vs Depth.....	65
Figure 37 – STIX Using Equation 32 .....	67
Figure 38 – STIX Using Equation 42 with Maximum and Minimum Bounds.....	68
Figure 39 – STIX Using Equation 43 with Equal Weight Percent .....	68
Figure 40 – STIX Using Only BRIX .....	69

Figure	Page
Figure A1 – BRIX vs Depth for the Garrett Lateral .....	74
Figure A2 – BRIX vs Depth for the Garrett of Depth 11,500’ – 12,500’ .....	75
Figure A3 – BRIX vs Depth for the Garrett of Depth 12,500’ – 13,500’ .....	76
Figure A4 – BRIX vs Depth for the Garrett of Depth 13,500’ – 14,500’ .....	77
Figure A5 – BRIX vs Depth for the Garrett of Depth 14,500’ – 15,500’ .....	78
Figure A6 – BRIX vs Depth for the Garrett of Depth 15,500’ – 16,500’ .....	79
Figure A7 – BRIX vs Depth for the Garrett of Depth 16,500’ – 17,200’ .....	80

## NOMENCLATURE

Symbol	Description	Units
MWD	Measurement While Drilling	---
LWD	Logging While Drilling	---
$R_t$	Resistivity	$\Omega \cdot m$
GR	Gamma Ray	API
$\rho$	Bulk Density	g/cc
$\Delta t_c$	Sonic Compressional Travel Time	$\mu sec/ft$
$\Delta t_p$	P-Wave Internal Transit Time	$\mu sec/ft$
$K_1 - K_9$	Regression Constants	---
D	Depth	km
f	Compaction	---
$\emptyset_a$	Sonic Porosity	%
$\emptyset_{N-SS}$	Sandstone Porosity	%
$\emptyset_{N-Shale}$	Shale Porosity	%
$\emptyset$	Porosity	%
$\emptyset_N$	Neutron Porosity	%
$\delta_{ult}$	Ultimate Compressive Strength	psi
$\delta_{ARS}$	Apparent Rock Strength	psi
$\delta_{ARS-MAX}$	Maximum Apparent Rock Strength	psi
$\delta_{NORM}$	Normalized Apparent Rock Strength	---
UCS	Uniaxial Compressive Strength, SI	MPa
UCS	Uniaxial Compressive Strength, IMP	ksi
CCS	Confined Compressive Strength	ksi
G	Shear Modulus	GPa

## NOMENCLATURE

Symbol	Description	Units
$C_o$	Rock Strength	MPa
$E$	Young's Modulus, SI	GPa
$E$	Young's Modulus, IMP	Mpsi
$E_{min}$	Minimum Young's Modulus	Mpsi
$E_{max}$	Maximum Young's Modulus	Mpsi
$E_{Brit}$	Brittleness due to Young's Modulus	---
$\nu$	Poisson's Ratio	---
$\nu_{max}$	Maximum Poisson's Ratio	---
$\nu_{min}$	Minimum Poisson's Ratio	---
$\nu_{Brit}$	Brittleness due to Poisson's Ratio	---
BRIX	Brittleness Index	%
$\sigma$	Confined Rock Strength	psi
$\sigma_o$	Unconfined Rock Strength	psi
$P_e$	Effective Differential Pressure	psi
$\beta$	Internal Friction Angle	°
$\Delta$	Small Value of Pressure	psi
$K_o$	Coefficient of Earth at Rest	---
FF	Friction Force	kdaN
$\mu$	Friction Coefficient	---
$F_N$	Normal Force	kdaN
$F_{top}$	Tension at the Top of Each Element	kdaN
$F_{bottom}$	Tension at the Bottom of Each Element	kdaN
Static Weight	Static Weight of the Drillstring	kdaN

## NOMENCLATURE

Symbol	Description	Units
$w$	Unit Pipe Weight	kdaN
$\alpha$	Inclination Angle	°
$\alpha_{top}$	Inclination Angle at the Top of Element	°
$\alpha_{bottom}$	Inclination Angle at the Bottom of Element	°
$\Psi_{top}$	Azimuth Angle at the Top of Element	°
$\Psi_{bottom}$	Azimuth Angle at the Bottom of Element	°
$\theta$	Dogleg Angle	°
$\Delta L$	Length of Element	m
$\rho_{mud}$	Mud Density	kg/m <sup>3</sup>
$\rho_{pipe}$	Pipe Density	kg/m <sup>3</sup>
$\rho_o$	Annulus Density	kg/m <sup>3</sup>
$\rho_i$	Internal Density	kg/m <sup>3</sup>
$d_o$	Outside Diameter of Drill Pipe	m
$d_i$	Inside Diameter of Drill Pipe	m
$C_s$	Contact Surface Correction Factor	---
$\gamma_i$	Contact Surface Angle	°
$F$	Force on an Insert	N
$k, a, b, c, d, e$	Regression Constants	---
$h$	Penetration Depth	cm
$s$	Cross Sectional Area	cm <sup>2</sup>
$\Delta BG$	Bit Grade	---
$n_t$	Average Number of Inserts Contacting Rock	---

## NOMENCLATURE

Symbol	Description	Units
$a_E$	Formation Constant for Young's Modulus	---
$b_E$	Formation Constant for Young's Modulus	---
$a_s$	Formation Constant for UCS	---
$b_s$	Formation Constant for UCS	---
$P_c$	Confining Pressure	psi
$k_1 - k_4$	Porosity and Permeability Correlation Constants	---
$K$	Permeability	nD
Date	Drilling Date	---
Time	Drilling Time	sec
MD	Measured Depth	ft
Bit Depth	Depth of Bit	ft
WOB	Weight on Bit	klbf
Hook load	Hook Load on Drillstring	klbf
ROP	Rate of Penetration	ft/hr
RPM	Rotary Revolutions Per Minute of Drillstring	rpm
SPP	Standpipe Pressure	psi
GPM	Pump Flow Rate	gpm
dP	Differential Pressure	psi
PP	Pore Pressure	ppg
MW	Mud Weight	ppg
$W_{block}$	Weight of Traveling Block	klbf
#lines	Number of Lines	---

## NOMENCLATURE

Symbol	Description	Units
$\eta_{\text{sheave}}$	Sheave Efficiency	%
TVD	True Vertical Depth	ft
L	Drillstring Section Length	ft
ID	Drillstring Section Inner Diameter	in
OD	Drillstring Section Outer Diameter	in
$W_{\text{unit}}$	Drillstring Section Unit Weight	lb/ft
BHA	Bottom Hole Assembly	---
DP	Drill Pipes	---
HWDP	Heavy Weight Drill Pipe	---
DWOB	Downhole Weight on Bit	klbf
SWOB	Surface Weight on Bit	klbf
PDC	Polycrystalline Diamond Compact Drill Bit	---
$D_{\text{bit}}$	Bit Diameter	in
IADC code	Bit Classification	---
Bit Wear In	Bit Wear Going In	---
Bit Wear Out	Bit Wear Coming Out	---
$\#_{\text{nozzles}}$	Number of Nozzles	---
$D_{\text{nozzles}}$	Diameter of Nozzles	1/32 in
Mud Type	Water or Oil	---
Mud Motor	Mud Motor Constant	RPM/gal
$a_x, b_x, c_x$	Weighted Values Chosen by Operator	---
STIX	Stimulation Index	---

## NOMENCLATURE

Symbol	Description	Units
$UCS_{min}$	Minimum UCS in Lateral	ksi
$UCS_{max}$	Maximum UCS in Lateral	ksi
$UCS_{avg}$	Average UCS in Lateral	ksi
%UCS	Percentage Weight Contribution of UCS	%
Por	Porosity	%
$Por_{min}$	Minimum Porosity in Lateral	%
$Por_{max}$	Maximum Porosity in Lateral	%
$Por_{avg}$	Average Porosity in Lateral	%
%Por	Percentage Weight Contribution of Porosity	%
$K_{min}$	Minimum Permeability in Lateral	nD
$K_{max}$	Maximum Permeability in Lateral	nD
$K_{avg}$	Average Permeability in Lateral	nD
%K	Percentage Weight Contribution of Permeability	%
$BRIX_{avg}$	Average Brittleness Index in Lateral	---
%BRIX	Percentage Weight Contribution of Brittleness	%

## CHAPTER I

### INTRODUCTION

In the Oil & Gas industry today, downhole predictability is a crucial factor when discussing field optimization. For drilling, this is imperative for finding the optimal rate of penetration (ROP) for a specific section or length of wellbore to decrease the cost per foot, leading to an overall decrease in drilling cost. Likewise, for completions, predicting downhole rock strength, porosity, permeability, and brittleness can greatly improve the selective stimulation confidence level for greater returns and production. To provide this information, companies utilize measurement while drilling (MWD) or logging while drilling (LWD) tools to display downhole gamma, resistivity, density, and sonic values for the specific bit depth. Through recent years, models have been developed and software has been utilized to evolve the MWD or LWD values into reputable correlations for rock strength, porosity, permeability, and Poisson's Ratio. In addition, drilling data from nearby wells and core data from the target reservoir can provide the same reputable correlations. This will further enable drilling and completion optimization to take place, without the added cost of LWD or MWD tools.

## 1.1 Goals

This thesis aims at one key aspect: integrating the core and drilling data for completion optimization. Using drilling data for completion optimization, a wellbore friction analysis using a drill string drag model is used to determine the downhole weight on bit (DWOB). Using the DWOB and operating parameters at the drill bit (design and wear, RPM, flowrate, nozzle sizes, and mud weight), as well as a detailed drill bit description and reported bit wear in conjunction with an inverted rate of penetration (ROP) model, can determine the confined compressive strength (CCS) of the rock. The CCS is further correlated to uniaxial compressive strength (UCS), which is used to predict porosity, permeability, Poisson's Ratio, and UCS, through correlations modeled from laboratory core testing. Through the use of the aforementioned parameters, a selective stimulation guide can be introduced using a combination of these parameters into one stimulation index (STIX) where each of the geomechanical and petrophysical parameters are weighed.

Chapter 2 gives a comprehensive literature review of UCS correlation obtained from sonic logs, completion optimization techniques and modelling, and previous work developed for the Montney and Eagle Ford shale plays. Chapter 3 provides a background of the drilling data from the reference wells provided by Continental Resources. Chapter 4 will then discuss the completion optimization methodology, while Chapter 5 will present key findings for selective stimulation and a recommendation for a new well to be drilled in the Caney shale. The Garrett well with a lateral in the Caney reservoir zone 3 is presented, herein, to give a sample application to evaluate different forms of the STIX parameter. To conclude, a comparison of the proposed STIX models is presented, and a summary of current and future work is outlined.

## CHAPTER II

### REVIEW OF LITERATURE

As oilfield technology improves, data acquisition becomes significantly important, especially in the context of well optimization. However, MWD or LWD tools are expensive, contain data uncertainty, and provide consumption time which effect overall field cost. In addition, approximately 1 in 20 or 1 in 10 wells are cored and logged which can potentially create a working geomechanical and petrophysical property log (Tahmeen et al., 2017). To curtail this issue, developments have been made to calculate rock mechanical properties from sonic logs starting in 1988 with Onyia's correlation (Onyia, 1988) until today, where drilling data assisted by core data can provide a complete and thorough geomechanical property log necessary to decrease cost and improve stimulation (Tahmeen, 2020).

#### 2.1 UCS Correlations

The unconfined compressive strength (UCS) is the maximum axial compressive stress a right-cylindrical sample can withstand under unconfined conditions – the confining stress is zero. This is also known as the uniaxial compressive strength, due to the sample compressed along only one axis – the longitudinal axis. Numerically, UCS can range from 5,000 – 15,000 psia for shale, and to 35,000 psia for granite (Zhu, 2018).

Instinctively, a higher rock strength indicates a less fracable to stimulate due to low porosity and low permeability zone to stimulate, whereas a lesser rock strength can create additional permeable zones when stimulating and have less closing stress on the proppant (Atashnezhad et al, 2017). UCS can be a very important factor to calculate and model throughout the wellbore and can lead to enhanced recovery if known.

### 2.1.1 Onyia's Correlation

In 1988, Onyia developed and modeled in-situ mechanical strength along the wellbore by correlating resistivity and sonic to known strength values (Onyia, 1988). The induction log, which measures the response of formation to induced electromagnetic fields, formation conductivity including its inverse, deep resistivity ( $R_t$ ), are determined. While calculating UCS, or in this case, ultimate compressive strength ( $\delta_{ult}$ ) from resistivity, some key problems arise that will produce variable results for UCS. Problems such as decreased reliability when logging in shaley reservoirs, porosity, and the resistivity of the formation fluid can decrease the model confidence. Equation 1 represents the correlation between true resistivity and ultimate compressive strength, while Figure 1 represents the trend of the model compared to measured results of UCS. As shown, the model indicates a strong trend exists between UCS and  $R_t$ .

$$\delta_{ult} = -5.668 + 14.606 * \log R_t \quad (1)$$

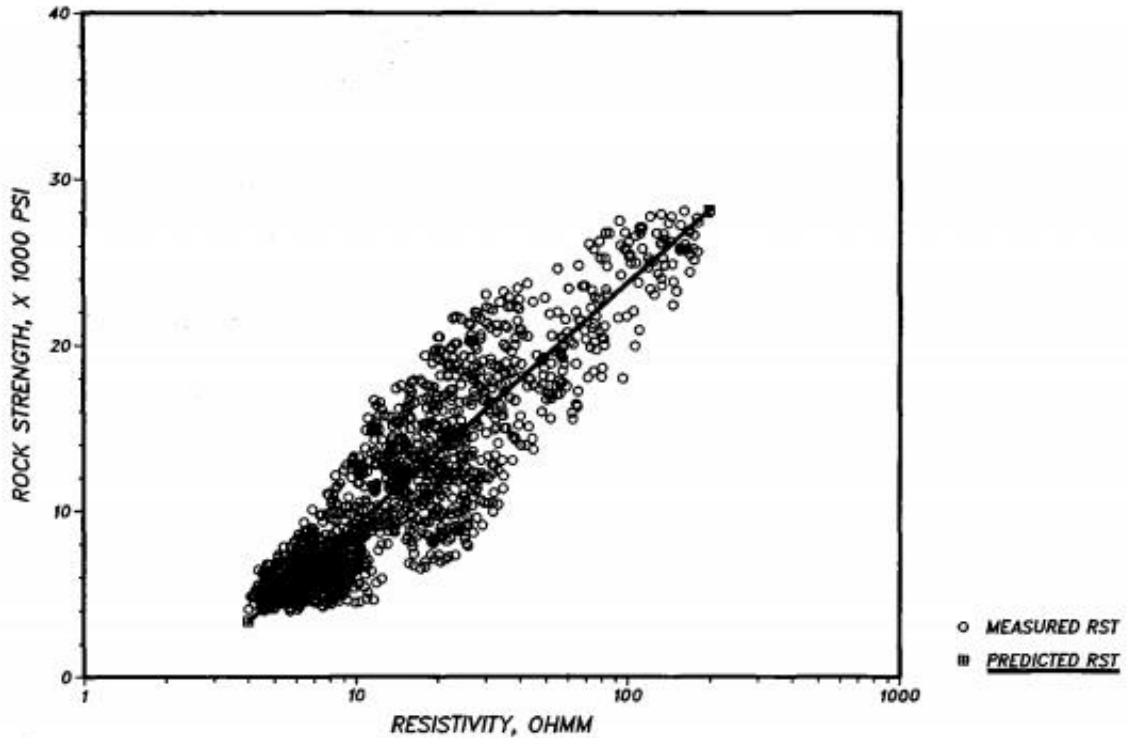


Figure 1: Rock Strength vs Resistivity (Onyia, 1988)

To avoid the issues presented in the induction log, Onyia performed a multiple linear regression analysis using a combination of resistivity, gamma ray (GR), bulk density ( $\rho$ ), and compressional travel time ( $\Delta t_c$ ) represented in Equation 2. Constants  $K_1$ ,  $K_2$ ,  $K_3$ ,  $K_4$ , and  $K_5$  represent the regression constants found which equate to 10.7616, 7.9018, -0.0187, -2.0149, and -0.0383, respectively. In addition, Figure 2 shows the multiple regression analysis compared to measured data of UCS. The fit is almost perfect for lower strength rock, approximately 200 to 1200 ft, then starts to deviate. Beyond 1200 ft, Onyia explains the difference could be due to formation fluid reducing the strength (especially in permeable and porous rock), or the relationship of rock strength to induction is not directly related due to most sedimentary rocks being nonconductive.

$$\delta_{ult} = K_1 + K_2 * \log R_t + K_3 * GR + K_4 * \rho + K_5 * \Delta t_c \quad (2)$$

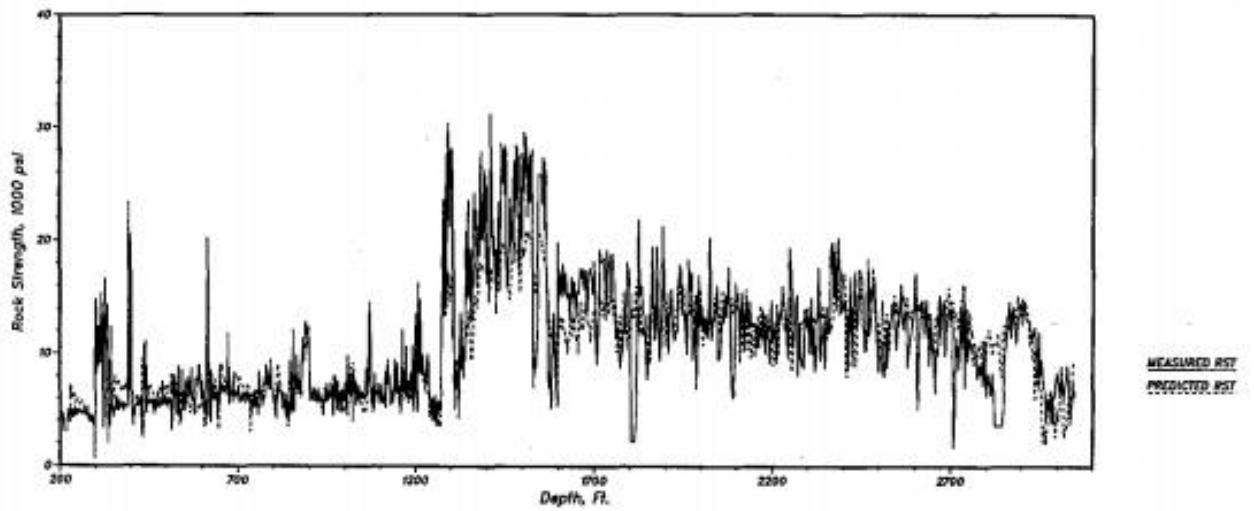


Figure 2: Rock Strength vs Depth (Onyia, 1988)

In an alternative approach, Onyia used only the sonic logs to calculate rock strength. Equation 3 utilizes regression constants  $K_6$  and  $K_7$ , equating to -3.044 and 881.1229, respectively, to create the relationship shown in Figure 3. High travel time or high porosity rocks have lower rock strength. Dolomite clusters between 50 and 60  $\mu\text{s}/\text{ft}$  on the x-axis and 2 to 25 ksi on the y-axis influence the shape of the best fit line and reduce the correlation quality.

$$\delta_{ult} = K_6 + \frac{K_7}{\Delta t_c} \quad (3)$$

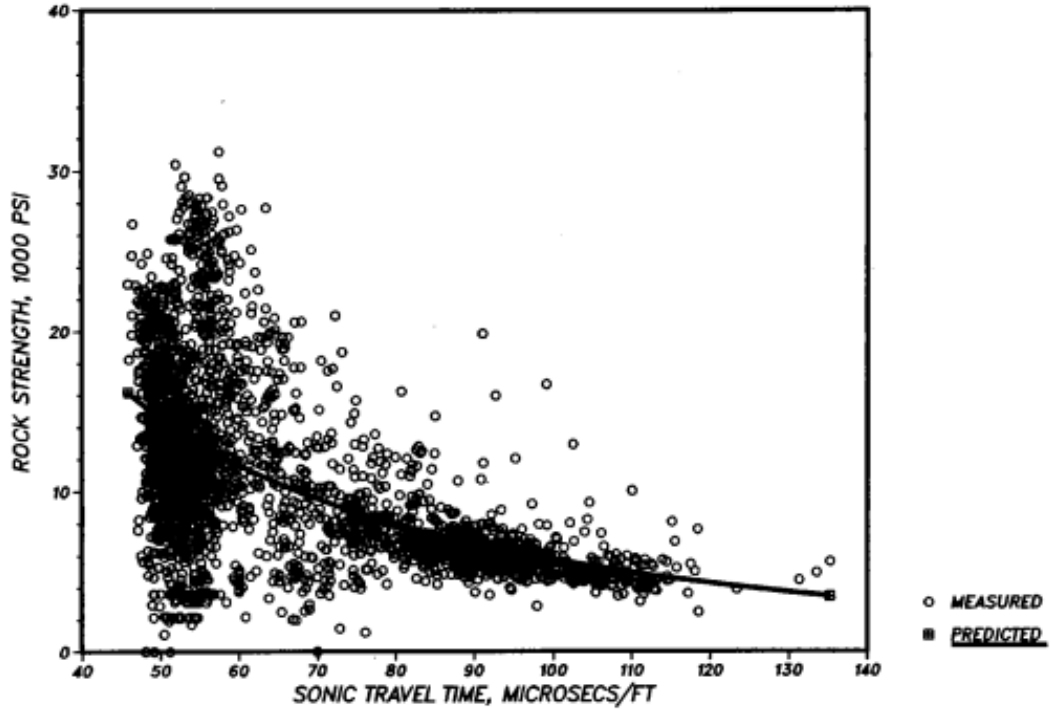


Figure 3: Rock Strength vs Sonic Travel Time (Onyia, 1988)

Extrapolating the dolomite clusters, a nonlinear regression equation was derived represented in Equation 4 where  $K_8$  is  $5.15 \times 10^{-8}$  and  $K_9$  is 23.87. While this model eliminates the dolomite cluster, data are still dispersed throughout the predicted curve depicted in Figure 4. Onyia concluded that the correlation using sonic was the best in terms of rock strength prediction and may be used in the future.

$$\delta_{ult} = \frac{1.00}{K_8(\Delta t_c - K_9)^2} + 2.0 \quad (4)$$

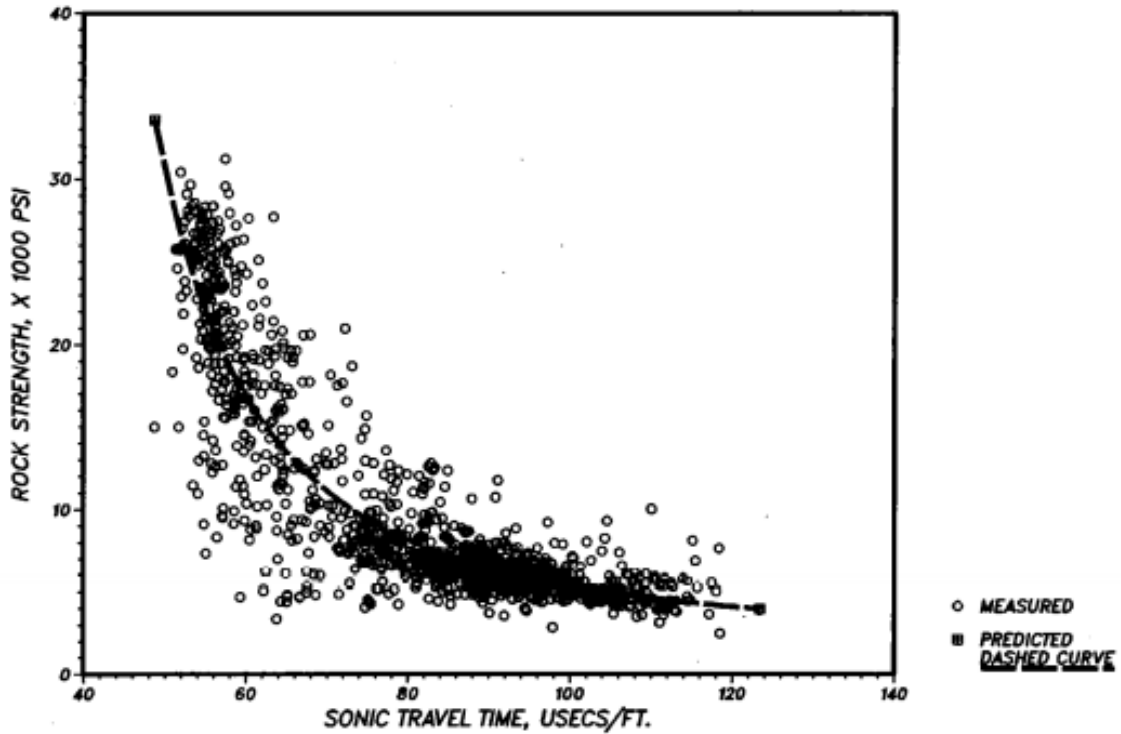


Figure 4: Rock Strength vs Sonic Travel Time Excluding Dolomite Clusters (Onyia, 1988)

To account for the reservoir water and porosity, Onyia further equated rock strength to porosity in Equation 5. While porosity can be evaluated from sonic logs, the correlation of rock strength to porosity can be modeled in a non-linear fashion, as depicted in Figure 5. As porosity increases, rock strength decreases, especially in sandstones and shales. Although porosity can be obtained from density logs, the correlation did not fit very well where sonic porosity is recommended over density porosity.

$$\delta_{ult} = 3.2205 + \frac{102.51}{\phi_a} \quad (5)$$

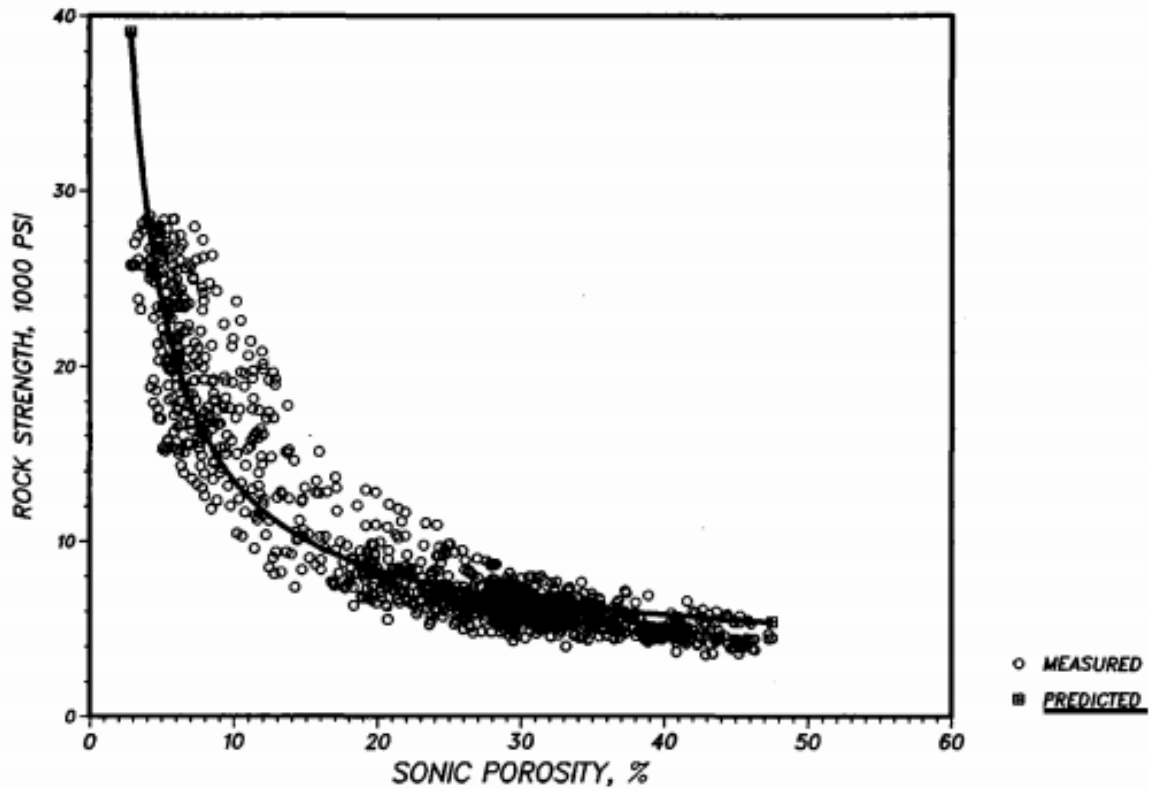


Figure 5: Rock Strength vs Sonic Porosity (Onyia, 1988)

### 2.1.2 Horsrud's Correlation

In 2001, Horsrud developed empirical correlations for rock strength, Young's Modulus, and shear modulus to predict downhole mechanical properties for borehole stability (Horsrud, 2001).

Laboratory testing of core samples obtained from the North Sea assisted in building the correlations along with sonic logs from various wells. A set of samples from one given depth were tested at different confining pressures to provide the static elastic properties and the failure properties needed for distinct modelling. For a good correlation between lab-measured P-wave velocity of shales and the mechanical properties of the shales, Horsrud uses Equations 6, 7, and 8 to determine uniaxial compressive strength ( $C_0$ ), Young's Modulus ( $E$ ), and shear modulus ( $G$ ) from P-wave velocity ( $\Delta t_p$ ). This implies that a continuous estimate of shale mechanical

properties can be obtained directly from sonic logs where  $\Delta t_p$  is the P-wave internal transit time in  $\mu\text{sec}/\text{ft}$ .

$$C_o = 0.77 * \left( \frac{304.8}{\Delta t_p} \right)^{2.93} \quad (6)$$

$$E = 0.076 * \left( \frac{304.8}{\Delta t_p} \right)^{3.23} \quad (7)$$

$$G = 0.030 * \left( \frac{304.8}{\Delta t_p} \right)^{3.30} \quad (8)$$

For confirmation, Horsrud compared the lab values of  $C_o$  at relative depths to the core interval, in meters, to three different wells drilled in different reservoirs as shown in Figure 6. The Tertiary Eocene geologic well was drilled to 1570 meters with a clay content of 82% and porosity of 41%. The Triassic geologic well was drilled to 2440 meters with a clay content of 65% and a porosity of 15%. Lastly, the Middle Jurassic well was drilled to 4870 meters with a clay content of 49% and a porosity of 3%. Between the three wells, a reasonably good estimate between lab values and correlation data were found. For the Middle Jurassic well, however, the correlation begins to deviate at greater depths, as longer travel times are seen.

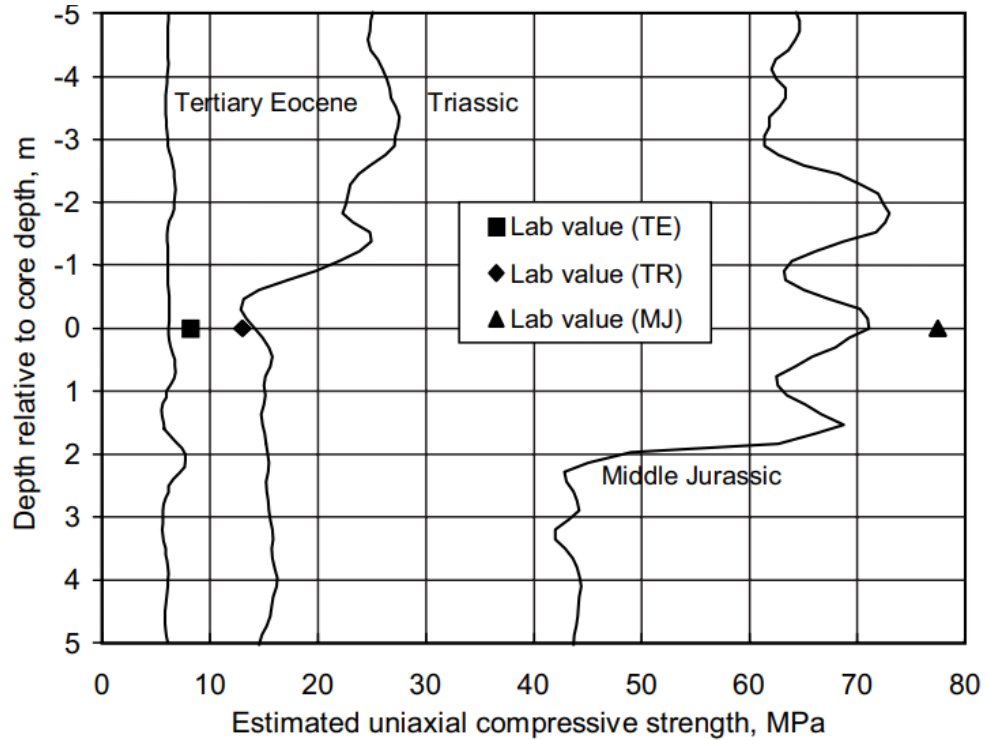


Figure 6: UCS Estimated from Sonic and Laboratory Tests (Horsrud, 2001)

### 2.1.3 Andrews et al. (2007) Correlation

In 2007, Andrews et al. developed correlations between sonic logs and formation drillability for different lithology types with data taken from 10 wells in North America (Andrews et al., 2007). The “Optimizer” (Andrews et al., 2007) is used which can estimate unconfined rock strength as apparent rock strength ( $\delta_{ARS}$ ), using a reference well that closely matches the characteristics of the planned well. The drilling inputs (WOB, RPM, flow rate, etc.) and outputs (bit wear, ROP, etc.) of the reference well are used to generate a drillability log or an apparent rock strength log (ARSL) for the planned well. The reliability of this procedure is dependent on the quality of field drilling data recorded. The ARS is a function of ROP, pore pressure, lithology, bit properties, and operational parameters. First, Andrews et al. plotted the ARSL with sonic travel time,  $\Delta t_c$ , to determine the trend of data with a boundary condition of 40  $\mu\text{sec}/\text{ft}$  to develop Equation 9. In this case,  $K_1$  and  $K_2$  are dimensionless regression constants of values 217457 and 0.52, respectively,

and the  $\delta_{ARS}$  is normalized to the maximum. The normalized apparent rock strength can then be correlated to neutron porosity,  $\phi_N$ , as an alternative correlation since Onyia concluded the poor correlation using density, in Equation 10.

$$\delta_{ARS} = \frac{K_1}{(\Delta t_c - 40)^{K_2}} \quad (9)$$

Normalize:

$$\delta_{NORM} = \frac{\delta_{ARS}}{\delta_{ARS-max}} = 1 - \phi_N^{18} \quad (10)$$

To modify the equation further, Andrews et al. (2007) accounts for rock compaction where the grain contact area and contact stress increase, which causes the bulk and shear modulus to increase. At surface levels, shale has higher porosity than sandstone. As depth increases and the rock compacts, the porosity is reduced, and the density increases due to greater overburden pressure. Since shale is normally composed of softer minerals, the compaction is greater with this lithology. To account for compaction, Equation 11 is implemented where  $f$  is the ratio of shale to sand porosity,  $\phi_{N-SS}$  is the fractional sandstone porosity,  $\phi_{N-Shale}$  is the fractional shale porosity, and  $d$  is the depth in kilometers.

$$f = \frac{1 - \phi_{N-SS}^{0.18}}{1 - \phi_{N-Shale}^{0.18}} = -0.0016 d^4 + 0.0181 d^3 - 0.0757 d^2 + 0.3121 d + 0.5 \quad (11)$$

Adding in the porosity and compaction terms to the sonic equation:

$$\delta_{ARS} = \frac{K_1(1 - \phi^{0.18})f}{(\Delta t_c - 40)^{K_2}} \quad (12)$$

Andrews et al. (2007) then conclude with a comparison in Figure 7 of the ARS in Equation 12 to Onyia's correlation for UCS to sonic in Equation 4. The data trends are similar and thus provide a good comparison of sonic to formation drillability.

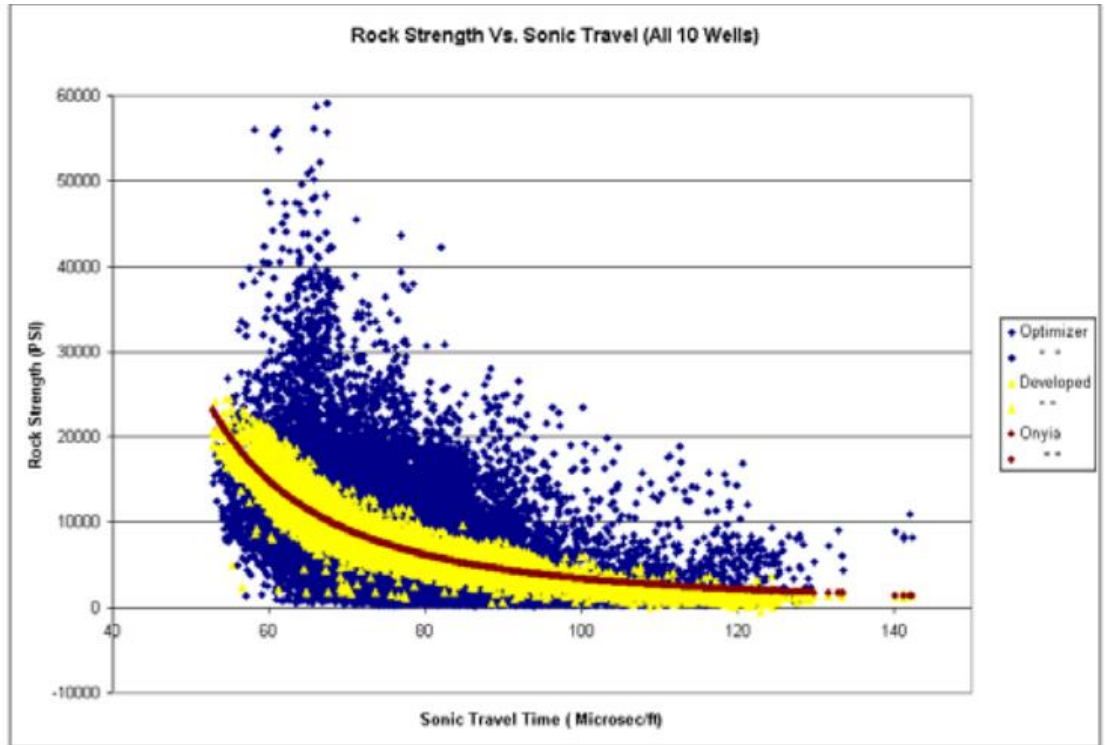


Figure 7: Comparing Onyia’s Results for UCS to the Optimizer’s ARS (Andrews et al., 2007)

#### 2.1.4 Olea et al. (2008) Correlation

In 2008, Olea et al. utilized the Andrews et al. (2007) correlation with specific salt correction factors (Olea et al., 2008). Polycrystalline salt exhibits deformation behavior that is similar to the deformation of brittle rocks and ductile metals. Salt creeps under any deviatoric stress. According to Olea et al. (2008), the deformation of salt has five typical stages: visco-elastic deformation, elastic deformation, brittle-ductile transition, final elastic deformation, and plastic behavior. First, dimensionless fitting parameters are found according to lithology to better understand the fitment and deviation of salt in the UCS computation. Table 1 represents the parameters according to lithology.

Table 1: Olea et al. (2008) Correlation Constants for Sand and Shale

	All	Shale	Sand
$K_1$	217457	754708	149595
$K_2$	0.52	0.83	0.42

To examine and account for the salt effect in determining UCS, Olea et al. (2008) implement Equations 9, 11, and 12 from Andrews et al. (2007) and Equation 4 from Onyia (1988) with changes according to fitment factors for salt. Below in Equation 13 is the adjustment to Onyia's correlation, where 10.48 and 0.5724 are the adjustable factors for salt. Furthermore, in Equations 14 and 15, the Andrews correlation is adjusted with differing  $K_1$  and  $K_2$  values that account for salt, porosity, and compaction. In Equation 14, the constants 6823.813358 for  $K_1$  and 0.2912 for  $K_2$  are used, whereas Equation 15 uses 11898 for  $K_1$ , 0.2977 for  $K_2$ , and an added adjustment exponent of 0.5724.

$$\delta_{ult} = 10.48 \left[ \frac{1.00}{5.15 \times 10^{-8} (\Delta t_c - 23.87)^2} + 2.0 \right]^{0.5724} \quad (13)$$

$$\delta_{ARS} = \frac{6823.813358}{(\Delta t_c - 40)^{0.2912}} \quad (14)$$

$$\delta_{ARS} = \frac{[11898(1 - \phi^{0.18})f]^{0.5724}}{(\Delta t_c - 40)^{0.2977}} \quad (15)$$

These equations account for lithology, salt, porosity, and rock compaction where Olea et al. (2008) compared Onyia's (1988) correlation to the corrected salt factor. Olea et al. (2008) showed the salt correction provides a smoother trend in ARS, due to the lithology correction accounting for minor salt formations. A larger salt formation appears where the salt correction is applied and, due to the thickness of the salt formation, the ARS increases and is easily noticeable, as compared to the ARS without the salt correction factors. Similarly, the bit wear tends to decrease to further

ensure the longevity of the drill bit when accounting for salt as a direct result of adjusting ROP when necessary.

## 2.2 In-Situ Stress Bounds

In 1993, Hareland and Hoberock utilized drilling parameters in prediction of bounds on minimum principal in-situ stress of rock (Hareland and Hoberock, 1993). This is important when considering the hydraulic fracturability of reservoir rock and designation for fracture programs without the need for expensive stress work. The prediction is based on knowledge of the compressive rock strength failure as a function of confining pressure that can then be used to obtain the Mohr failure envelope. This can then be used to calculate the angle of internal friction, which can further be used in calculating a “coefficient for earth at rest”. With known overburden and pore pressure, this coefficient can be used to calculate an upper bound on the minimum horizontal stress for each foot drilled. The results can be compared to 46 tests in four Gas Research Institute wells. Empirical expressions for rock strength as a function of effective differential pressure,  $P_e$ , are fit to data from previous models and represented in Equation 16, where  $\sigma$  is the confined rock strength or CCS and  $\sigma_o$  is the unconfined rock strength or UCS. Formation constants, specific to each lithology, are found by the nonlinear regression analysis. Rearranging Equation 16 and accounting for  $\sigma_o$  to change with depth due to compaction, rock hardening by cementation, grain size, and other burial factors, Hareland and Hoberock solved for  $\sigma_o$  in Equation 17.

$$\frac{\sigma}{\sigma_o} = (1 + a_s P_e^{b_s}) \quad (16)$$

$$\sigma_o = \frac{\sigma}{(1 + a_s P_e^{b_s})} \quad (17)$$

The “failure angle of friction” is defined from soil mechanic tests where the angle is the contact point between the axis of normal stress and the tangent to the Mohr failure envelope at a given

point with a certain failure stress condition. The Mohr failure envelope, shown below in Figure 8, displays various confining pressures and confined rock strengths to find the compressive stress.

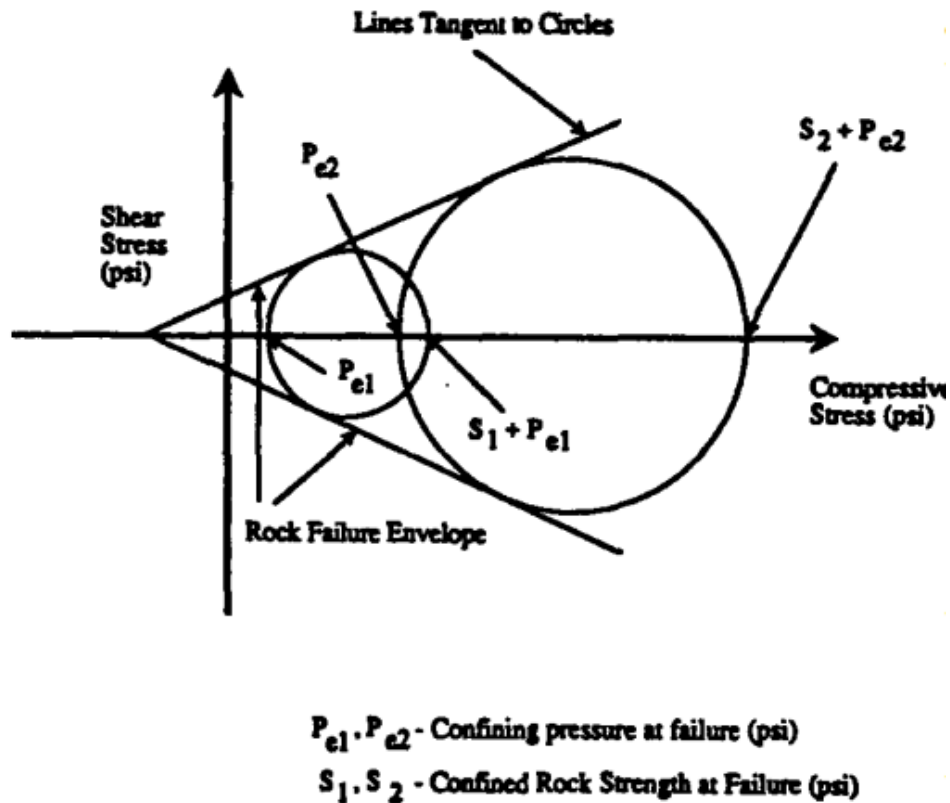


Figure 8: Mohr Failure Envelope for Various Confining Pressures (Hareland and Hoberock, 1993)

Furthermore, the “failure angle of friction” is derived in Equation 18 where  $\beta$  is the internal failure angle of friction, and  $\Delta$  is a small value of pressure, arbitrarily small – nonzero. The internal friction angle is the primary mechanism to relate rock strength to in-situ stress. A “coefficient of earth at rest”,  $K_o$ , was then used to relate overburden stress to in-situ horizontal stress. A relationship for  $K_o$ , represented in Equation 19, was obtained experimentally, while Equation 20 relates the dimensionless Poisson’s Ratio to the failure angle of friction.

$$\beta = \sin^{-1} \left[ 1 / \left( 1 + \left\{ \frac{4\Delta}{UCS * a_S * [P_{e1}^{bs} - P_{e2}^{bs}]} \right\} \right) \right] \quad (18)$$

$$K_0 = 1 - \sin(\beta) \quad (19)$$

$$v = \frac{K_0}{1 + K_0} \quad (20)$$

### 2.3 Brittleness

In 2008, Rickman et al. introduced rock brittleness derived from combining both the Poisson's Ratio and Young's Modulus (Rickman et al., 2008). These two components, as stated by Rickman et al., are combined to reflect the rock ability to fail under stress (Poisson's Ratio) and maintain a fracture (Young's Modulus) once the rock fractures. Table 2 represents various zones of the Barnett Shale that were quantified in terms of brittleness (%), thickness (ft), closure stress (psi), whether the zone was a frac barrier, frac width at 100 bbl/min (in), and finally a recommendation on the fluid type, proppant size, proppant type, and whether to frac the zone. As detailed, the higher brittleness zones reduce the closure stress and enable the zone to be fractured, while zones with lower brittleness create a frac barrier.

Table 2: Analysis and Recommendations for Stimulation Design (Rickman et al., 2008)

Zone	Brittleness, %	Thickness, ft	Closure Stress, psi	Frac Barrier, Y/N	Frac Width at 100 bbl/min, in.	Recommendations			
						Fluid Type	Proppant Size	Proppant Type	Frac ?
<b>A</b>	15.3	400	6,134	Y	0	—	—	—	N
<b>B</b>	56	82	4,650	N	0.038	Slick Water	30/50	Sand	Y
<b>C</b>	18	103	6,261	Y	0	—	—	—	N
<b>D</b>	59	91	5,150	N	0.038	Slick Water	30/50	Sand	Y
<b>E</b>	18	85	6,350	Y	0	—	—	—	N
<b>F</b>	22	40	6,040	Y	0	—	—	—	N
<b>G</b>	45	350	5,600	N	0.038	Slick Water	30/50	Sand	Y

Brittleness increases with lower values of Poisson's Ratio and higher values of Young's Modulus. With the units differing in Poisson's Ratio and Young's Modulus, Rickman et al. unitized each component then averaged to yield the brittleness coefficient as a percentage. Figure 9 displays a cross plot of the effect of Poisson's Ratio and Young's Modulus on brittleness. As previously mentioned, an increase in brittleness relates to an increase in Young's Modulus and a decrease in Poisson's Ratio.

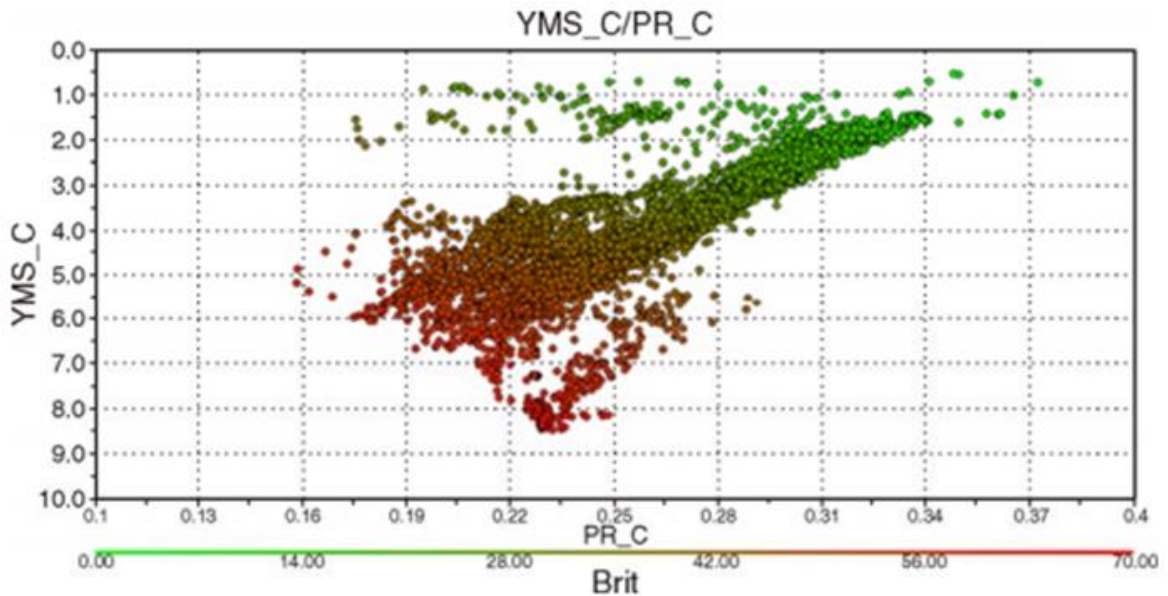


Figure 9: Effect of Young's Modulus and Poisson's Ratio on Brittleness (Rickman et al., 2008)

To calculate the brittleness index (BRIX) from Poisson's Ratio and Young's Modulus, Equations 21, 22, and 23 were used where the maximum and minimum values of each parameter are unitized for the maximum and minimum, then averaged for the brittleness index. This is important when modelling the wellbore using drilling data to create a brittleness profile to help determine optimal zones of stimulation.

$$E_{Brit} = \frac{E - E_{min}}{E_{max} - E_{min}} \quad (21)$$

$$v_{Brit} = \frac{v - v_{max}}{v_{min} - v_{max}} \quad (22)$$

$$BRIX = \frac{E_{Brit} + v_{Brit}}{2} \quad (23)$$

## 2.4 Wellbore Friction

In 2011, Fazaelizadeh et al. modeled wellbore friction and the effect of buoyancy on drillstring weight (Fazaelizadeh et al., 2011). When considering a drillstring in the wellbore filled with drilling fluid, the forces acting on the pipe are buoyed weight, axial tension, friction force (FF), and normal force ( $F_N$ ) perpendicular to the contact surface of the wellbore. Equation 24 equates this consideration:

$$FF = \mu * F_N \quad (24)$$

This is true for the straight inclined and horizontal sections where the normal force is equal to the normal weight of the element and there is no other contribution. However, Fazaelizadeh et al. considers the curved section, with such factors as build-up, drop-off, side bends and/or a combination of them, when deriving Equation 25, where the normal force mostly depends on the tension at the bottom end of the pipe element, and less on the weight of the element. The tension at the top of each element ( $F_{top}$ ) in relation to the bottom ( $F_{bottom}$ ), static weight, and coefficient of friction ( $\mu$ ) is:

$$F_{top} = F_{bottom} + \text{Static Weight} \pm \mu * F_N \quad (25)$$

Where the plus or minus sign refers to pipe movement up or down. For a straight inclined element, the normal force is weight dominated and is not dependent on axial tension at the bottom of the element. The coulomb friction model is then used in Equation 26.

$$F_{top} = F_{bottom} + \beta * w * \cos\alpha \pm \mu * \beta * w * \sin\alpha \quad (26)$$

With the introduction of the dogleg angle,  $\theta$ , which considers the wellbore azimuth and inclination, Equation 27 is developed to showcase the contact of the pipe on either the high or low side of the wellbore in the dogleg plane. The dogleg is the absolute change in direction and can be determined by:

$$\cos\theta = \frac{\sin\alpha_{top}\sin\alpha_{bottom} \cos(\psi_{top} - \psi_{bottom}) + \cos\alpha_{top}\cos\alpha_{bottom}}{\cos\alpha_{top}\cos\alpha_{bottom}} \quad (27)$$

Rearranging the equation and accounting for build-up, drop-off, side bends, or a combination of these, the axial force becomes:

$$F_{top} = \beta w \Delta L \left\{ \frac{\sin\alpha_{top} - \sin\alpha_{bottom}}{\alpha_{top} - \alpha_{bottom}} \right\} + F_{bottom} * e^{\pm\mu|\theta|} \quad (28)$$

The forces are then summed starting from the bottom of the well. Figure 10 details the well path, with the start of building for the curve in comparison to the correlated friction coefficient, to give a simple representation of the relationship between the two.

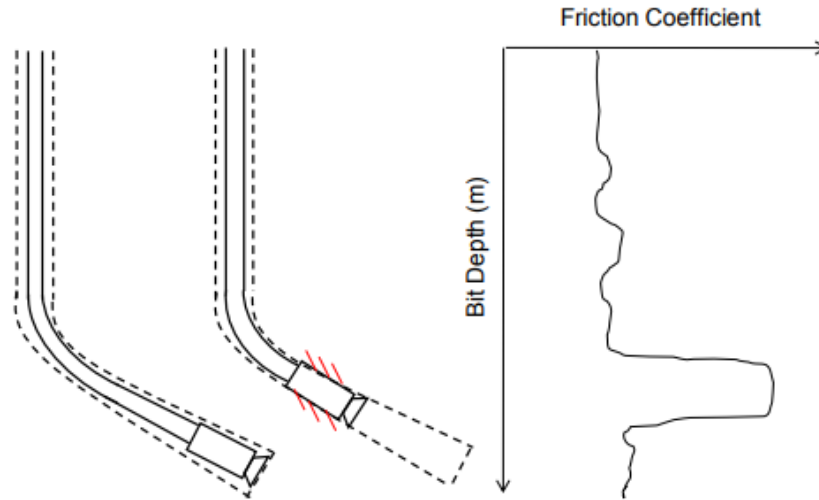


Figure 10: Typical Illustration for BHA-Tight Hole Effect on Friction Coefficient (Fazaelizadeh et al., 2011)

Fazaelizadeh et al. then used Archimedes' Principle in buoyancy calculations. The principle states that when a body is submerged into a fluid, the buoyancy force is equal to the weight of the dispersed fluid. The drillstring tension in the wellbore, when filled with drilling fluid, can be represented in Equation 29 where the buoyancy factor,  $\beta$ , is a function of the density of drilling mud,  $\rho_{mud}$ , and the density of the pipe,  $\rho_{pipe}$ . This assumes that the drilling fluid is incompressible, and the effect of temperature and cutting concentration is ignored.

$$\beta = 1 - \frac{\rho_{mud}}{\rho_{pipe}} \quad (29)$$

If there is a density difference between the inside of the string and the annulus, such as cementing or tripping in, Equation 30 accounts for the difference where subscripts "o" and "i" refer to the inside and outside of the drillstring.

$$\beta = 1 - \frac{\rho_o d_o^2 - \rho_i d_i^2}{\rho_{pipe}(d_o^2 - d_i^2)} \quad (30)$$

The correction factor,  $C_s$ , represents the effect of the contact surface area on the pipe and wellbore. Including the correction factor, the friction force becomes:

$$FF = C_s * \mu * F_N \quad (31)$$

Where the correction factor depends on the contact surface angle,  $\gamma$ , which varies between  $0^\circ$  and  $90^\circ$ , hence, the correction factor,  $C_s$ , can vary between 1 and  $\frac{4}{\pi}$ . The correction factor can be shown below in Equation 32.

$$C_s = \frac{2}{\pi} \gamma_i \left( \frac{4}{\pi} - 1 \right) + 1 \quad (32)$$

## 2.5 ROP Model

In 2011, Hareland et al. developed an ROP model for optimal drilling where WOB, RPM, rock type, bit structure, hydraulics, bit wear, and other parameters were included in the formulation (Hareland et al., 2011). For roller cone bits, Hareland et al. assumed the bit inserts are in the shape of a wedge or chisel, and there is a relationship between the force (F) and the penetration depth (h), as shown in Equation 33. Where k, a, and b are coefficients found during regression analysis to be 0.001943, 0.5407, and 0.9248, respectively, s is the cross-sectional area, and the CCS is the confined compressive strength.

$$F = k * h^a * s * CCS^b \quad (33)$$

For the cross-sectional area of an insert, the following relation is used in Equation 34 where c, d, and e are curve fitting coefficients outlined in the paper and  $\Delta BG$  is the insert wear or bit grade.

$$s = c * (h + \Delta BG)^d + e \quad (34)$$

Hareland et al. then applied the force equilibrium principle, where the applied WOB is a sum of the reaction forces in contact with the bit inserts at bottomhole. Equation 35 represents this principle where  $n_t$  is the average number of inserts in contact with the rock, and k, a, and b are data fit coefficients for various insert types outlined in the paper.

$$WOB = n_t * F = n_t * k * h^a * s * CCS^b \quad (35)$$

By the combining Equations 34 and 35, the CCS can be obtained as follows in Equation 36:

$$CCS = \left\{ \frac{WOB}{n_t * k * h^a * [c * (h + \Delta BG)^d + e]} \right\}^{\frac{1}{b}} \quad (36)$$

This correlation is important due to the relation between  $\Delta BG$ , WOB, and CCS for drilling and, in this case, completion optimization where CCS plays a vital role in correlating to UCS.

## 2.6 Downhole WOB (DWOB) to Estimate UCS

In 2014, Kerkar et al. reported a method for estimating mechanical rock properties and in-situ rock mechanical profiles in every well in a field development, based on calibration from initial rock core analyses plus drilling data that are routinely acquired (Kerkar et al., 2014). The wellbore friction analysis was combined with the torque and drag model to estimate in-situ UCS and Young's Modulus profiles. Kerkar et al. then described the process steps and compared the results to field data from the Montney Shale in Alberta, Canada. Core samples were analyzed, and using regression analysis, Equations 37 and 38 derive the correlations for Young's Modulus and UCS compared to CCS and confining pressure.

$$UCS = \frac{CCS}{1 + a_s P_c^{b_s}} \quad (37)$$

$$E = CCS * a_E * (1 + P_c) b_E \quad (38)$$

Constants  $a_E$ ,  $b_E$ ,  $a_s$ , and  $b_s$  are formation regression constants found during correlating CCS and UCS to confining pressure, and Young's Modulus and CCS to confining pressure. These constants were derived from reservoir core samples and triaxial tests.

## 2.7 Temperature Profile

In 2016, Mohamadi and Wan presented the thermo-mechanical strength characterization of the Colorado shale in Alberta, Canada (Mohamadi and Wan, 2016). Samples were tested at high

temperature and pressure along triaxial compression stress paths to indicate a simple thermo-mechanical failure criterion in core samples with a temperature differential between ambient and downhole conditions. This is important to recall when core samples are tested and UCS results are adjusted for the temperature differential.

## 2.8 D-Series Software

In 2017, Tahmeen et al. (2017) utilized drilling data to calculate petrophysical properties such as porosity and permeability, and geomechanical properties such as Young's Modulus, Poisson's Ratio, CCS, and UCS for a complete geomechanical property log along the wellbore. A wellbore friction model is used to estimate the coefficient of friction and effective downhole weight on bit (DWOB) from the routinely collected drilling data. The inverted ROP models are used to estimate the DWOB and formation lithology constants needed to calculate the geomechanical properties throughout the horizontal reservoir formations. The model was then compared to core tests for a comprehensive review. An outline of the two applications, D-WOB and D-ROCK, are presented in Figure 11. The routinely collected time and depth-based files are compounded along with the survey and drill string file for inputs into D-WOB where, using the torque and drag and sliding models, one can find the downhole WOB and friction coefficient. From this and other data such as mud information, drill bit parameters, and triaxial data, the D-ROCK software is implemented for modelling the rock mechanical and petrophysical properties.

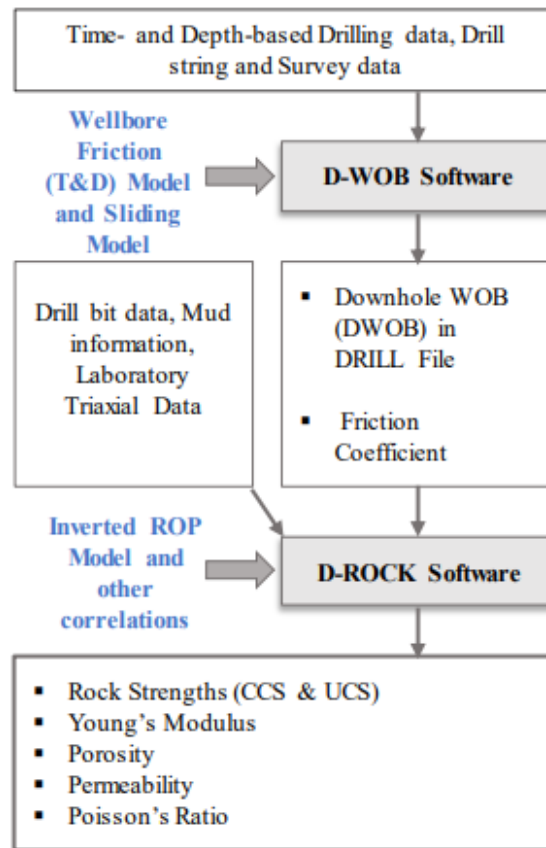


Figure 11: D-Series Outline (Tahmeen et al., 2017)

The torque and drag friction model, as previously mentioned, helps determine the friction coefficient along the wellbore (Fazalizadeh, 2011). Using the force balance for straight and bent pipe in Figure 12, Tahmeen et al. implemented this model into the D-Series software for friction determination. The force balance model implements a combination of Equations 27 and 28 to account for the friction at a straight angle in Figure 12a, and along the bend in Figure 12b. This is imperative when determining the friction coefficient later presented in Section 5.2.1, where the initial depths in Figure 32 represent the bend, and as the drillstring travels through the bend, the friction coefficient decreases and can be represented by Figure 12a.

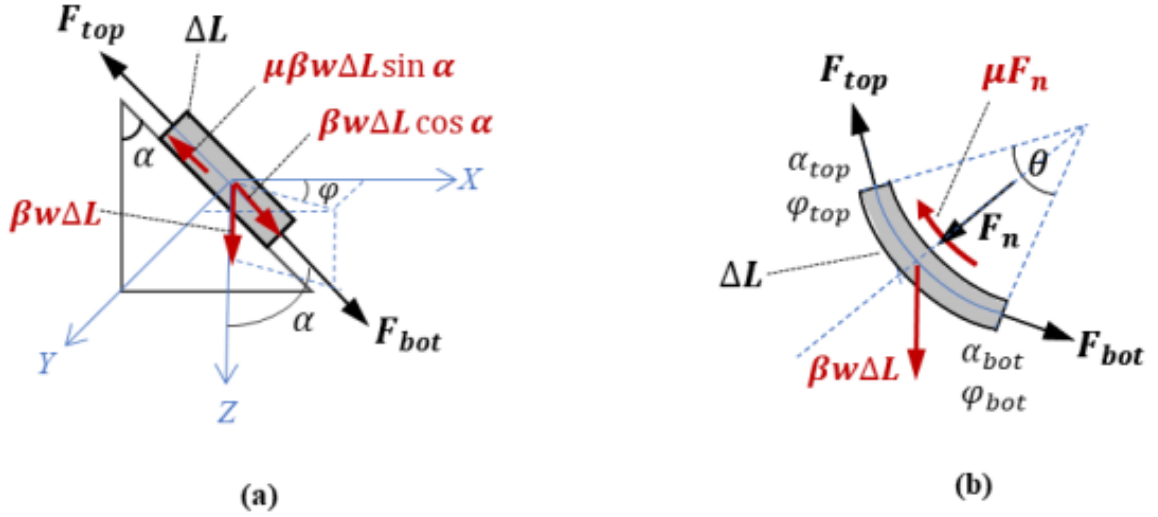


Figure 12: Force Balance on Drillstring Elements (Fazalizadeh, 2011)

### 2.8.1 Inverted ROP Model and Other Correlations

For D-ROCK, the inverted ROP model is used to quantify CCS from drilling parameters, and various correlations for porosity and permeability are used to obtain a foot-by-foot strength log for the horizontal. For PDC and rollercone drill bits, the ROP model considers ROP, DWOB, RPM, bit wear ( $W_f$ ), hydraulics ( $h_x$ ), and bit parameters ( $B_x$ ) such as nozzle size, back rake angle, side rake angle, total flow area, number of blades, size of bit, etc. (Hareland and Nygaard, 2007) (Rashidi et al., 2015) (Kerkar et al., 2014) as shown in Equation 39. Constants  $k$ ,  $a_1$ ,  $b_1$ , and  $c_1$  are regression constants found during previous modelling to be 2.5, 0.92, 1.1, and -1.5, respectively, for PDC bits. For tricone, the constants deviate depending on IADC code but stay within 10% of the PDC values.

$$CCS = \left[ \frac{ROP}{k \times DWOB^{b_1} \times RPM^{c_1} \times h_x \times W_f \times B_x} \right]^{\frac{1}{a_1}} \quad (39)$$

The porosity and UCS correlation for shale was obtained from various shale cores and cuttings analysis (Cedola et al., 2017a) as:

$$\phi = k_1 * UCS^{-k_2} \quad (40)$$

The permeability and porosity correlation for the lower Eagle Ford shale formation was obtained from trendline analysis, as given below, and represented in Figure 13:

$$K_p = k_3 * \phi^{k_4} \quad (41)$$

Where  $k_1$ ,  $k_2$ ,  $k_3$ , and  $k_4$  are regression constants found when plotting porosity vs UCS and permeability vs porosity for any given depth.

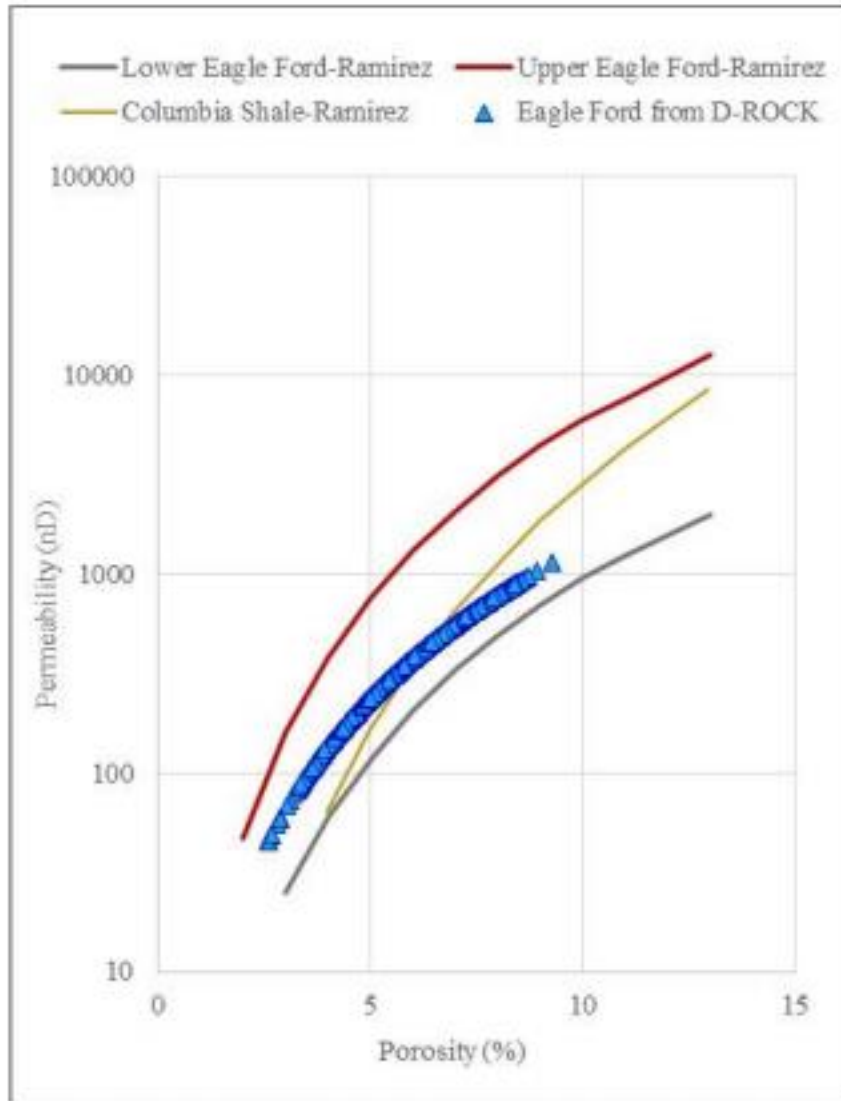


Figure 13: Porosity and Permeability Relationships for Eagle Ford Formation (Cedola et al., 2017)

The values of  $k_1$ ,  $k_2$ ,  $k_3$ , and  $k_4$  calculated for the lower Eagle Ford formation are 92.529, 0.63, 4.0302 and 2.5313, respectively. From Kerkar et al. in Equation 37 and 38, the constants  $a_E$ ,  $b_E$ ,  $a_s$ , and  $b_s$  are 0.234, -0.075, 1.323 and 0.115, respectively.

### 2.8.2 D-WOB and D-ROCK Inputs

For inputs into the software, common drilling data can be obtained, and quality controlled for accurate friction analysis, DWOB, and geomechanical and petrophysical property calculations.

For inputs required for D-WOB, the following are needed:

- Drilling data: date & time, measured/hole depth, bit depth, WOB, hook load, ROP, rotary RPM, stand-pipe pressure, flow rate, differential pressure, and pore pressure
- Survey data: measured depth, true vertical depth, inclination, and azimuth
- Drill string configuration: lengths, inner diameter, outer diameter, and unit weights of drill string sections, such as bit and bottom hole assembly (BHA) components, drill pipes (DP), and heavy weight drill pipe (HWDP)
- Additional data: weight of travelling block, number of lines, single sheave efficiency, and mud weight

For D-ROCK, the following inputs are required:

- Drill data: output file from D-WOB including measured/hole depth, TVD, downhole weight on bit, ROP, RPM, SPP, flow rate, pore pressure and mud weight
- Drill bit data: type of drill bit (PDC or Rollercone), bit diameter, IADC code, bit wear in and wear out, number and diameter of bit nozzles
- Mud and formation data: drilling mud type (water or oil), mud motor constants and type of formation
- Laboratory triaxial data: confining pressure, CCS, average UCS, Young's Modulus, and Poisson's Ratio

### 2.8.3 Geomechanical Strength Log

From the downhole weight on bit calculated from D-WOB, correlations derived from regression analysis for porosity, permeability, Poisson's Ratio, and Young's Modulus, Tahmeen et al. then presented the geomechanical strength log for the lower Eagle Ford wells. Figure 14 shows the geomechanical log plotted with depth versus UCS, porosity, permeability, and STIX which will be discussed next in Section 2.8.4. Zones of lower UCS indicate a softer formation with higher porosity and permeability. Likewise, zones with higher UCS refer to zones of harder strength with lower porosity and permeability.

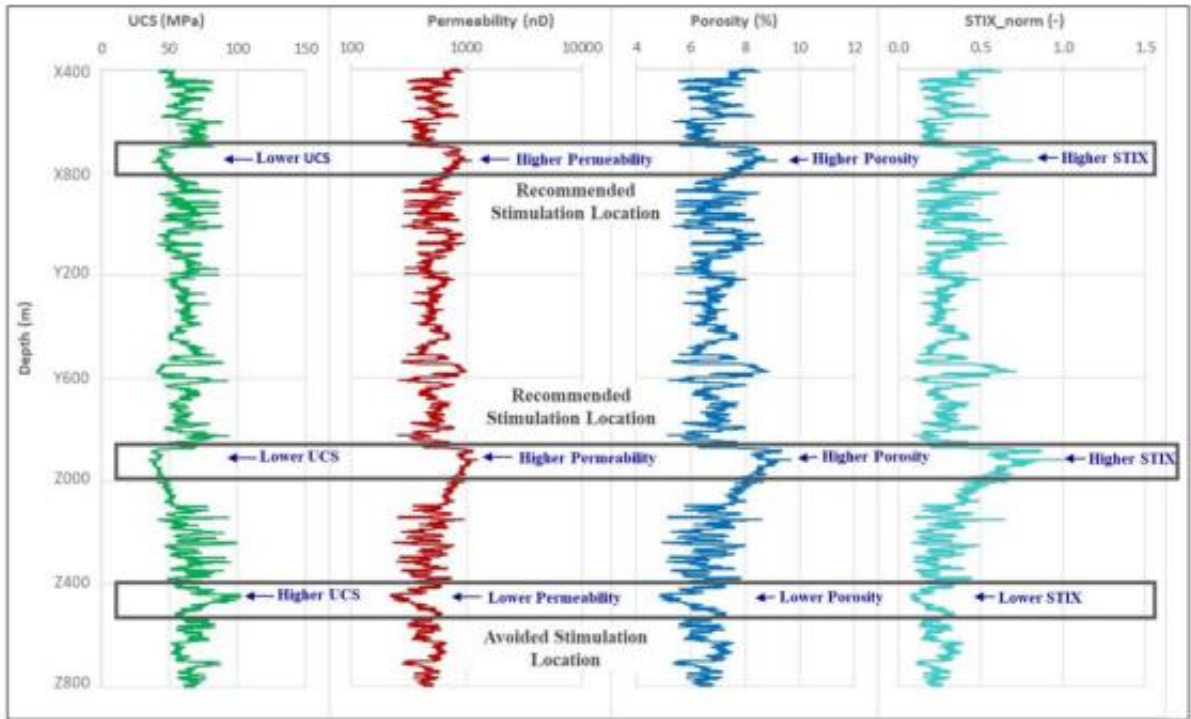


Figure 14: Selective Stimulation Locations from the Geomechanical Property Log (Tahmeen et al. 2017)

#### 2.8.4 Stimulation Index

The stimulation index or STIX is a dimensionless weighted value for quantifying a selective stimulation parameter – accounting for brittleness, UCS, porosity, and permeability. The STIX will allow companies to vary their selection criteria for perforating and will ultimately dictate the optimal zones of completion. In Equation 42, the STIX is formulated from the ratio of Young’s Modulus to Poisson’s Ratio (brittleness), UCS raised to the negative power indicating the inverse effect of UCS on stimulation, porosity raised to the positive power indicating the positive correlation to STIX, and likewise for permeability. The exponents  $a_x$ ,  $b_x$ , and  $c_x$  are weighted values that correlate to the impact of each parameter. An operator can choose which parameter affects stimulation the most. For example, Tahmeen at al. used values of 1.5, 1.0, and 1.0 for  $a_x$ ,  $b_x$ , and  $c_x$ , respectively, showing that UCS is more impactful, and porosity and permeability are equally impactful. As discussed previously in Figure 14, the STIX is plotted with corresponding values of UCS, porosity, and permeability. In this case, the STIX is normalized over the maximum to give a value between 0 and 1, where zero indicates a lower ability to create fractures or stimulate, and a STIX value of one indicates high brittleness, porosity, and permeability, with low UCS and therefore, a higher fracturability.

$$STIX = \frac{E}{\nu} * UCS^{-a_x} * \phi^{b_x} * K_p^{c_x} \quad (42)$$

Furthermore, when plotting UCS and STIX versus depth, zones of optimal completion or “sweet spots” can be located. Figure 15 displays this value. As detailed, the zones with higher UCS than STIX, such as arbitrary depths XY25 and XY26, are not recommended for stimulation. These zones should be avoided as the fracture network will not expand at the same length as other zones

and may result in greater closure stress and lower fracture initiation. On the other hand, zones where the STIX is higher than UCS, such as depths XYD1 and XYF1, are recommended for stimulation and are considered the “sweet spots”. This is due to the greater porosity, permeability, and brittleness combined with a lower UCS resulting in greater fracture initiation and, in the end, greater returns on hydrocarbon production.

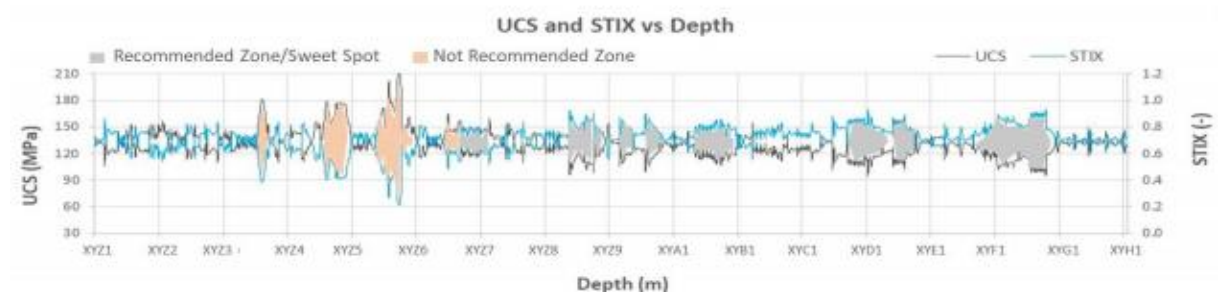


Figure 15: Using UCS and STIX for Recommended Zones (Tahmeen et al., 2017)

## CHAPTER III

### FIELD OF STUDY

In this chapter, the two reference wells are introduced in both a geologic and production sense to give a representation of the Caney shale. From background information of these two wells, quality assurance can guarantee accurate results for simulating a new well to be drilled and core analysis will aid in determining correlations prevalent for the Caney shale.

Drilled in 2014 and 2015 by Continental Resources, the Wynell and Garrett oil wells were targeted for the Caney Shale – a formation in the South-Central Oklahoma Oil Province (SCOOP) above the Woodford and Meramec formations near the Arbuckle Mountains. Landing in an upper Caney zone of the reservoir, the Wynell was stimulated with 3.76 million kilograms (8.3 million pounds) of sand and 1.4 million liters (375,000 gallons) of fluid, for a cumulative production of 255,000 barrels of oil and 24.8 billion cubic meters (876,000 MSCF) of gas with a 50% water cut. In comparison, the Garrett, which landed in a lower zone of the Caney – approximately 304.8 m (1000 ft) below the Wynell – was hydraulically stimulated with 2.2 million kilograms (4.8 million pounds) of sand and 999,349 liters (264,000 gallons) of fluid. This led to a cumulative oil production of 141,000 barrels of oil and 23.2 billion cubic meters (818,000 MSCF) of gas at a 25% water cut.

### 3.1 Garrett and Wynnell Data

The drilling data provided by Continental Resources for the Garrett and Wynnell contained operational parameters for drilling given in a time and depth-based format – intervals of either one foot or ten seconds. These parameters consist of the WOB, RPM, ROP, hook load, gamma ray, pump pressure, flow rate, and other operational parameters. A survey report containing the measured depth, inclination, azimuth, and dogleg severity provided a drilling outline of the kick-off point and lateral depth. A bit file summarizing the bits used for each section, the section depths, bit nozzle sizes, bit grade, and reason for tripping was provided along with a BHA file that contained the mass per length of the BHA and individual components for the assembly. Lastly, a daily drilling report was given that provides a day-by-day analysis of the drilling operation, mud weight details, lithology descriptions, and daily costs that provide a key understanding and potential quality of the drilling data.

The core data provided by Continental Resources for the Tomaney well drilled in the same area into the Caney shale provided the necessary tools for triaxial tests and analysis. With the help of Chesapeake Energy and the University of Pittsburgh, the triaxial test results for UCS, CCS, Poisson's Ratio, and Young's Modulus for various confining pressures were given.

#### 3.1.1 Location

The reference wells, Garrett and Wynnell, are within a mile of each other in adjacent sections. Located in Stephens County, the Garrett 1-36H (API# 351372713400) was geographically placed in Section 36-2S-4W, drilling north in the downdip of the formation. The Wynnell 1-31-3XH (API# 350192617200) was placed in Carter County in Section 31-2S-03W, drilling north into the downdip of the formation. In Figure 16, an overview of the reference wells is shown from Enverus DrillingInfo for visualization.



Figure 16: Location of Garrett and Wynell with Respect to the Tomaney

### 3.1.2 Well Path

Each reference well was drilled at approximately 60° inclination at a 9741' kick-off point (KOP) for the Wynell and a 10,901' KOP for the Garrett. The vertical sections for both wells were approximately 10,000' followed by 2-mile laterals. The Wynell, shown below in Figure 17, shows the well path and general direction for total depth. As for the Garrett, the well was drilled with an original and sidetrack section, represented in Figure 18. The sidetrack proved to have duplicate data from the original hole where quality control was necessary for data analysis.

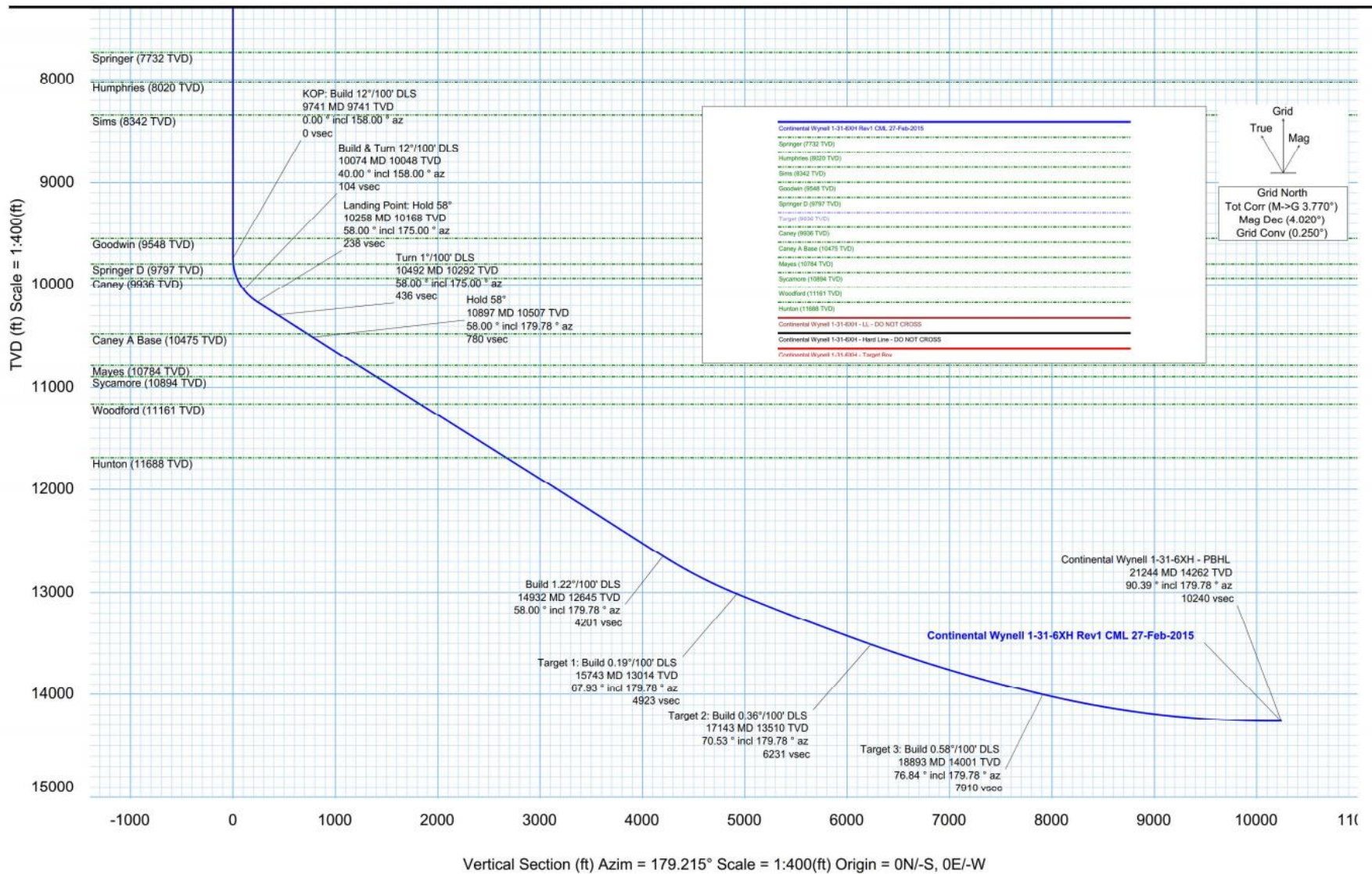


Figure 17: Wynell Well Path

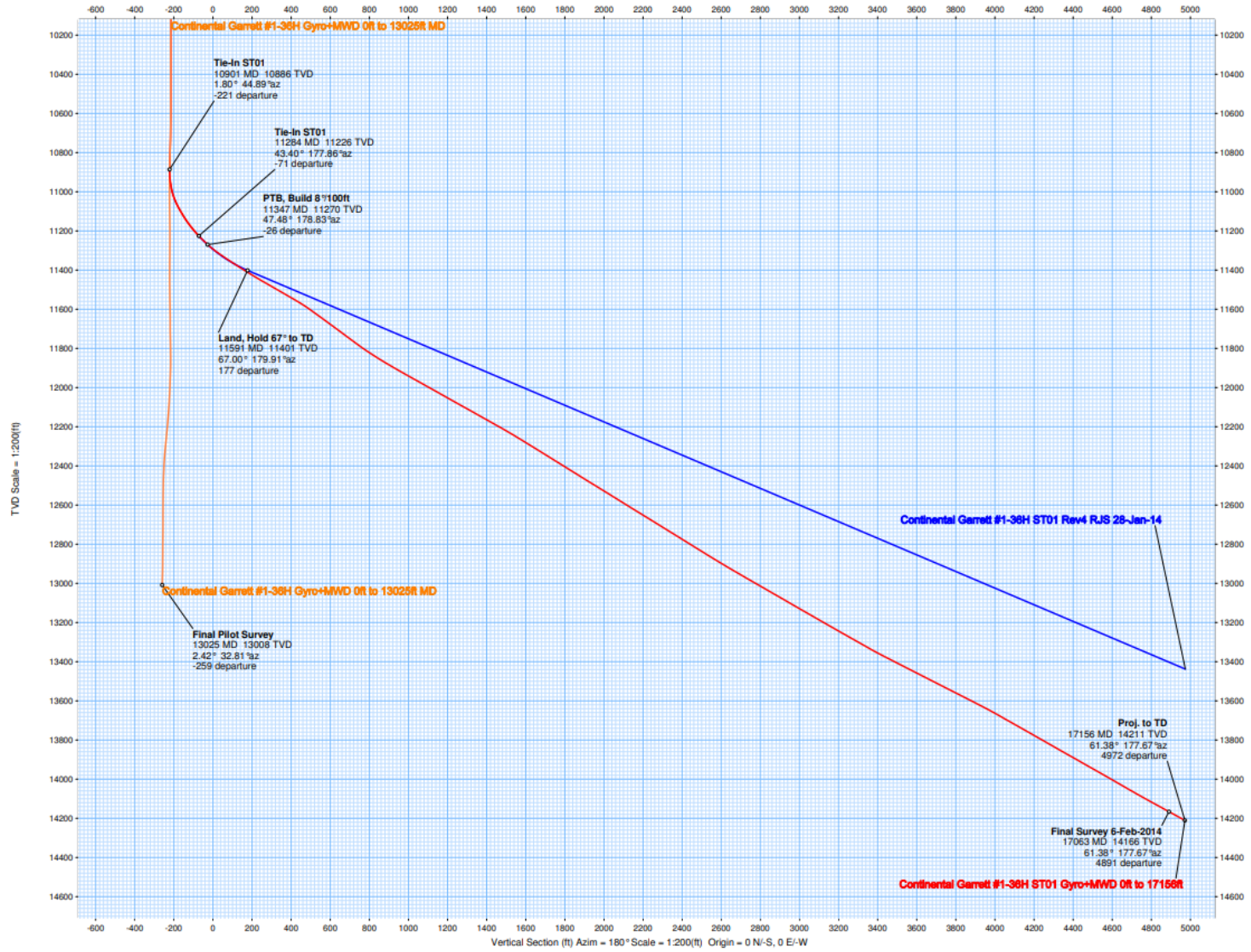


Figure 18: Garrett Well Path

### 3.1.3 Target Reservoir

The target zone for the Garrett was in the Reservoir 3 zone of the Caney, and Reservoir 2 for the Wynell displayed in Figure 19. Ductile zones surround Reservoir 2 with an oil-bearing zone in Reservoir 1 approximately 100' above. The well logs were compared, and Figure 19 is discussed further in the next section.

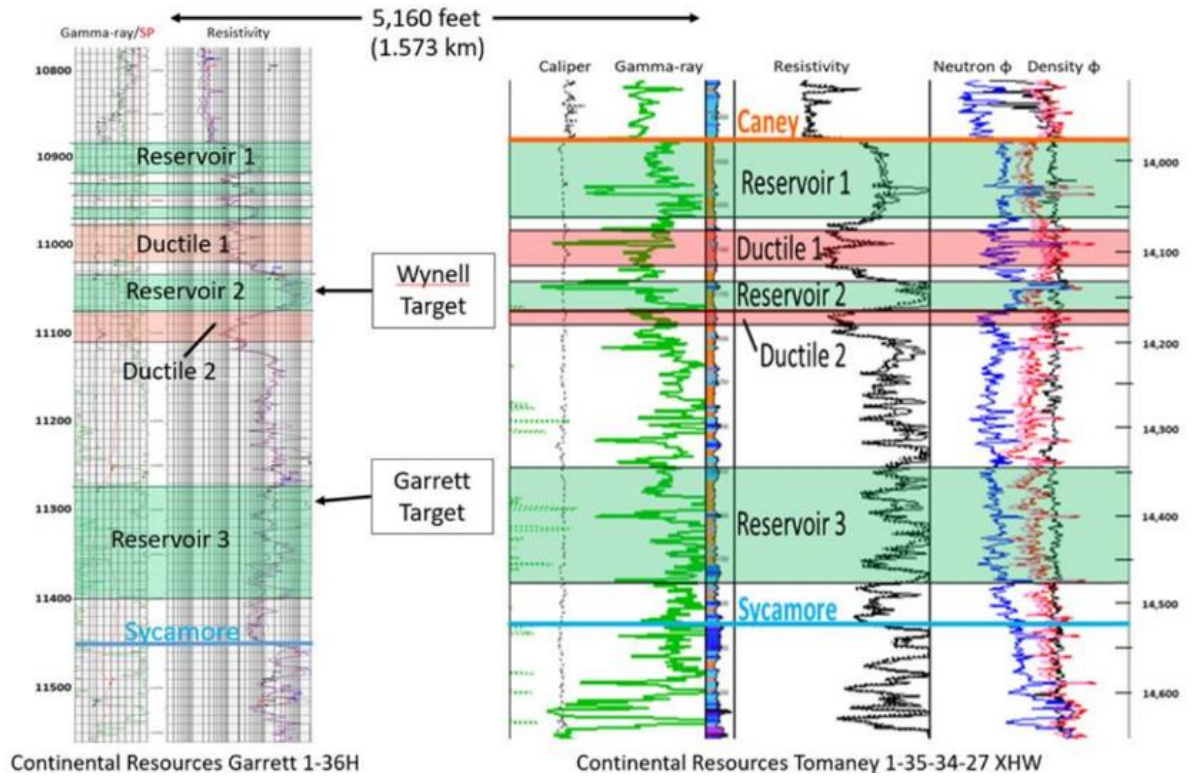


Figure 19: Target Depths for the Wynell and Garrett Compared to the Tomaney

### 3.2 Tomaney

Located in Section 35-2S-4WA, the Tomaney (API# 351372748100) provided a Caney core sample where experiments could be conducted. The well provided the core analysis for triaxial experiments, where UCS, CCS, Young's Modulus, and Poisson's Ratio were found. The well logs for the Tomaney were then correlated to give an approximate depth of the reservoir cores that were extracted. In Figure 19, the Tomaney gamma ray log is compared to the Garrett,

showing a reservoir height difference of about 3,000'. This is due to the dip angle of the Caney and its relation to the wells. A sample photo of the Caney Shale from the Chesapeake (CHK) core lab is represented below in Figure 20.

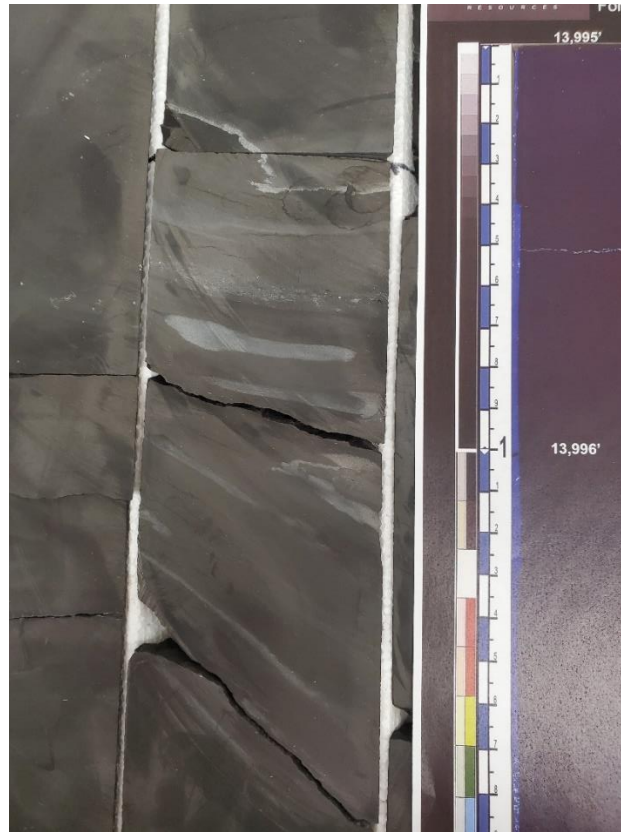


Figure 20: Caney Core from CHK Labs

The core was tested under various confining pressures for triaxial properties at the University of Pittsburg. The confinement test was at 90 °C, while the UCS tests were at room temperature. The data below, Tables 3 and 4, represent the data University of Pittsburg compiled for a target zone of Reservoir 3. This is important when making key correlations between CCS, UCS, porosity, permeability, Poisson's Ratio, and Young's Modulus. As confining pressure increases, the compressive strength or CCS increases as well. The Young's Modulus and Poisson's Ratio vary and will be further explained in Chapter 5.

### Reservoir 3

Triaxial Properties at 90°C:

Sample	Confining Pressure (psi)	Compressive Strength (psi / MPa)	Young's Modulus (Mpsi / GPa)	Poisson's Ratio (-)
R3-V-500HCS-2 *	500	19,667 / 135.6	4.26 / 29.33	0.179
R3-V-1500HCS-3	1500	20,508 / 141.4	3.69 / 25.47	0.164
R3-V-3000HCS-5	3000	22,559 / 155.5	4.40 / 30.32	0.194

Table 3: Reservoir 3 Triaxial Properties at 90 °C

Measured UCS at Room Temperature:

Sample	UCS (psi)	UCS (MPa)
1	11,987	82.7
2	12,845	88.6
3	11,877	81.9
4	18,259	125.9
Average	13,742	94.7

Table 4: Reservoir 3 Uniaxial Properties at Room Temperature

### 3.3 Galloway

From the thesis herein, a completion optimization technique is displayed using raw drilling data from the Garrett and Wynell reference wells for selective stimulation of the new well to be drilled. This new well, the Galloway, will be drilled between the Tomaney and Garrett into the Reservoir 3 zone of the Caney. The Galloway will land at 13,800' and kick-off to a 2-mile lateral. The well path will be at a downdip of 2-3° so a near perfect 90° horizontal can be modeled. The well will drill into the strike of the formation, as opposed to the Garrett and Wynell drilling along the formation. Furthermore, when considering the stimulation index for the new well, brittleness is the only key factor when selecting optimal zones of completion, according to Continental Resources.

## CHAPTER IV

### METHODOLOGY

In this chapter, the methodology is presented where necessary corrections to UCS and depth are shown as well as the inputs into D-WOB and D-ROCK. The data are then quality controlled and the correlations for UCS, porosity, and permeability are compared to other shale plays to give a representation of the similarities of the Caney Shale.

#### 4.1 Corrections

##### 4.1.1 Temperature

In Section 2.6, Mohamadi and Wan (2016) presented a UCS difference between downhole and surface temperature for triaxial tests. With a proposed temperature scaling law and capturing both thermal weakening and strengthening of a material, Mohmadi and Wan presented Figure 21 where an exponential trend shows the effect of temperature on UCS. In general, as temperature increases, the UCS will decrease approaching zero. The opposite is true for when temperature decreases. This profile occurs when an increase in temperature results in a decrease in yield stress, causing the yield strength to decrease.

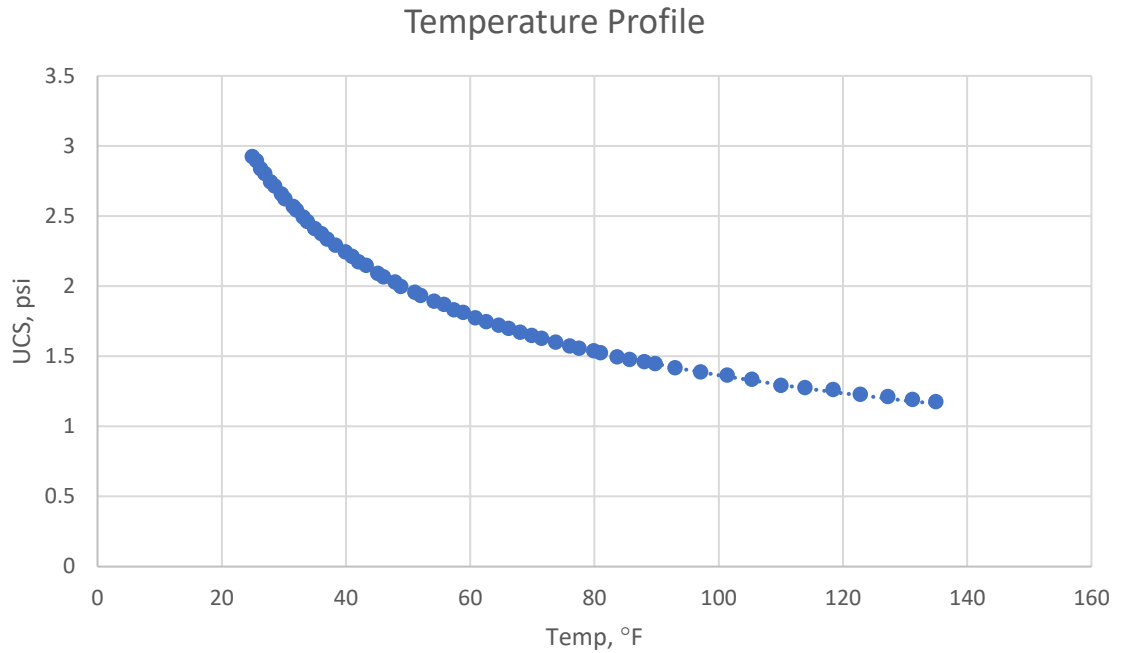


Figure 21: Mohmadi and Wan Temperature Profile Compared to UCS (Mohamadi and Wan, 2016)

Taking this into account, and the triaxial results being done at room temperature, a reduction in UCS values from core testing must be done to account for the temperature differential. For triaxial testing, UCS was done at room temperature, or 20 °C, and CCS was done at 90 °C. The sonic logs used for calculating UCS were done at 107 °C – using a typical geothermal gradient of 1.3 °F / 100 ft for the Anadarko Basin. To compute the required percent reduction in UCS, Equation 43 was used where, according to Mohamadi and Wan (2016), the difference had to be greater than 30%.

$$30 \times \frac{107 - 20}{90 - 20} = 37\% \text{ reduction in UCS} \quad (43)$$

Reducing the UCS values from triaxial tests by 37%, the temperature effect is now considered, and comparisons could be made. To compare this difference, Figure 22 is represented. The UCS from triaxial core data before the 37% reduction is plotted in blue, the UCS after reduction is plotted in orange, and the UCS derived from Onyia’s correlation for compressional travel time in Equation 3 is plotted in gray. Notice the dramatic decrease from UCS found during triaxial tests and the similarities between log-based data and the UCS reduction value. This proves a reduction in UCS was necessary and will be used for further comparisons and correlations.

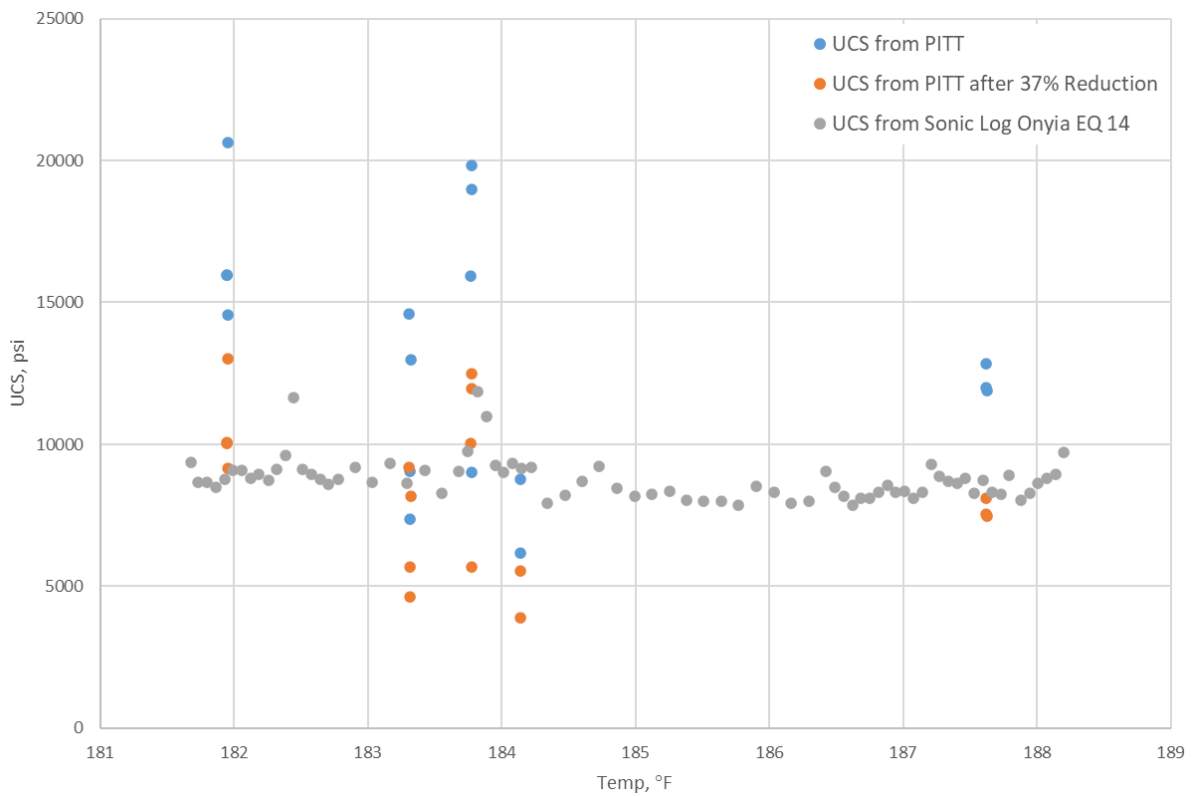


Figure 22: UCS vs Temperature for Reservoir 1, 2, and 3 Comparing 37% Reduction in UCS

#### 4.1.2 Depth

To account for the distance between the rig floor and ground elevation, a depth shift needed to be made when taking compressional travel time from sonic. Shifting the depths by 25 ft and correlating the specific sonic values, proved to be necessary when comparing UCS to percent reduction and to other correlations. Figure 23 represents this value, where core tests were compared to various correlations from Onyia, Andrews, Horsrud, and Olea. Due to the difference in UCS to Andrews' correlation, Onyia's correlations were used for similarity to the Tomaney core data.

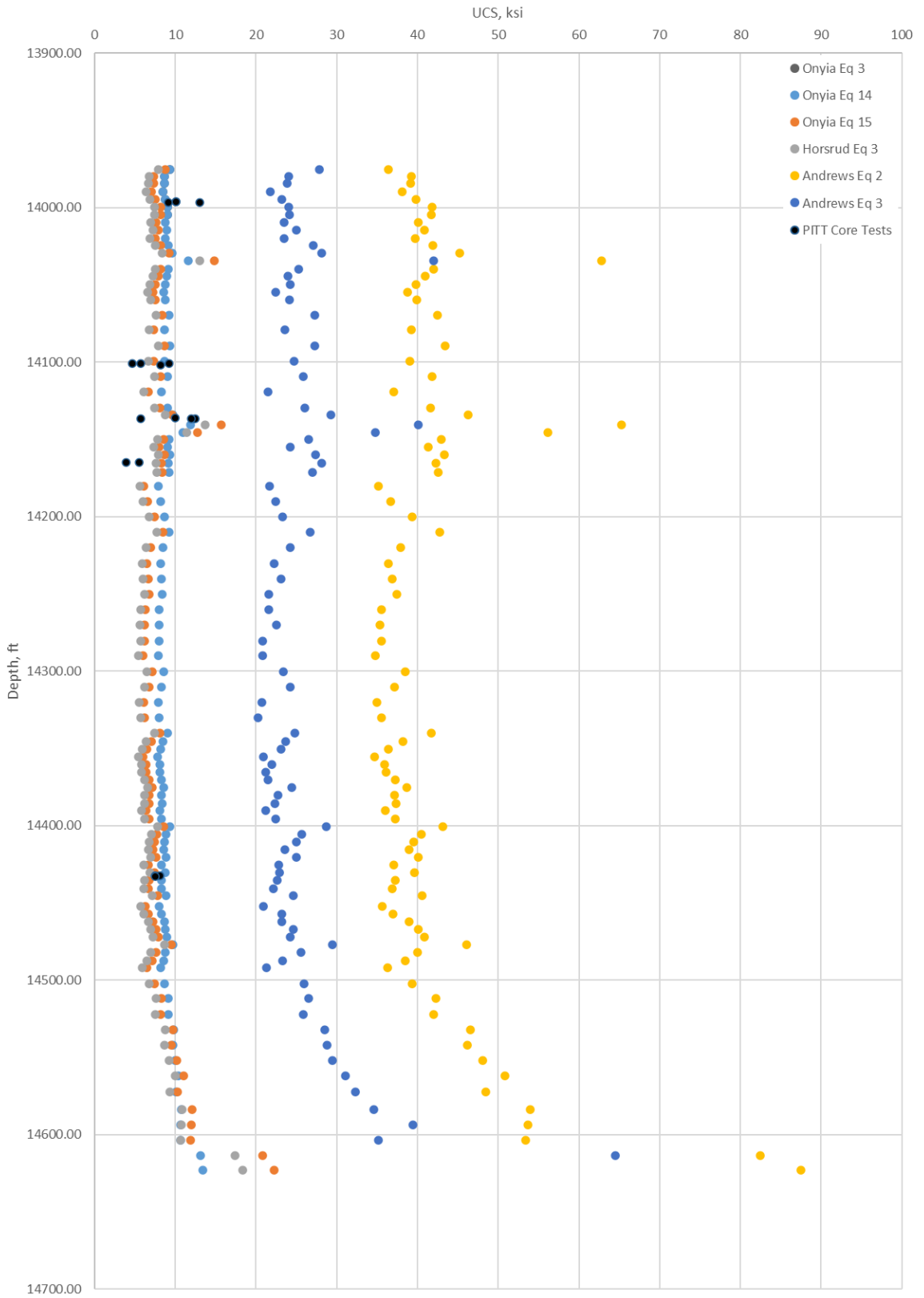


Figure 23: Varying UCS Correlations Compared to Triaxial Results

## 4.2 D-Series Inputs and Quality Control

When using the D-Series software, various inputs must be made, then quality controlled for accurate results. These inputs include sheave efficiency, hook load, number of lines, and files as referenced in Section 2.8.2. In the general inputs (hook load, sheave efficiency, number of lines), common values were found or extrapolated from the drilling data. From drilling rig specifications, 96% sheave efficiency and 10 lines were used along with 40 klbf hook weight (found when plotting hook load vs bit depth and taking the minimum). A common pore pressure was calculated in relation to overbalanced drilling, where pore pressure is 0.3 ppg less than mud weight. Overbalanced drilling was used to prevent reservoir fluids from entering the wellbore and to prevent kicks. For quality control of the drilling data, “non-drilling” data which includes tripping in and out of the hole were excluded to prevent false data, where the RPM would drastically decrease to a null or -999 value. To display this effect, simply plot bit depth vs hole depth to see and exclude tripping time, pipe change, or drilling out cement plugs set for casing intervals. The Wynell was drilled with a single hole to TD, while the Garrett was drilled with an original hole till about 13,400’ MD, then pulled to KOP where a sidetrack was drilled to TD, as represented in Figure 18. When evaluating the time and depth-based drilling data for quality control, the Garrett had duplicate data from the KOP of 10,901’ MD to 13,400’ MD. The original data had to be taken out so only the sidetrack remained in the data files.

Next, the data files were converted to text files to be inputted into D-WOB and D-ROCK. For D-WOB, the time and depth-based drilling files were inputted. These files contained the necessary operational inputs for the inverted ROP model to run. While in the D-WOB window, a quality control feature can be used where the depth-based file can be quality controlled. Null values can be taken out, tripping in/out or making connections can be averaged over a number of data points

to avoid errors, and smoother trends can be formed where the data are coherent and readable. The BHA file was obtained from a BHA analysis report from Continental Resources, where each BHA was outlined and described. Drill pipe, collars, motor or rotary steerable specifications, and stabilizers were found in the file. The components had to be averaged according to weight, while the length had to be summed over the full length of the BHA. The survey file included depth, azimuth, inclination, and dogleg angle where little quality control was needed. The two outputs for D-WOB are a drill file that contains quality controlled operational parameters and a friction coefficient. For inputs into D-ROCK, the drill file and an added bit file are used. The bit file contains the type of bit, nozzles, number of blades, cutter sizes, etc., while also containing a motor constant in rev/gal. The motor constant, available only if a section ran a motor as opposed to a rotary steerable, was found in the BHA file or daily drilling report. The motor constant is used in D-ROCK by multiplying the constant by flow rate, then adding the speed to overall RPM of the drillstring. This is important to add when considering the effect of RPM on rock strength, where the bit RPM is a required input.

#### 4.3 Correlations

Initial correlations used the triaxial core data with the 10' depth shift and 37% reduction in UCS to compare the Tomaney core for Reservoir 3 to other shale formations. First, permeability vs UCS is compared to the Montney, Barnett, and Fayetteville Shale to gain a brief understanding of how the Caney compares to other reservoirs. Then, porosity vs UCS is compared to other correlations, as presented by Cedola et al. (2017), and finally, a comparative view of permeability vs porosity. For a general trend, the Tomaney core data aligns more with the Fayetteville Shale, below the Montney and above the Barnett Shale trends, when comparing UCS to porosity and permeability. For porosity vs UCS, the general trend lies below the correlations for Horsrud, Chang, and Lashkaripour, suggesting a lower percent porosity per given UCS for each correlation. The range for UCS lies between 50 and 100 MPa (7250 – 14,500 psia), while

porosity is between 1 – 5%, and permeability between 0.000036 – 0.000294 mD (36 – 294 nD). Comparing the figures to ensure validation, in Figure 24, the general trendline begins at 57 MPa and 0.00023 mD. Using Figure 25 and 57 MPa, the porosity lies at approximately 3.1%. This will determine the relation between porosity and permeability as 0.00023 mD to 3.1%, which can be validated in Figure 26.

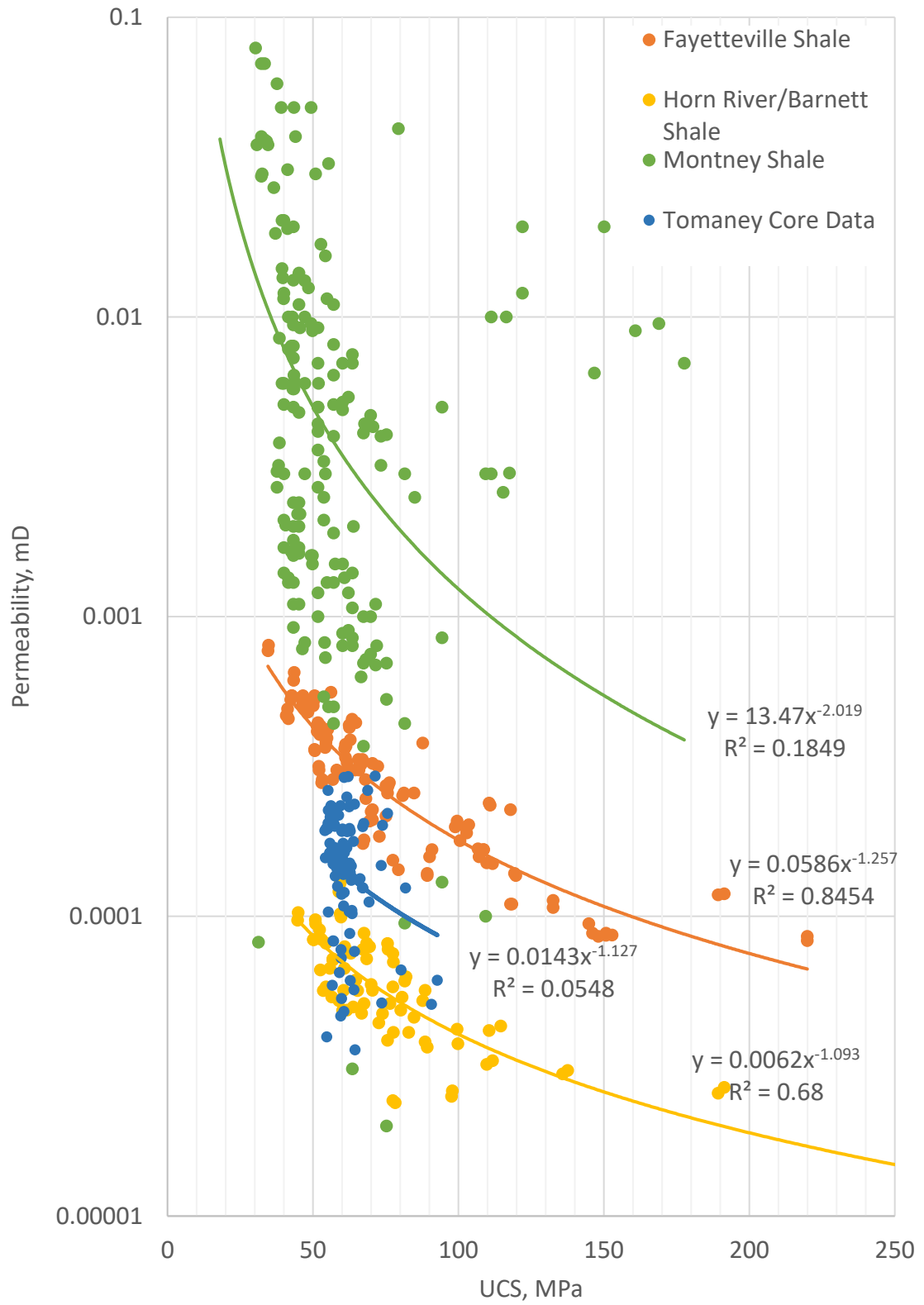


Figure 24: Permeability vs UCS for the Tomaney Core and Other Shale Plays

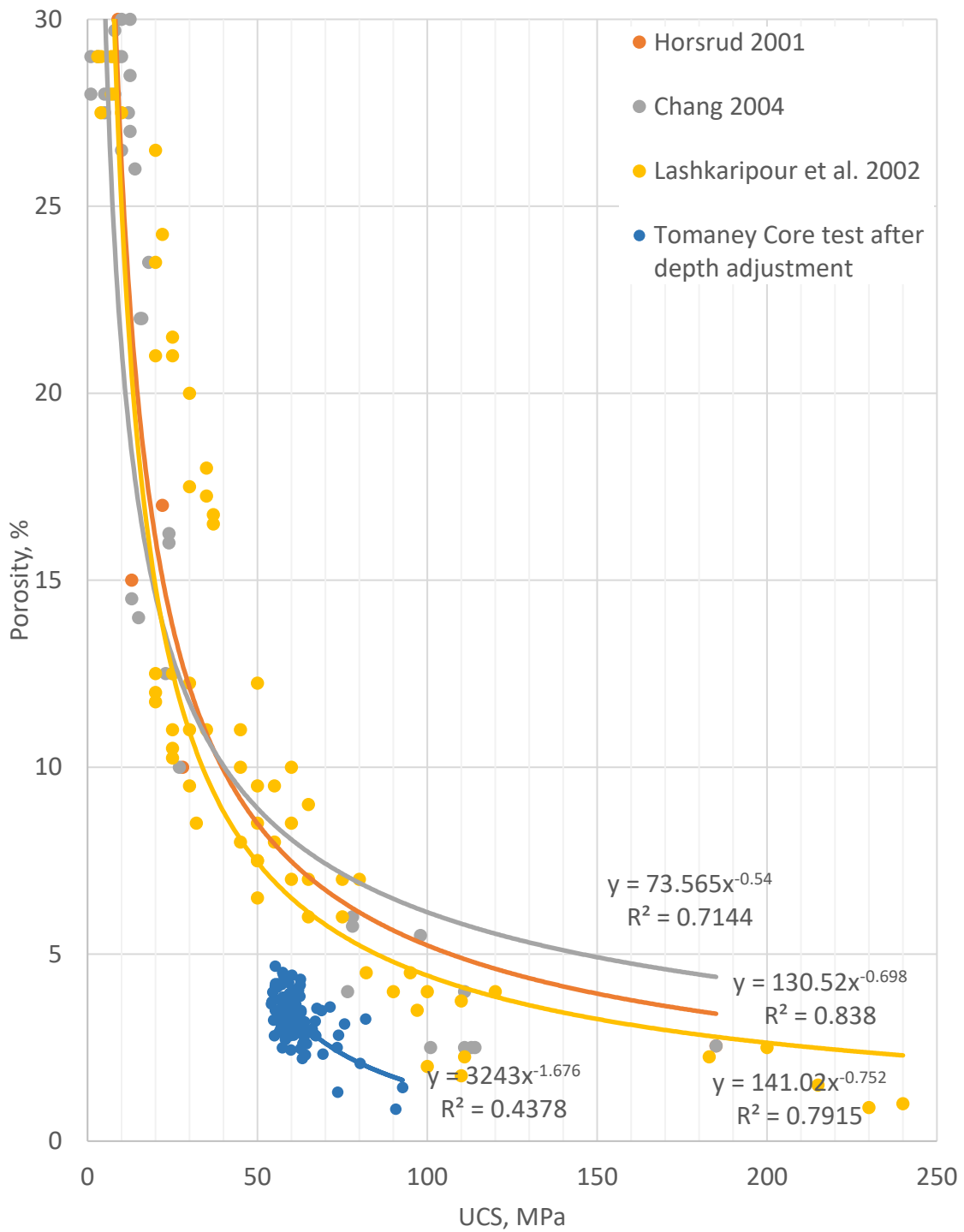


Figure 25: Porosity vs UCS for the Tomaney Core and Other Correlations

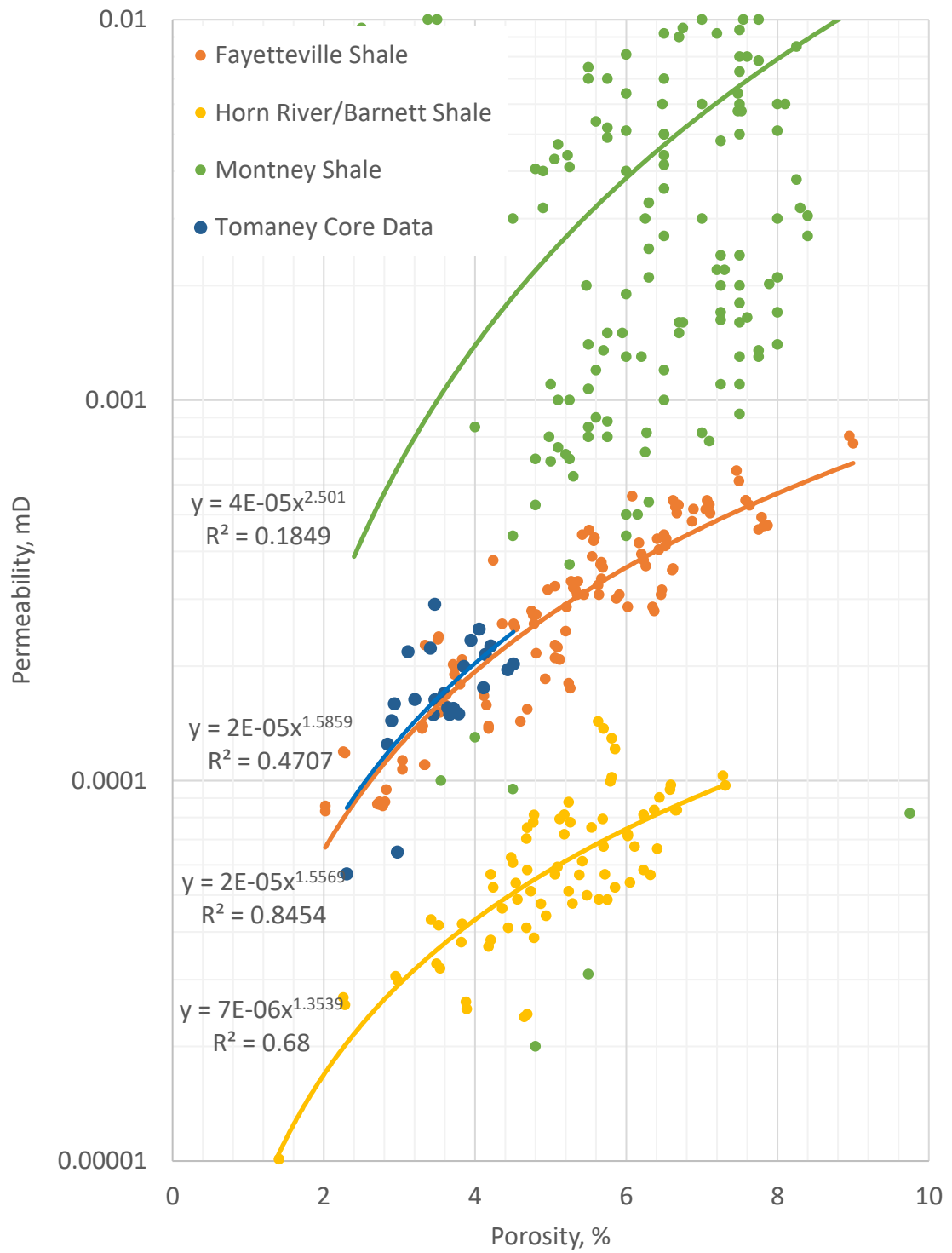


Figure 26: Permeability vs Porosity for the Tomaney Core and Other Shale Plays

## CHAPTER V

### FINDINGS

In the chapter, the key findings for correlations between CCS and confining pressure, UCS and porosity, and permeability to porosity are presented. Formation constants are then derived from triaxial tests and inputted into D-WOB for correct correlation. The initial outputs for D-WOB, friction and surface WOB, are then compared to downhole WOB and explained. Furthermore, through use of D-ROCK, the geomechanical property log for the Garrett lateral is shown, due to its interaction with Reservoir 3. The Caney Shale data are then compiled and compared to other field results for productive shale formations. Lastly, the stimulation index (STIX) is derived through multiple equations, with the last being requested for selective stimulation from Continental Resources.

#### 5.1 Correlations

Before entering data into D-WOB and D-ROCK, correlations must be made for correct geologic results. The default input into D-WOB is the formation constants,  $a_E$ ,  $b_E$ ,  $a_s$ , and  $b_s$  for CCS, UCS, confining pressure, and Young's Modulus, and  $k_1$ ,  $k_2$ ,  $k_3$ , and  $k_4$  for porosity and permeability for the Eagle Ford shale. Through regression analysis presented in this section, the constants are derived, and the process is shown for the Caney.

### 5.1.1 Porosity and UCS

The correlation between Porosity and UCS is imperative in understanding the Caney structure and formation. Detailing the rate at which porosity decreases according to increasing UCS is a key input into D-WOB, to not only calculate the downhole WOB, but to also predict porosity for each UCS interval. This prediction will ultimately aid in selective stimulation design and criteria for hydraulic fracturing. Figure 27 displays the correlation between Porosity to UCS calculated from Onyia's Equation 3 for the Tomaney core in Reservoir 3. The trendline for the data,  $y = 231.57x^{-1.95}$  where  $y$  is the porosity in percent and  $x$  is the UCS in ksi, represents Equation 40 from Section 2.8.1. In this case, 231.57 is  $k_1$  and -1.95 is  $k_2$ . To align the values in D-ROCK after calculating UCS, the constants had to be adjusted for a more accurate fit when comparing to Chesapeake petrophysical averages to 41.03 for  $k_1$  and -0.636 for  $k_2$ . These values are then inserted into D-WOB for formation constants for the Caney.

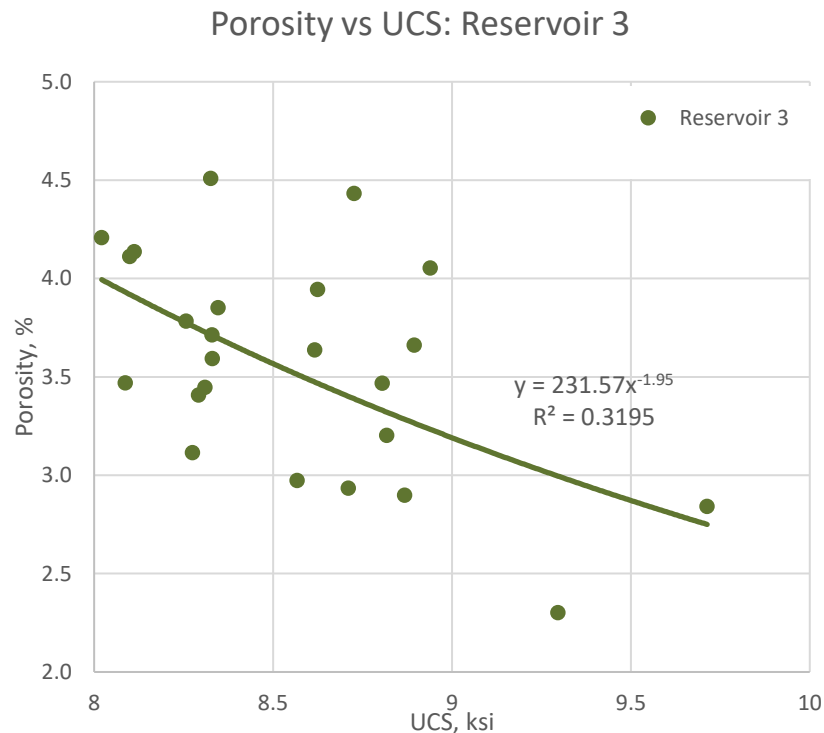


Figure 27: Porosity vs UCS for Reservoir 3

### 5.1.2 Permeability and Porosity

When correlating permeability to porosity, the same approach is taken as mentioned in Section 5.1.1 where permeability is plotted against porosity and a trendline will detail the correlation constants. Figure 28 explains this effect where the trendline equation is  $y = 23.08x^{1.586}$ . A previously mentioned in Equation 41 of Section 2.8.1, the correlation constants are 23.08 for  $k_3$  and 1.586 for  $k_4$ . This can then be inputted into D-WOB for formation constants.

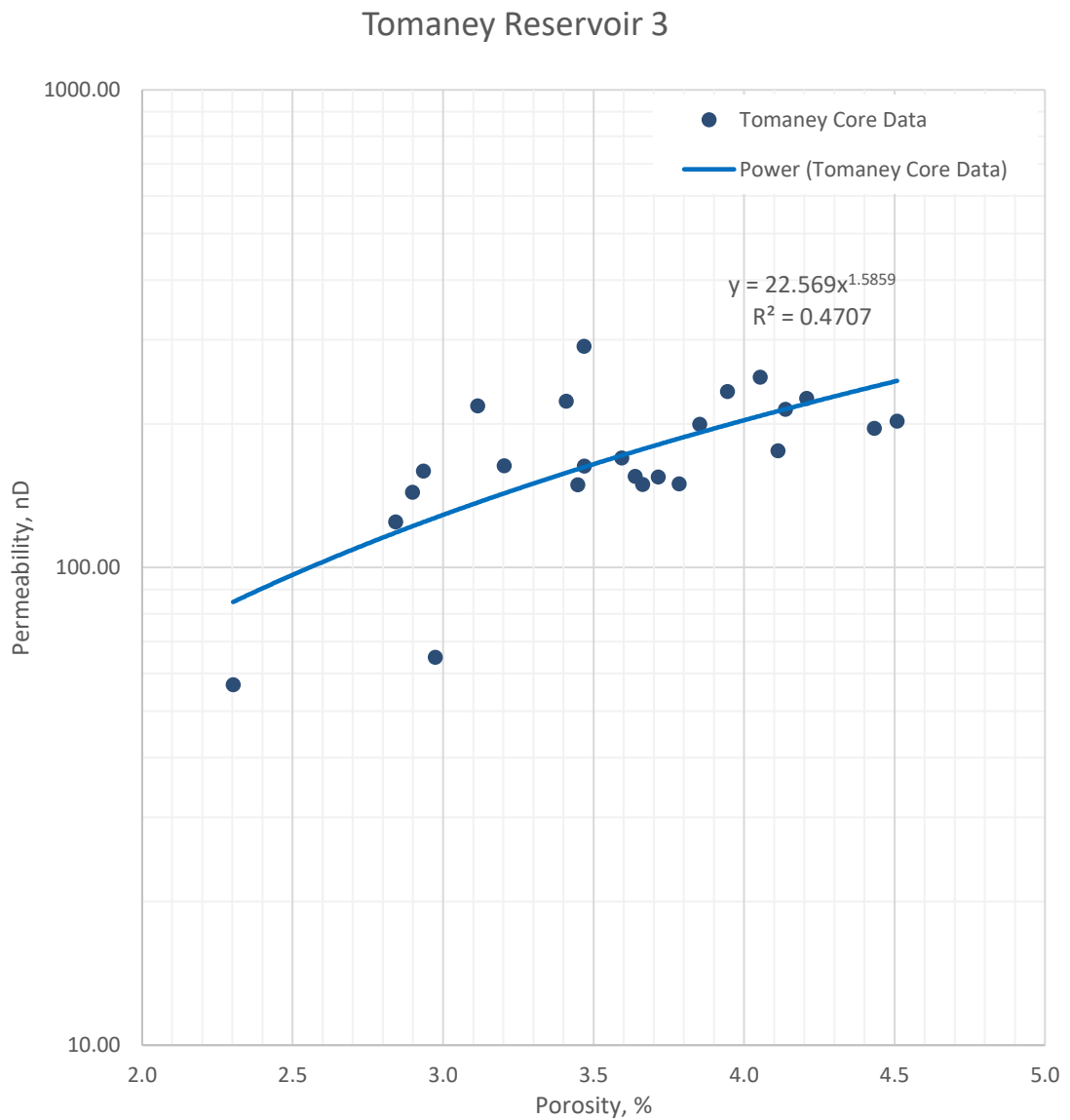


Figure 28: Permeability vs Porosity for Reservoir 3

### 5.1.3 Compressive Strength and Confining Pressure

As porosity, permeability, and UCS were correlated, confining pressure to compressive strength can be modeled the same way. From the triaxial data in Tables 3 and 4 and equating zero confining pressure to UCS, and after reducing the values by 37% and converting to MPa, the formation constants,  $a_s$  and  $b_s$ , can be inputted into D-ROCK. The first three data points were taken whereas the fourth UCS value at 18,259 psi was void due to errors within the triaxial test. The confining pressure and CCS were then converted to MPa and inserted into the D-WOB calculator for formation constants as presented in Figure 30. The calculator then displays the values of 1.323071 for  $a_s$  and 0.115337 for  $b_s$ . For quality control, the correlation constants had to be adjusted to fit for UCS while considering Poisson's Ratio to 0.601 for  $a_s$  and 0.404 for  $b_s$ . This change accounted for the differential in downhole WOB to surface WOB, as explained in Section 5.2.2.

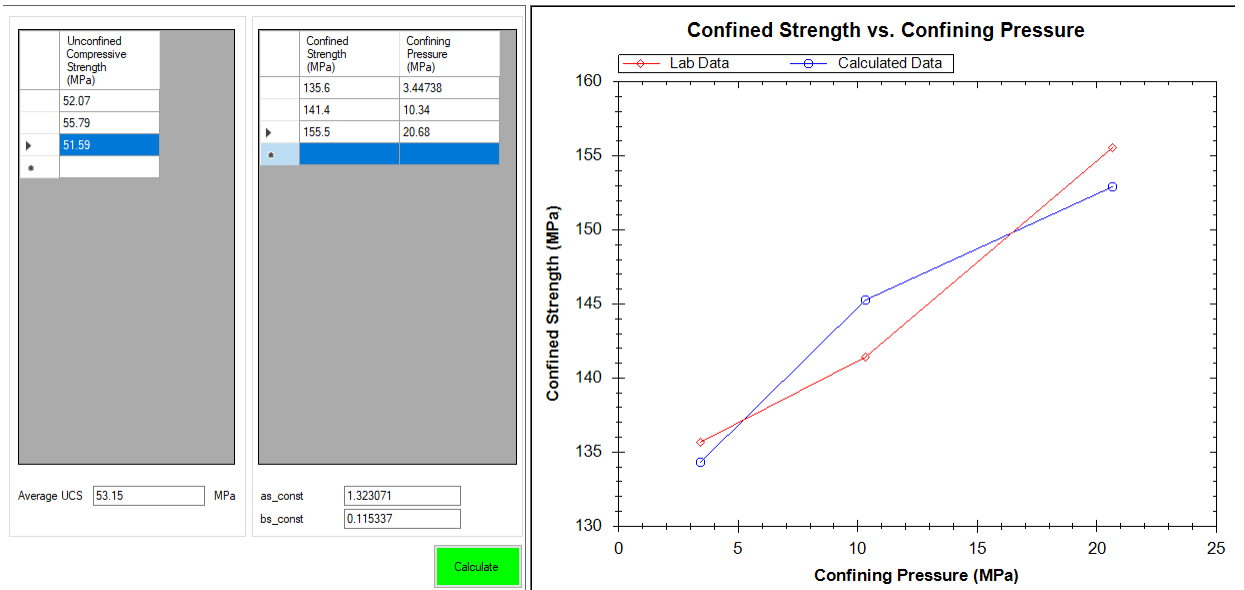


Figure 29: Correlation between Strength and Confining Pressure

### 5.1.4 Young's Modulus and Confining Pressure

Likewise, for Young's Modulus and Confining Pressure, the same approach is taken. Equation 38 from Section 2.6 is used where Young's Modulus, confining pressure, and confined compressive strength are inserted into the D-WOB calculator for finding the constants  $a_E$  and  $b_E$ . In this case, for Reservoir 3 of the Caney, as represented in Figure 30,  $a_E$  is 0.233995 and  $b_E$  is -0.074698. As the constants had to be adjusted for CCS and confining pressure, the same must be done here to better fit the raw data from triaxial core tests. The correlation constants were adjusted to 0.441 for  $a_E$  and -0.16 for  $b_E$ .

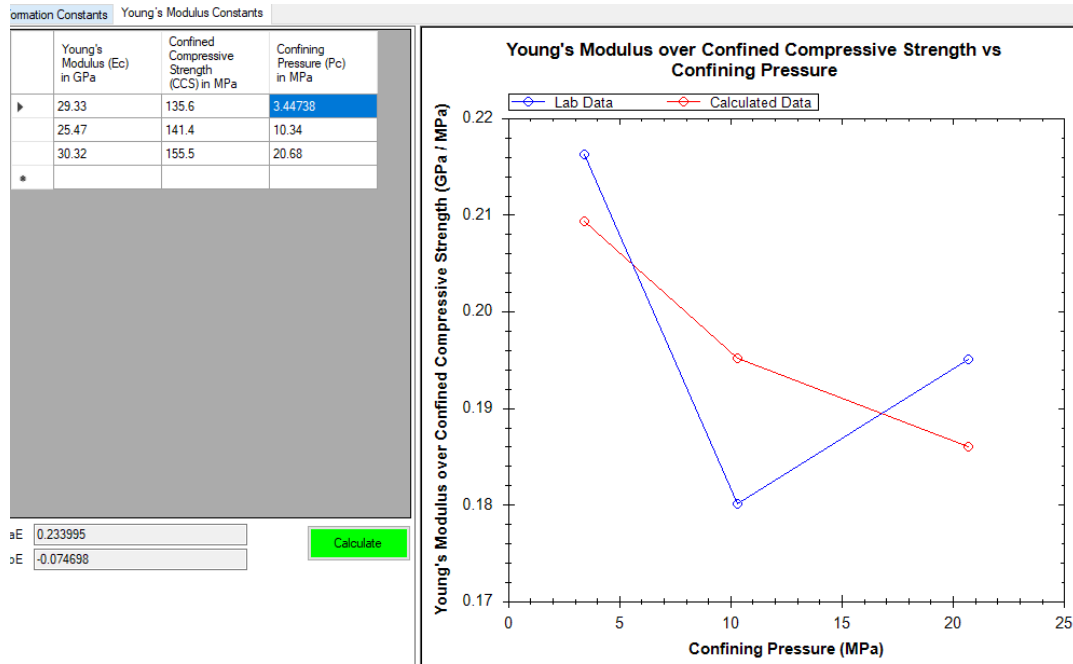


Figure 30: D-WOB Correlation between Young's Modulus Over CCS vs Confining Pressure

### 5.1.5 Overview of Constants

This section concludes the inputs and quality control needed for D-WOB to run properly and efficiently. The formation constants generated can further be represented in Figure 31 where direct correlations are made and confirmed. In general, there is a direct increasing correlation with porosity and permeability, such that an increase in one lead to an increase in the other. Conversely, as permeability decreases, UCS increases due to confinement and grain compaction. As for porosity and UCS, the same can be shown, but at an increasing rate. Porosity drastically decreases with the slightest decrease in UCS. Poisson's Ratio and UCS present as a near linear line, where decreasing Poisson's Ratio leads to an inversely proportionate UCS value. The correlation constants are then outlined in Table 5 where the Eagle Ford and Caney are compared.

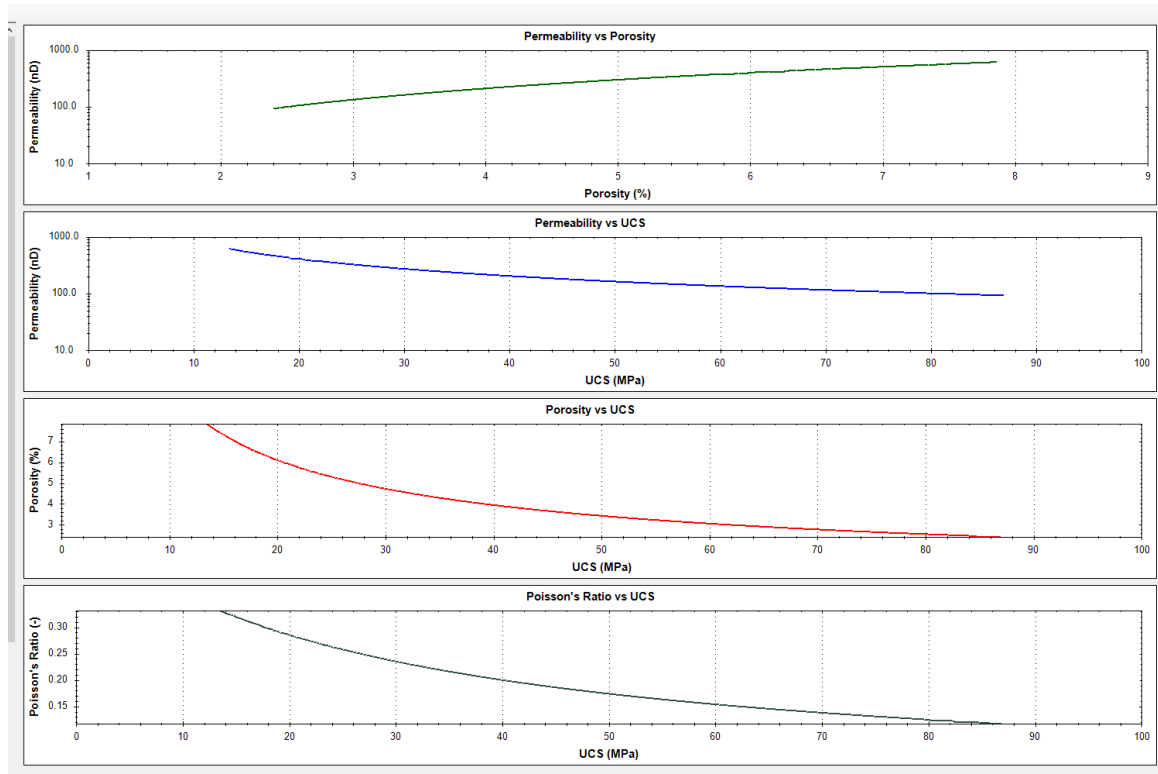


Figure 31: Overview of Trends Generated from D-ROCK

Table 5: Formation Constant Comparison of the Caney to Eagle Ford Shale

	Eagle Ford	Caney
Constant ID	Formation Constant	Formation Constant
as	0.04078	0.601
bs	1.0396	0.404
ae	0.4209	0.441
be	-0.16773	-0.16
kpor1	92.529	41.03
kpor2	0.636	0.636
kprm1	6.9302	23.08
kprm2	2.5313	1.586

## 5.2 Outputs

For the outputs herein, the Garrett lateral section is shown, due to its impact with Reservoir 3 and the detail of data, as opposed to the Wynn lateral and data for the total depths. To begin, D-WOB outputs are presented with a friction analysis, then a comparison of the surface WOB to downhole WOB is shown. From there, D-ROCK is then used to calculate the strength log for the lateral, and display the stimulation parameters of UCS, porosity, permeability, and Young's Modulus, and Poisson's Ratio. The data are then averaged with the maximum and minimum values compared to other shale plays for a comprehensive overview of the comparative nature of the Caney shale. Lastly, a stimulation index is shown that quantifies the likelihood of greater fracturability zones within the reservoir for various equations.

### 5.2.1 Wellbore Friction

The friction coefficient displays the relative friction along the wellbore. This can be used for quality control of the data and explanation where points are too high or too low. An example of this is in Figure 32 where the friction coefficient – outputted from D-WOB – helps explain certain depth intervals. At approximately 12,000', the well is coming out of the bend and starting to go

lateral which incurred a 60° inclination – according to the survey data at 11,887'. This will make the friction greatly increase for the bend, then come back down when going lateral.

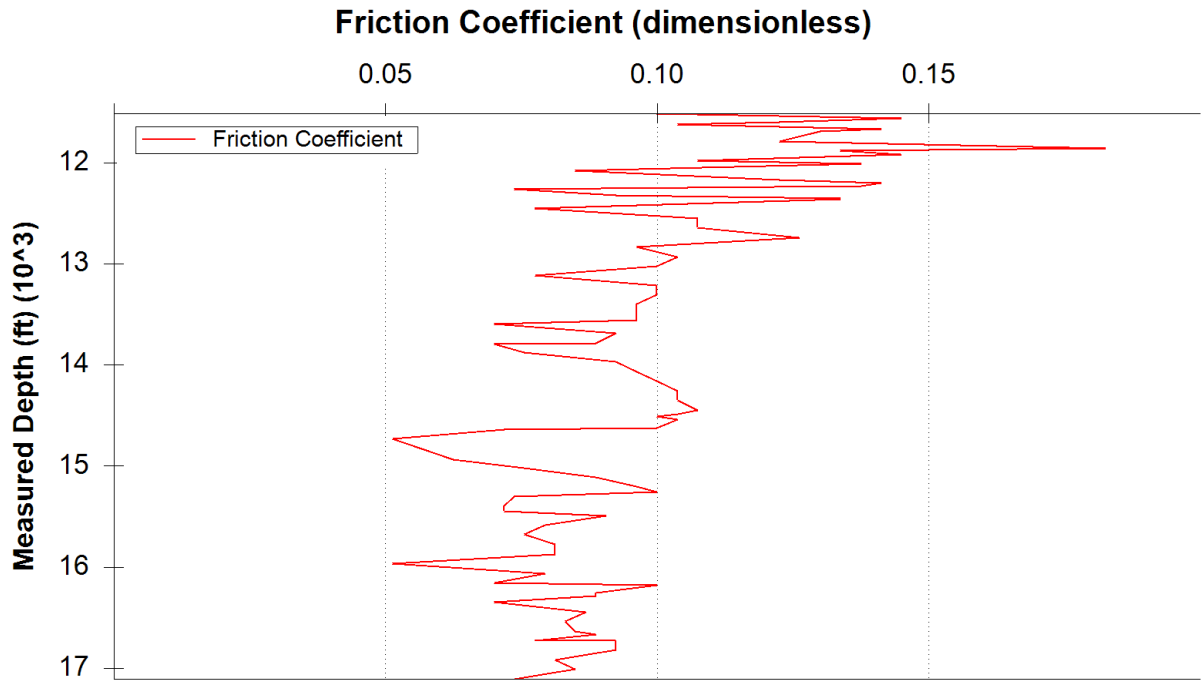


Figure 32: Depth vs Friction Coefficient for the Garrett Lateral

### 5.2.2 SWOB vs DWOB

Along with the friction coefficient, the surface WOB and downhole WOB can be compared to detail the difference between WOB in the lateral outlined in Figure 33. As the well deviates and is now horizontal, the pipe will lie on the wellbore wall causing the downhole weight to be less than the surface weight. For the Garrett, there is about a 5-10 klbf WOB difference between surface and downhole WOB. For a vertical well, this difference is nonexistent, where the DWOB in Equation 39 is equivalent to the surface WOB, therefore, giving a true value for CCS. For the Garrett, the lateral section creating the WOB difference between surface and downhole will decrease the value for CCS, due to Equation 39 containing DWOB rather than SWOB. A

correction in the regression constants for the CCS correlation will need to be made to account for this differential.

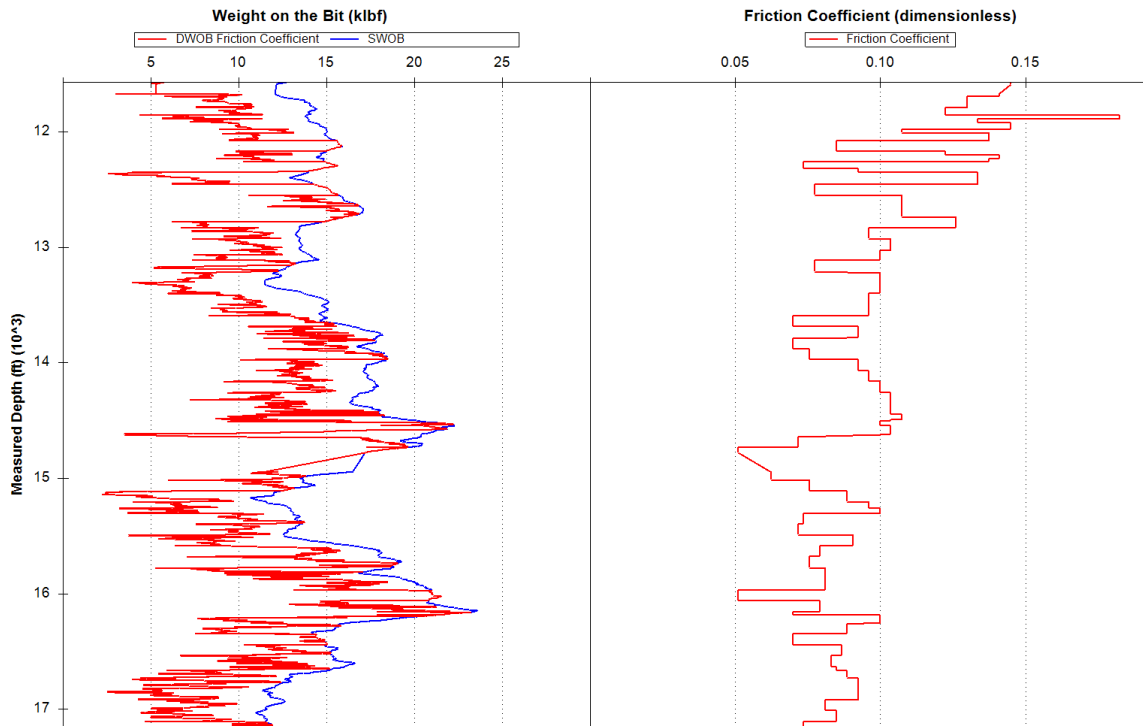


Figure 33: Surface WOB vs Downhole WOB for the Garrett Lateral

### 5.2.3 Geomechanical Strength Log

The geomechanical strength log is the primary output from D-ROCK that is used to correlate selective stimulation depths to rock mechanical properties. The strength log, given on a foot-by-foot basis, defines the intervals of UCS, porosity, permeability, Poisson's Ratio, and Young's Modulus given in Figures 34, 35, and 36. For interpretation, intervals with high UCS, high Young's Modulus, low permeability, low porosity, and low Poisson's Ratio should be avoided for stimulation. In Figure 35, the depths of 13,800' or 14,500' where UCS is approaching its peak, should be avoided. Similarly, zones with low UCS, low Young's Modulus, high permeability, high porosity, and high Poisson's Ratio should be stimulated. The depths of 12,900' and 15,100' describe this result. From the Caney geomechanical log, a comparison to other shale plays can be

conducted for each property to detail the similarities and differences of the Caney. Furthermore, combining these geomechanical properties, a stimulation index (STIX) factor can be developed and normalized for complete selective stimulation design in accordance with Continental Resources. As such, a complete brittleness index profile along the Garrett lateral is presented in Appendix A detailing the points of high/low brittleness. This is extremely useful when considering the stimulation index presented in Section 5.4.

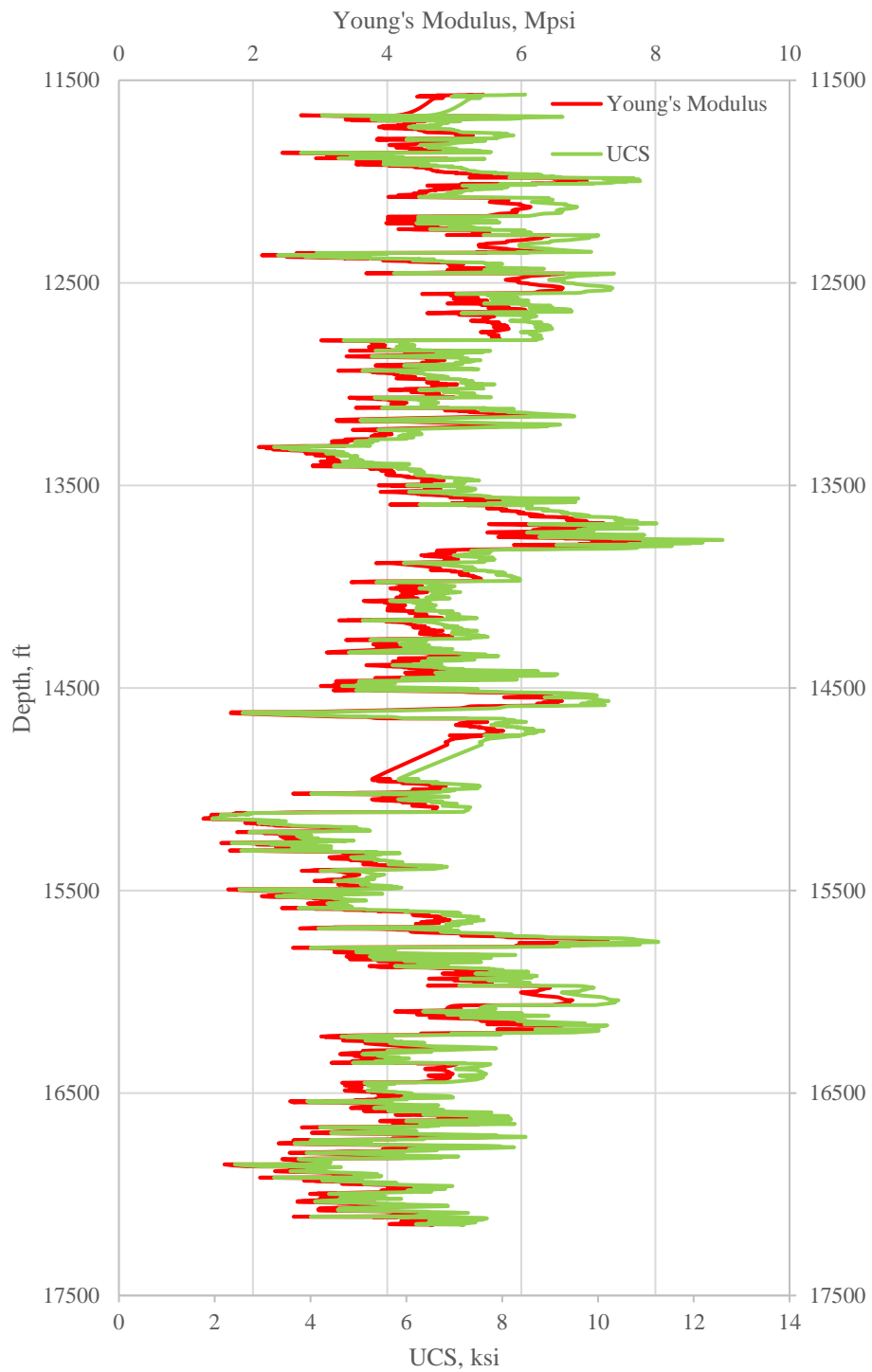


Figure 34: UCS and Young's Modulus vs Depth

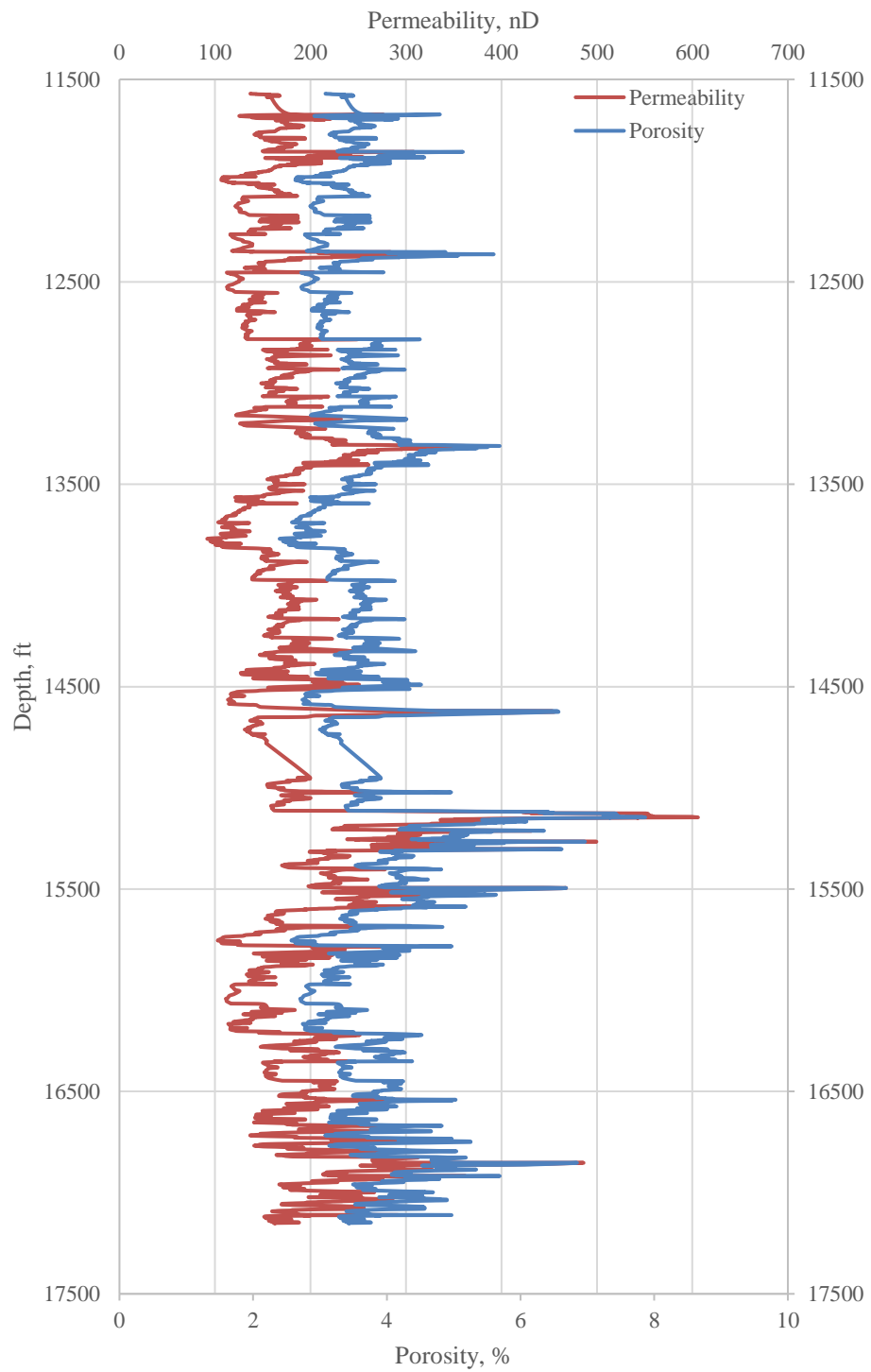


Figure 35: Permeability and Porosity vs Depth

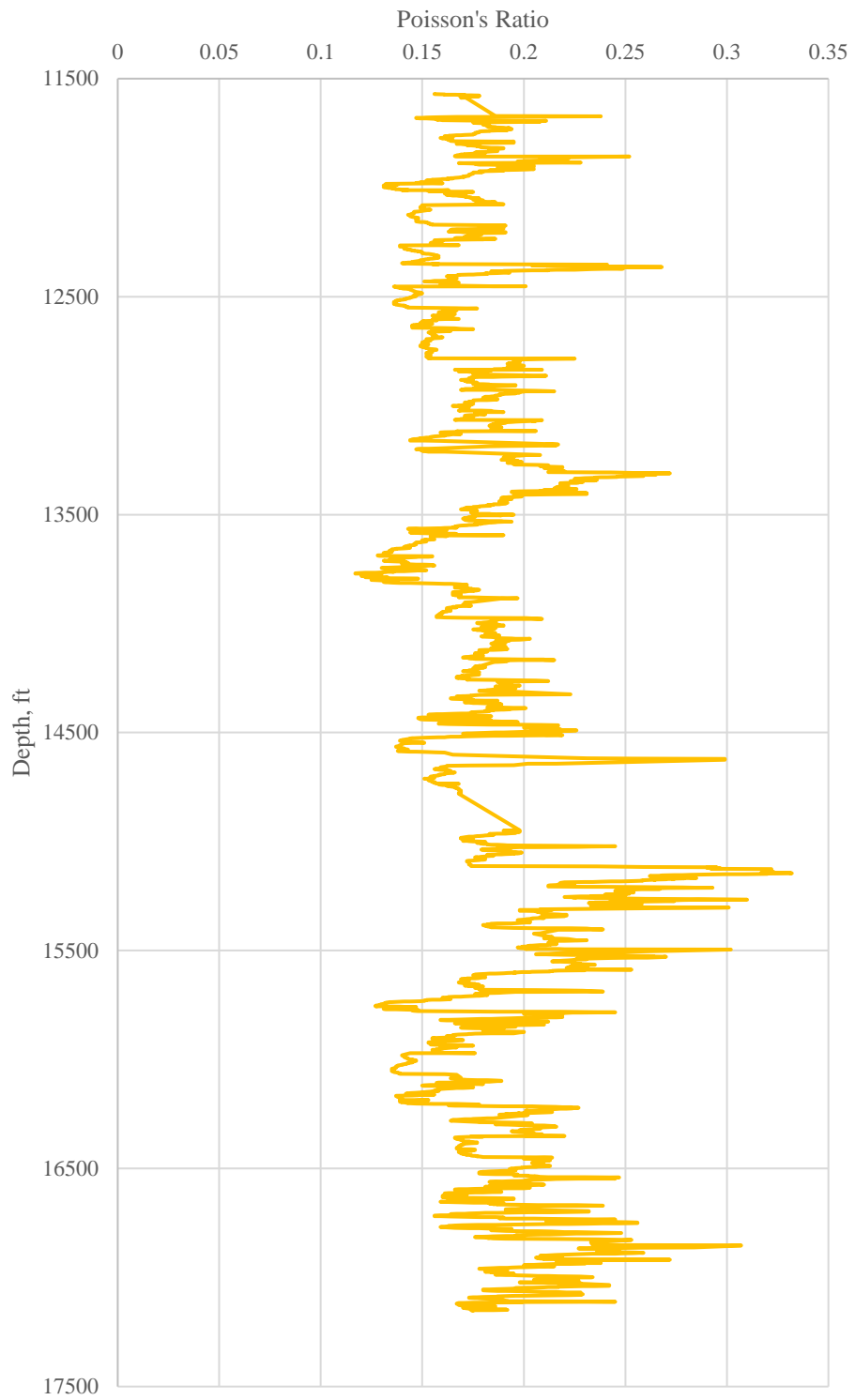


Figure 36: Poisson's Ratio vs Depth

### 5.3 Comparison to Other Shale Plays

When compared to other shale plays, the Caney falls close to the range of the Lower Eagle Ford Shale in Texas (Tahmeen et al., 2020) for each geomechanical property, as explained in Table 6. The table includes research examined for two wells in the Montney Shale and a third in the Eagle Ford Shale play. On average, the Caney UCS and Young's Modulus are much lower than the Montney Shale in Alberta, while the permeability, porosity, and Poisson's Ratio are much higher. The values are also compared against published data for each corresponding formation. For the Caney, the average UCS data of 57.92 MPa aligns closer with published data for the Eagle Ford UCS, with an average of 86.2 MPa (Hu, 2014). For Youngs Modulus, the Caney average of 15.86 GPa compared closer to the published data for the Eagle Ford of 25 – 34 GPa (Sone, 2012). The permeability average of 658.87 nD is within the range of the Eagle Ford published data of 300 – 1100 nD (Walls, 2011). Likewise, for porosity, the Caney Reservoir 3 average is 7.31%, compared to the Eagle Ford published reference of 6.9% (Walls, 2011). Lastly, for Poisson's Ratio, the average of the Caney is 0.243, compared to the published referenced for the Lower Eagle Ford, which is 0.2 – 0.45 (Alidi, 2017).

Table 6: Comparison of the Caney Shale to Other Shale Plays and Published Data

Shale Formation	Study Wells and Published Reference	UCS (Mpa)	Young's Modulus (Gpa)	Permeability (nD)	Porosity (%)	Poisson's Ratio (-)
Alberta & NEBC Montney	Well A	87.9 - 158.8 Avg. 123.24	26.4 - 52.8 Avg. 36.7	167.8 - 230.9 Avg. 199.7	2.67 - 3.22 Avg. 2.92	0.158 - 0.254 Avg. 0.204
	Well B	74.6 - 184.4 Avg. 108.56	18.5 - 40.1 Avg. 21.1	149.2 - 267.9 Avg. 213.7	2.54 - 3.42 Avg. 3.03	0.159 - 0.310 Avg. 0.234
	Published Reference	117 - 136 (Davey, 2012)	35 - 55 (Duenas, 2014)	Avg. 130 (Duenas, 2014)	2 - 5 (Duenas, 2014)	0.09 - 0.28 (Vishkai, 2017)
Lower Eagle Ford	Well C	53.2 - 129.8 Avg. 72.2	20.7 - 41.8 Avg. 30.4	273.6 - 1247.4 Avg. 729.8	4.26 - 9.29 Avg. 6.4	0.214 - 0.347 Avg. 0.278
	Published Reference	Avg. 86.2 (Hu, 2014)	25 - 34 (Sone, 2012)	300 - 1100 (Walls, 2011)	Avg. 6.9 (Walls, 2011)	0.2 - 0.45 (Alidi, 2017)
Caney	Case Study: Garrett	13.41 - 86.89 Avg. 48.725	8.68 - 56.02 Avg. 31.45	91.99 - 605.86 Avg. 177.23	2.40 - 7.866 Avg. 3.589	0.117 - 0.332 Avg. 0.181
	PITT & CHK Data for Res 3	Avg. 53.172 Diff. 8.36%	Avg. 28.37 Diff. 9.80%	Avg. 176.39 Diff. 0.47%	Avg. 3.6 Diff. 0.31%	Avg. 0.179 Diff. 1.1%

## 5.4 STIX Formulations

From the geomechanical property log, the data can be extrapolated and compressed to form one numeric value, the STIX, for selective stimulation. This value, presented here in this section, can take the form of various equations weighing UCS, porosity, permeability, and brittleness. The general trend of the equation is displayed in Section 2.8.4 Equation 42, where the weighted coefficients are  $a_x = 1.5$ ,  $b_x = 1$ , and  $c_x = 1$ . This general formulation is then plotted against UCS in Figure 37 to display the adverse effect of UCS on STIX for a given 1,000' section within the lateral of 11,570' – 12,921'. With the STIX ranging from 0 to 1, higher UCS values such as 11,756' and 12,425' drive the STIX value to zero. Alternatively, the lower UCS zones, 12,373' and 12,490', represent higher STIX values for more fracturability with the reservoir rock.

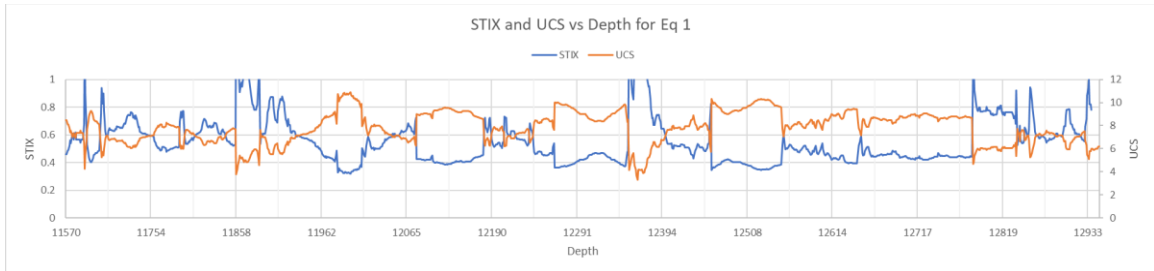


Figure 37: STIX Using Equation 32

An alternate form of the equation considers the difference in bounds of brittleness, UCS, porosity, and permeability. The STIX is then normalized to the maximum to display results between 0 and 1. Equations 21, 22, and 23 are used to calculate the brittleness index (BRIX) from Section 2.3. Equation 42 is then used to generate the STIX profile along the horizontal section of the Garrett well in Reservoir 3 displayed in Figure 38. The same general trend exists between the original equation and this alternate equation.

$$STIX = BRIX * \frac{UCS - UCS_{max}}{UCS_{min} - UCS_{max}} * \frac{Por - Por_{min}}{Por_{max} - Por_{min}} * \frac{K - K_{min}}{K_{max} - K_{min}} \quad (42)$$

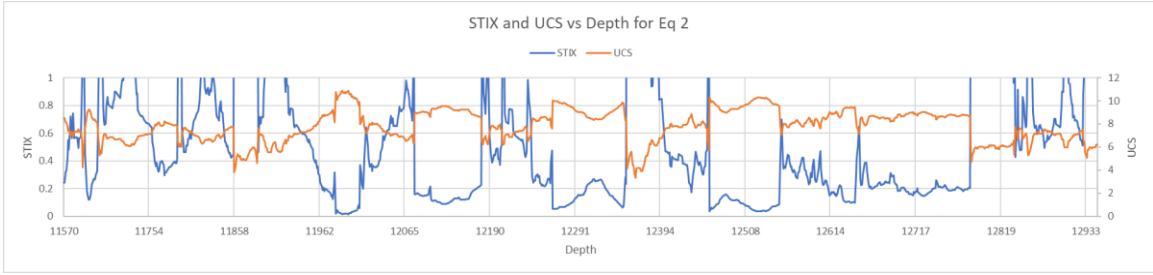


Figure 38: STIX Using Equation 42 with Maximum and Minimum Bounds

The next formulation considers a percentage weight to each parameter totaling 100%. For example, in Equation 43 and Figure 39, the percent weights are 25%, suggesting the operator values each parameter equally when suggesting a stimulation zone. This may not always be the case, as the percent weight of each parameter could change. The UCS is shown in the denominator of Equation 43 for the inverse effect of UCS on STIX and each parameter and is normalized to the average.

$$STIX = \frac{\%BRIX * \frac{BRIX}{BRIX_{avg}} + \%Por * \frac{Por}{Por_{avg}} + \%K * \frac{K}{K_{avg}}}{\%UCS * \frac{UCS}{UCS_{avg}}} \quad (43)$$

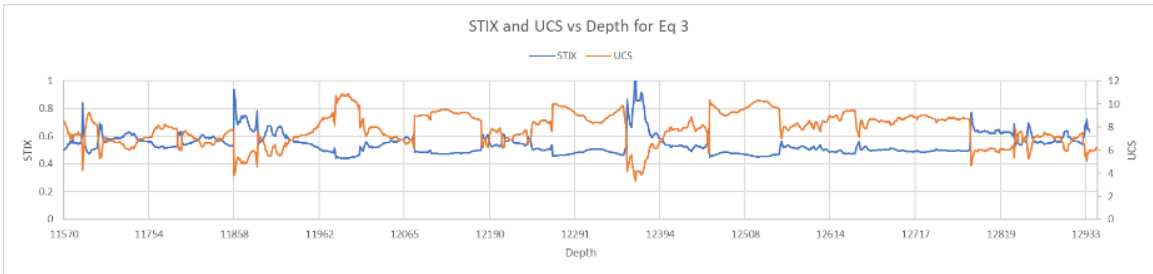


Figure 39: STIX Using Equation 43 with Equal Weight Percent

In accordance with Continental, the completion managers value brittleness significantly over porosity, permeability, and UCS, to the point where taking Equation 42 and deleting the UCS, porosity, and permeability terms to where  $STIX = BRIX$ . Equation 43 could also be used with a very small, non-zero UCS to avoid getting an undetermined value. Figure 40 displays this correlation with the full brittleness profile presented in Appendix A. In this case, the STIX does not have to cross the UCS value for a recommended zone of completion, as UCS is directly correlated to STIX and BRIX. The selective stimulation can be done at higher values of STIX and avoided for lower values of STIX – since the correlation is equivalent to BRIX. In turn, this results in selecting the highest zones of UCS where the fracture conductivity observed by Continental Resources when selecting high brittleness zones is greater than less brittleness zones, further justifying the need for BRIX over UCS, porosity, and permeability.

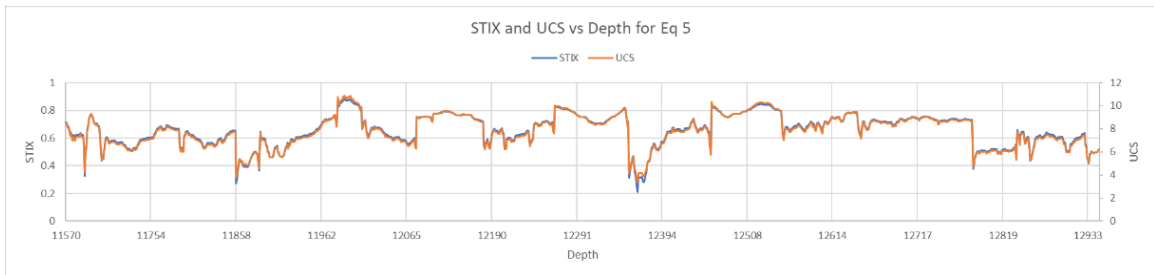


Figure 40: STIX Using Only BRIX

### 5.5 Recommendation

To conclude, a recommendation plan is outlined for the Garrett lateral. Referencing Figure 40 and accounting for Continental’s weighing of STIX, the optimal zones of completion are depths 11,705’ – 11,773’, 11,898’ – 11,987’, 12,202’ – 12,156’, 12,391’ – 12,442’, and 12,256’ – 12,773’, while avoiding the others. This will give the optimal perforation selection and provide Continental with the necessary resources for greater returns and greater production through selective stimulation design.

## CHAPTER VI

### CONCLUSION & FUTURE WORK

The Caney Shale is a developing play in Southern Oklahoma that can be characterized by both its geology and production performance. In the effort to maximize productivity, completion optimization can be implemented wherein selective stimulation can provide the optimal zones for completion metrics by further utilizing the D-Series software and geomechanical and petrophysical property logs.

#### 6.1 Conclusion

In this study, drilling data were used to find the optimal zones of stimulation for the Caney shale. In the process, the triaxial and uniaxial rock properties obtained during core tests calibrated the model to fit downhole drilling data. Once the models were calibrated, a geomechanical property log was generated to obtain a foot-by-foot detail of specific petrophysical and geomechanical rock properties. The Garrett lateral in Reservoir 3 was used due to the similarities of the upcoming well located in the same geographic area. Furthermore, the geomechanical property log was used to select stimulation zones according to the STIX parameter accounting for porosity, permeability, UCS, Poisson's Ratio, and Young's Modulus. According to Continental Resources, the optimal zones of completion should only consider brittleness – the ratio of Young's Modulus to Poisson's Ratio – and in turn, consider zones of highest UCS values. This will, in turn, directly correlate STIX to BRIX in a complete outline of the 6,000' lateral.

## 6.2 Future Work

Obtaining the geomechanical property log from drilling data and fitting the triaxial tests to the model for the Garrett in Reservoir 3 opened two main avenues of approach. First, the geomechanical log can be used for grid inputs into GOHFER for stimulation modelling and frac capabilities. Parameters such as UCS, Poisson's Ratio, permeability, porosity, and Young's Modulus obtained in the thesis herein are necessary for a complete GOHFER model to simulate fracture width, height, and length in the fracture network using appropriate proppant, slurry rate, and volumes. Second, the UCS obtained in D-ROCK using the inverted ROP model and reservoir correlations can be overlaid with the ARS values obtained during drilling optimization in the Pason Optimizer. The strength obtained in the drilling optimizer should directly overlay the strength generated from D-ROCK, further validating the model and its use. When considering the drilling optimizer, parameters such as ROP, RPM, WOB, bit selection, and nozzle sizes can be optimized to further decrease bit wear or increase ROP for a section. While this thesis determines the optimal zones to stimulate based on operator parameters, the geomechanical property logs can unequivocally be used to determine fracture simulation in those specific zones through GOHFER, while also improving drilling through optimization techniques when comparing the ARS obtained in Pason to the UCS obtained in D-ROCK.

## REFERENCES

- Andrews, R. (2007). Stratigraphy, Production, and Reservoir Characteristics of the Caney Shale in Southern Oklahoma. Oklahoma City Geological Survey. 25.
- Atashnezhad, A., Cedola, A. E., & Hareland, G. (2017). An Empirical Model to Estimate a Critical Stimulation Design Parameter Using Drilling Data. Day 4 Wed, April 26, 2017. doi:10.2118/185741-ms
- Benge, M., Lu, Y., Jones, J., Bunger, A.P., Haecker, A., Rihn, A., Crandall, D., Luo, G., Radonjic, M. (2021). ARMA 21-1570, 2021 American Rock Mechanics Association 55th Symposium, 20 – 23 June, Houston, Texas, 2021.
- Cedola, A.E., Atashnezhad, A., Hareland, G. 2017b. Real-time porosity from surface drilling data prediction and verification. AADE-17-NTCE-134, 2017 AADE National Technical Conference and Exhibition, 11-12 April, Houston, Texas, USA, 2017.
- Cedola, A. E., Atashnezhad, A. ., & Hareland, G. . (2017). Evaluating Multiple Methods to Determine Porosity from Drilling Data. Day 3 Wed, March 29, 2017. doi:10.2118/185115-ms
- Davey, H., 2012 “Geomechanical characterization of the Montney shale northeast Alberta and northwest British Columbia, Canada”, M.S. Thesis, Department of Geology and Geological Engineering, Colorado School of Mines, USA.
- Duenas, C. J., Davis, T., & DAMico, D. (2014). Understanding Rock Quality Heterogeneity Using Combined Multicomponent Seismic Inversion and Well Log Cluster Analysis. Montney Shale Reservoir, Pouce Coupe Field, Alberta, Canada. Proceedings of the 2nd Unconventional Resources Technology Conference. doi:10.15530/urtec-2014-1921332
- Gilmer, A. (2015). Well Data. Retrieved February 09, 2021, from <https://www.enverus.com/>
- Hareland, G., & Hoberock, L. L. (1993). Use of Drilling Parameters To Predict In-Situ Stress Bounds. All Days. doi:10.2118/25727-ms
- Hu, D., Matzar, L., & Martysevich, V. (2014). Effect of Natural Fractures on Eagle Ford Shale Mechanical Properties. All Days. doi:10.2118/170651-ms
- Johancsik, C. A., Friesen, D. B., & Dawson, R. (1984). Torque and Drag in Directional Wells-Prediction and Measurement. Journal of Petroleum Technology, 36(06), 987–992. doi:10.2118/11380-pa
- Kerkar, P. B., Hareland, G., Fonseca, E. R., & Hackbarth, C. J. (2014). Estimation of Rock Compressive Strength Using Downhole Weight-on-Bit and Drilling Models. IPTC 2014:

International Petroleum Technology Conference. doi:10.3997/2214-4609-pdb.395.iptc-17447-ms

Onyia, E. C. (1988). Relationships Between Formation Strength, Drilling Strength, and Electric Log Properties. All Days. doi:10.2118/18166-ms

Rickman, R., Mullen, M. J., Petre, J. E., Grieser, W. V., & Kundert, D. (2008). A Practical Use of Shale Petrophysics for Stimulation Design Optimization: All Shale Plays Are Not Clones of the Barnett Shale. All Days. doi:10.2118/115258-ms

Sone, H., 2012, Mechanical properties of shale gas reservoir rocks and its relation to the in-situ stress variation observed in shale gas reservoirs: Ph.D. thesis, Stanford University.

Tahmeen, M., Hareland, G., & Aadnoy, B. S. (2014). Real-Time Software to Estimate Friction Coefficient and Downhole Weight on Bit During Drilling of Horizontal Wells. Volume 5: Materials Technology; Petroleum Technology. doi:10.1115/omae2014-24620

Tahmeen, M., Hareland, G., & Hayes, J. P. (2020). A Convenient Technology to Calculate Geomechanical Properties From Drilling Data. Volume 11: Petroleum Technology. doi:10.1115/omae2020-18923

Tahmeen, M., Hareland, G., Love, J., Rashidi, B. 2017. Complete Geomechanical Property Log from Drilling Data in Unconventional Horizontal Wells. ARMA 17-591, 2017 American Rock Mechanics Symposium, 25 – 28 June, San Francisco, California, 2017.

Tahmeen, M., Cedola, A., Hareland, G., Hays, J. Geomechanical Properties from Drilling Data to Optimize Stimulation Design. AADE-19-NTCE-036, 2019 AADE National Technical Conference and Exhibition, 9 – 10 April, Denver, Colorado, 2019.

Vishkai, M., Wang, J., Wong, R. C. K., Clarkson, C. R., & Gates, I. D. (2017). Modeling geomechanical properties in the montney formation, Alberta, Canada. International Journal of Rock Mechanics and Mining Sciences, 96, 94–105. doi:10.1016/j.ijrmms.2017.04.001

Walls, J. D., & Sinclair, S. W. (2011). Eagle Ford shale reservoir properties from digital rock physics. First Break, 29(6). doi:10.3997/1365-2397.29.6.51280

Zhu, Ty (2018). UCS Data. Retrieved February 03, 2021, from <https://www.jsg.utexas.edu/tyzhu/files/Some-Useful-Numbers.pdf>

APPENDIX A

BRIX vs Depth

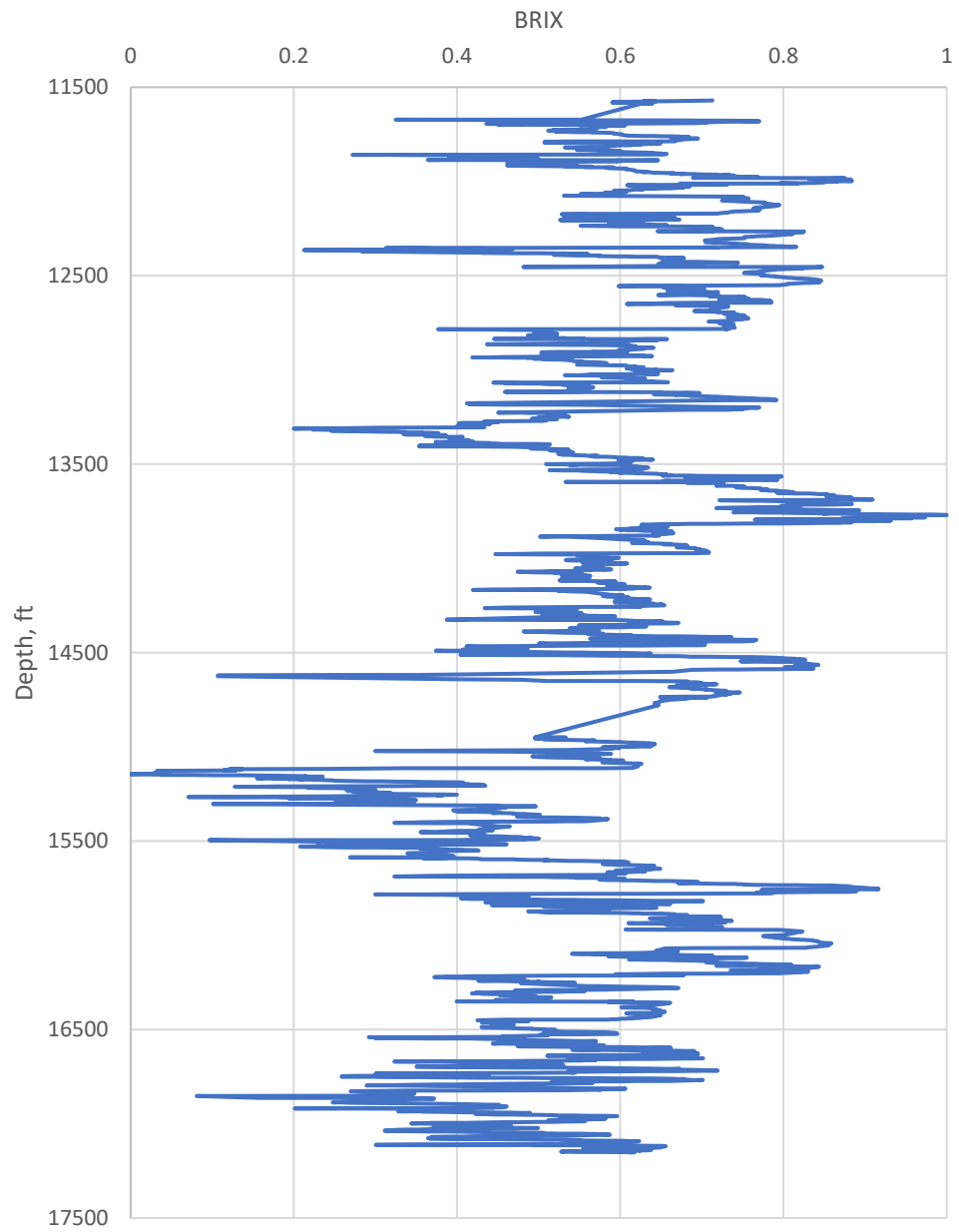


Figure A1: BRIX vs Depth for Garrett Lateral

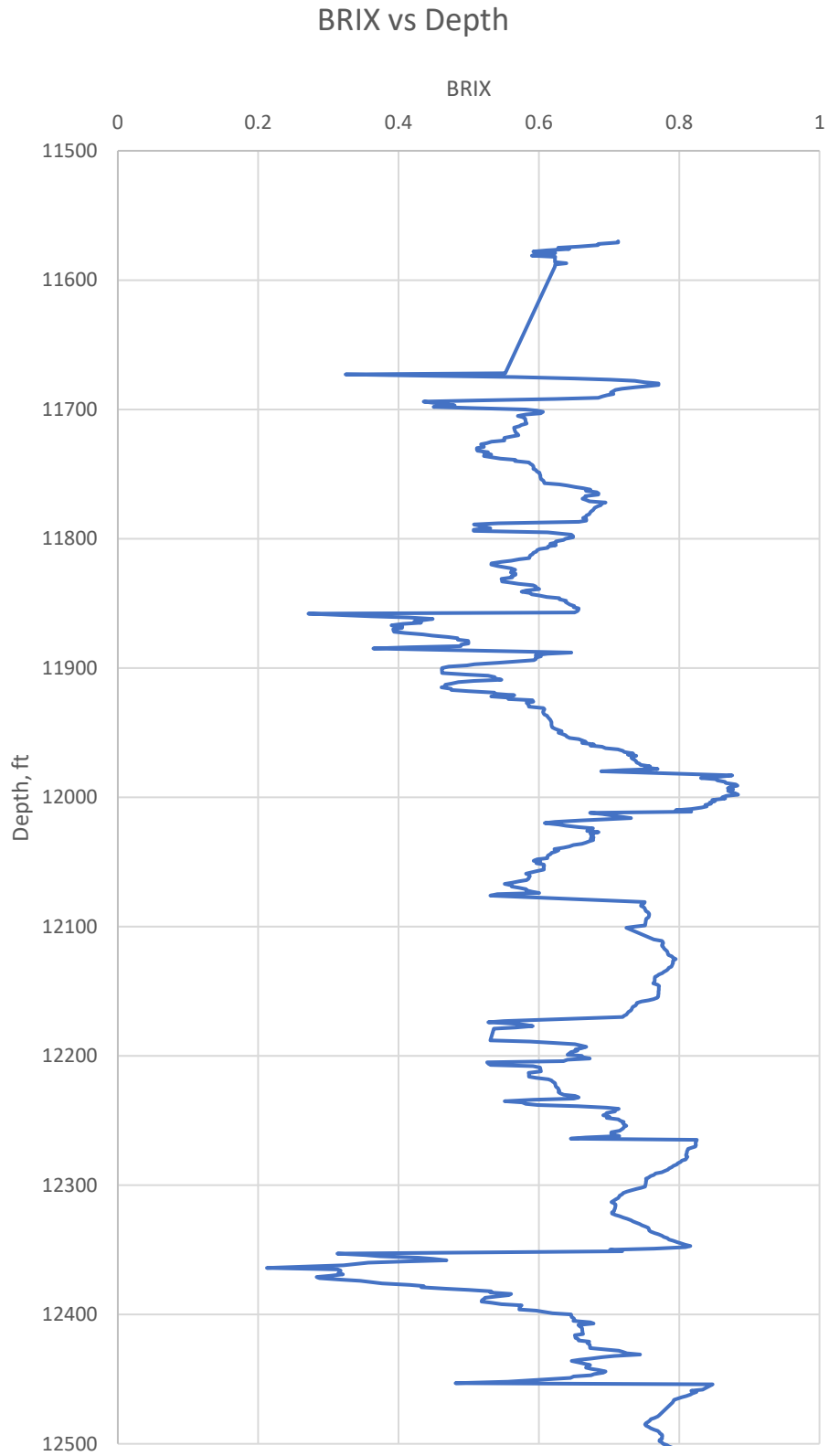


Figure A2: BRIX vs Depth for Garrett of Depth 11,500' – 12,500'

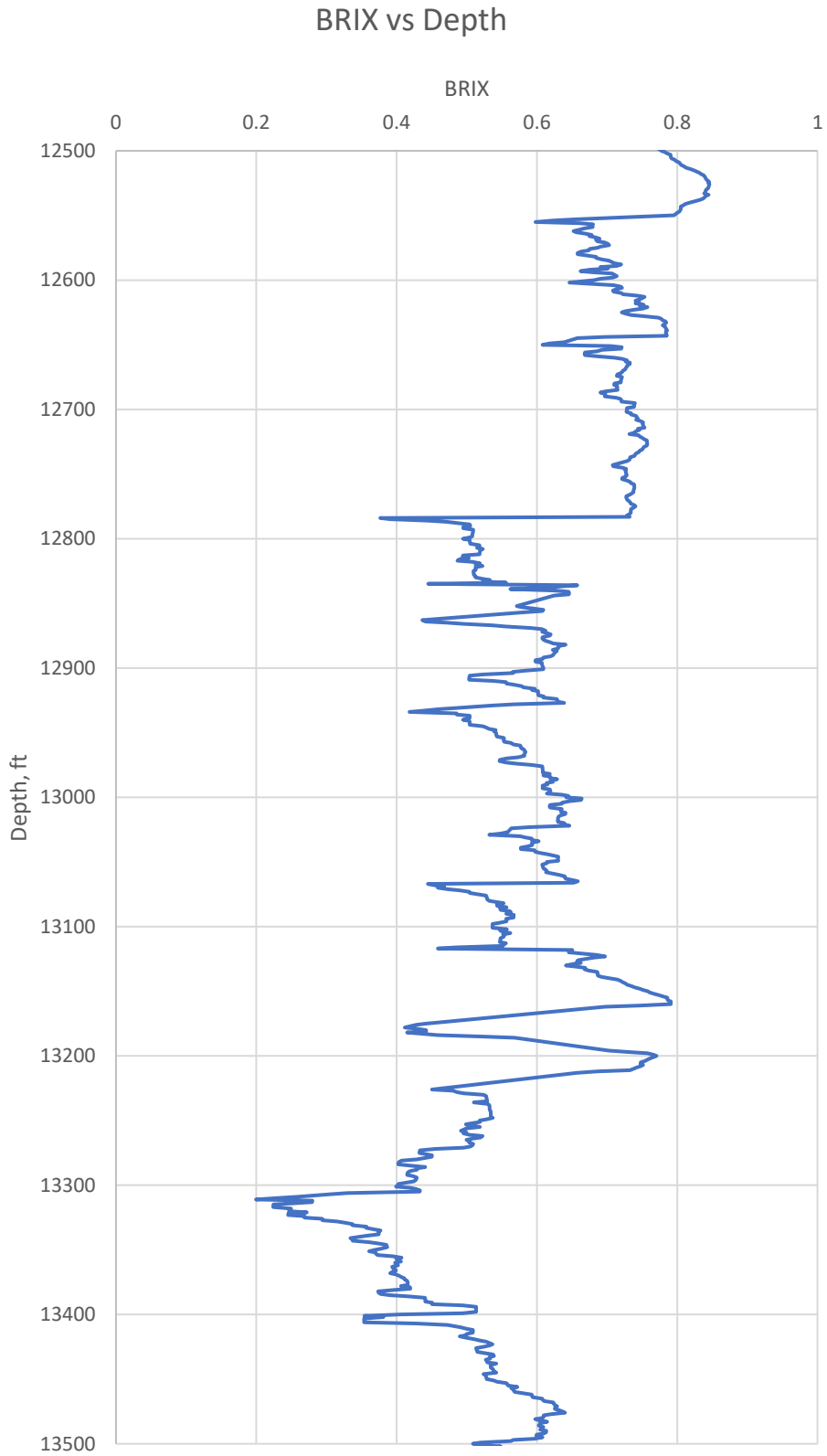


Figure A3: BRIX vs Depth for Garrett of Depth 12,500' – 13,500'

# BRIX vs Depth

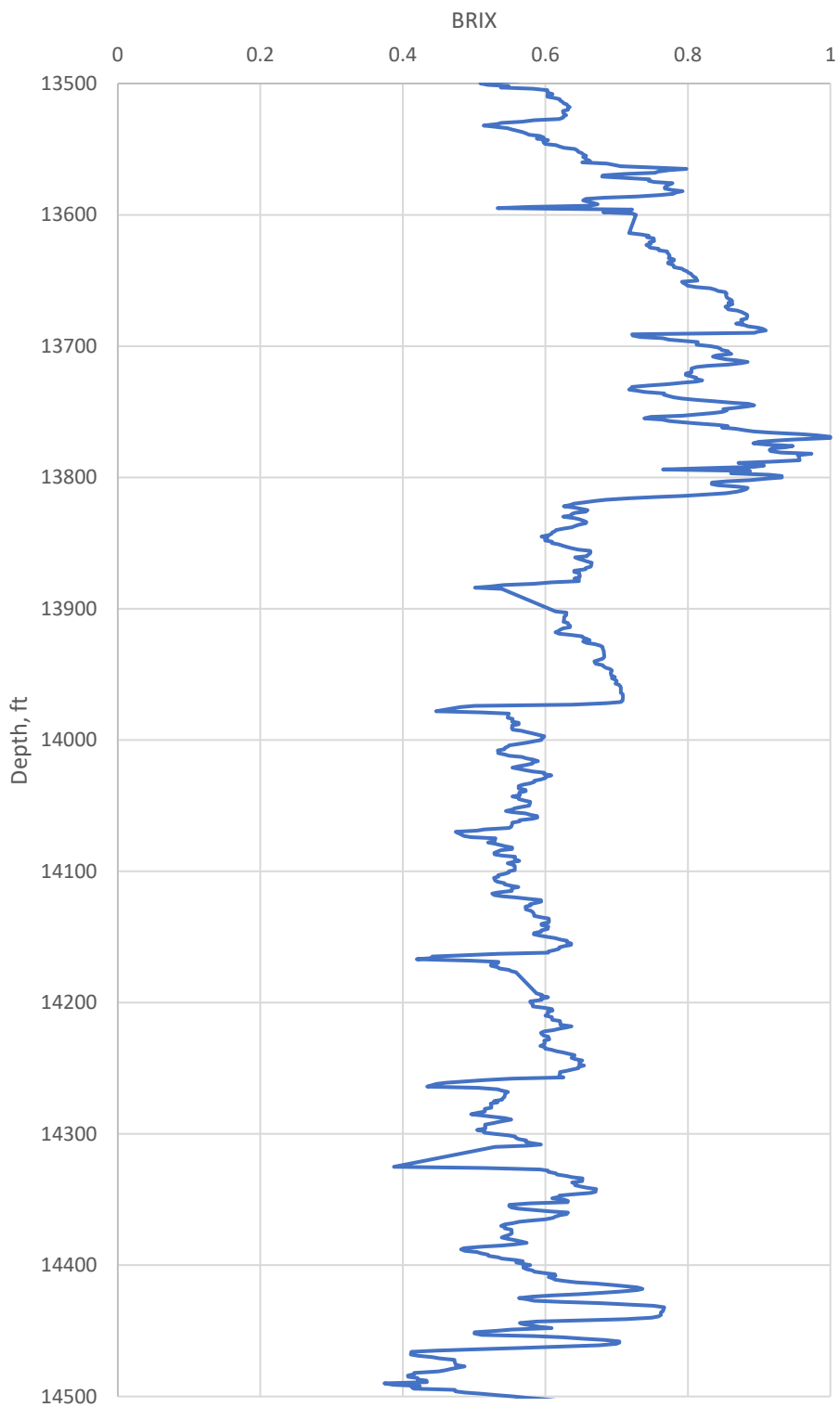


Figure A4: BRIX vs Depth for Garrett of Depth 13,500' – 14,500'

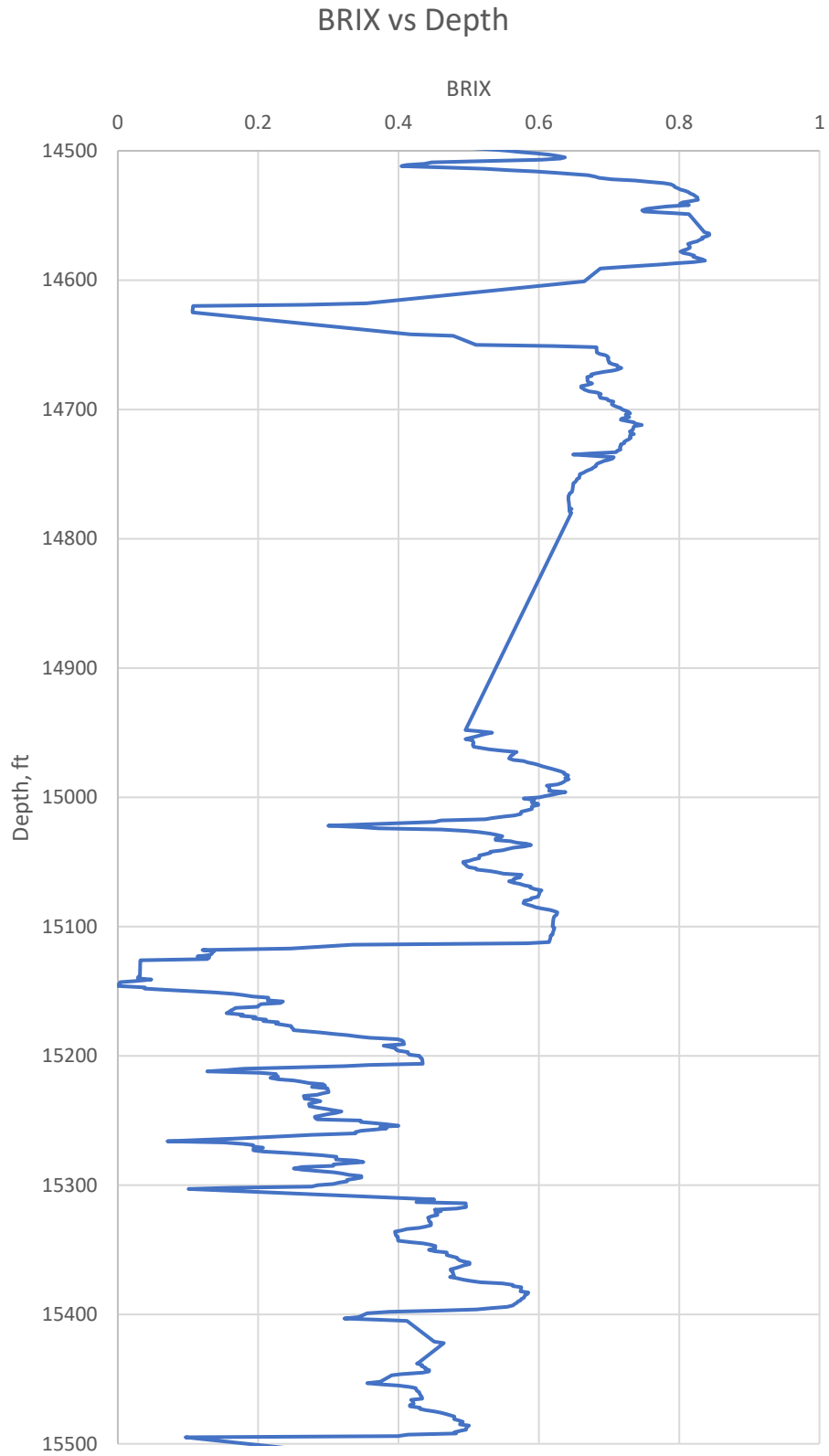


Figure A5: BRIX vs Depth for Garrett of Depth 14,500' – 15,500'

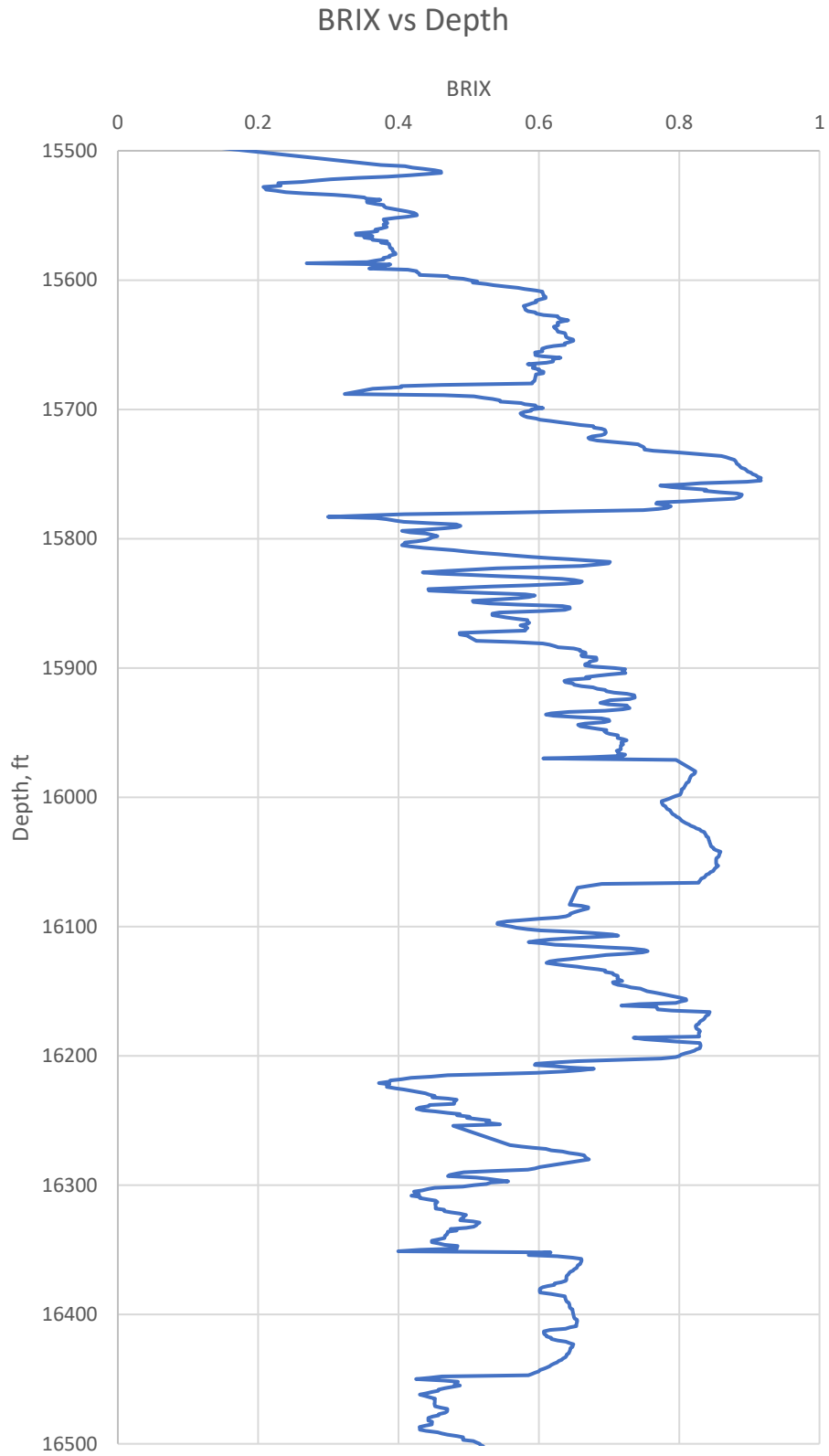


Figure A6: BRIX vs Depth for Garrett of Depth 15,500' – 16,500'

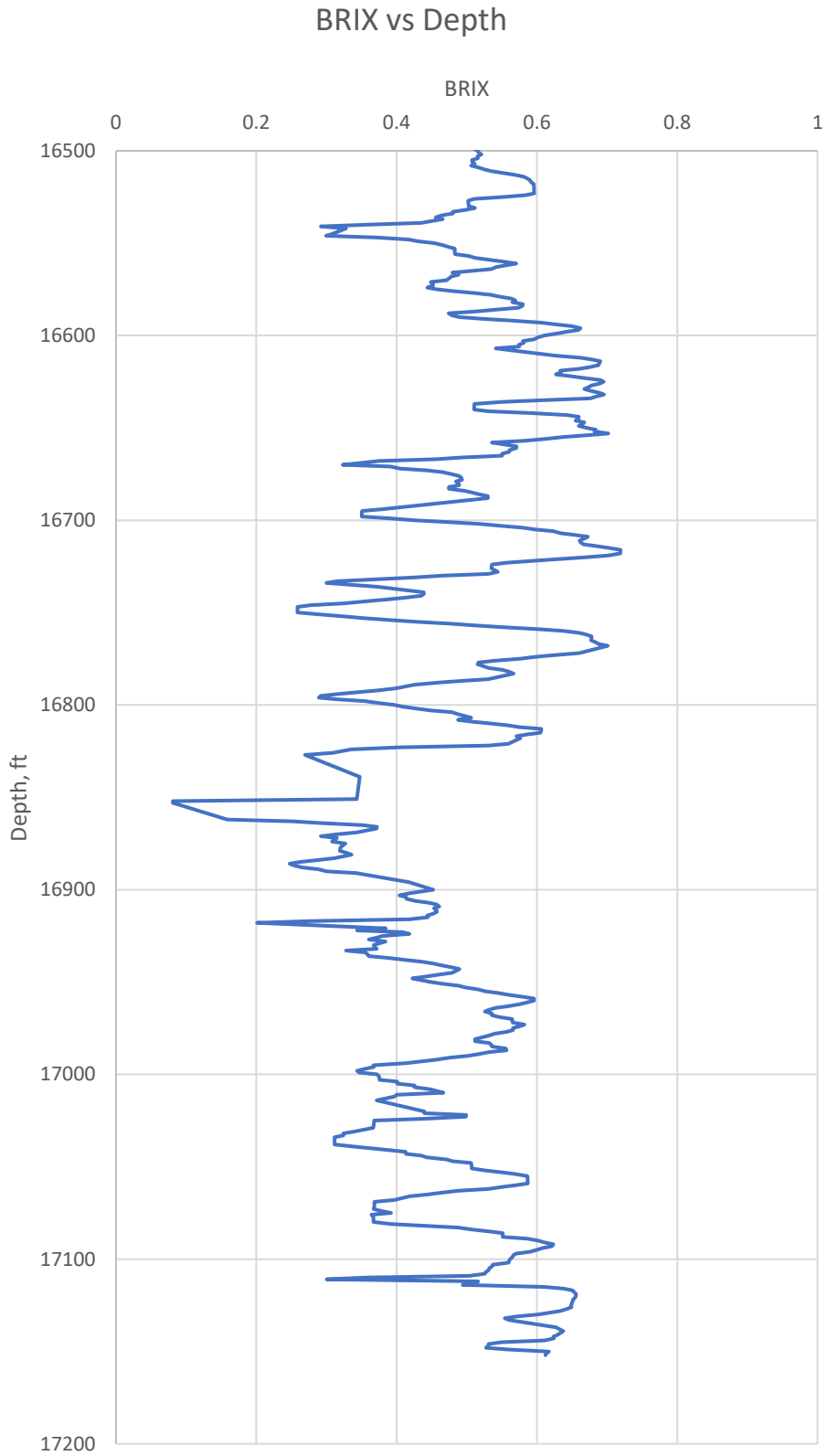


Figure A7: BRIX vs Depth for Garrett of Depth 16,500' – 17,200'

VITA

Haden Patrick Kolmer

Candidate for the Degree of

Master of Science

Thesis: THE USE OF CORE AND DRILLING DATA FOR SELECTIVE  
STIMULATION SELECTION IN THE CANEY SHALE

Major Field: Petroleum Engineering

Biographical:

Education:

Completed the requirements for the Master of Science in Petroleum Engineering at Oklahoma State University, Stillwater, Oklahoma in May, 2021.

Completed the requirements for the Bachelor of Science in Mechanical Engineering at Oklahoma State University, Stillwater, OK in 2019.

Experience:

Halliburton Energy Services, Hydraulic Fracturing, May 2019 – August 2019  
Ft. Lupton, CO: Field Engineering Intern

Halliburton Energy Services, Hydraulic Fracturing, May 2018 – August 2018  
El Reno, OK: Field Engineering Intern

Professional Memberships:

Society of Petroleum Engineers  
American Association of Drilling Engineers  
American Society of Mechanical Engineers